STRUCTURE OF THE PROTON UNBOUND NUCLEUS ^{11}N

by

Afshin Azhari

A DISSERTATION

Submitted to
Michigan State University
in partial fulfillment of the requirements
for the Degree of

DOCTOR OF PHILOSOPHY

Department of Physics and Astronomy

1996

ABSTRACT

STRUCTURE OF THE PROTON UNBOUND NUCLEUS ^{11}N

By

Afshin Azhari

A previous experimental study of the proton unbound nucleus ^{11}N did not observe the ground state and theoretical calculations predicted the ground state to be unbound to proton decay by 1.9 MeV. However, a study of the diproton decay of ^{12}O favored a sequential proton decay via an intermediate state in ^{11}N at 900 keV to the ground state of ^{10}C. Recent theoretical calculations of the ground state of ^{11}N obtained a decay energy of 1.6 MeV. Therefore, a clarification of the structure of ^{11}N was needed.

In the present study, the states in ^{11}N were populated through the reaction ^{9}Be(^{12}N,^{11}N) using a radioactive nuclear beam of ^{12}N. Due to extremely short lifetimes (~10^{-21} seconds), the ^{11}N decayed into a ^{10}C nucleus by emitting a proton inside the target. These decay products were detected in coincidence and momentum vectors were obtained for each, thus allowing for a kinematic reconstruction of the decaying states within ^{11}N.

Monte Carlo simulations of the decay energy spectrum of ^{11}N were performed. χ^2 optimizations of the simulations relative to the data yielded a decay energy of 1.45 MeV and a width of 2.4 MeV for the ground state of ^{11}N.

To my mother and the memory of my father

ACKNOWLEDGMENTS

First and foremost I would like to thank God for without Him nothing would be possible.

I had the privilege of working with one of the most talented scientists I have ever known. No words can convey the gratitude I feel for all that Michael Thoennessen has done to make my experiences as a growing scientist as smooth and efficient as possible. As a mentor and a friend, I could have found none better.

I would like to thank professors Julius Kovacs, David Tomanek, and Gary Westfall for being on my guidance committee. I thank Prof. Alex Brown for his tutelage and providing some of the theoretical calculations in addition to being a member on my guidance committee. I also greatly appreciate the theoretical calculations provided by Dr. Millener.

I truly enjoyed working with my collaborators Dan Russ and Houria Madani from Maryland and am indebted for all their help with the setup of the experiment. I also had the good fortune of working with Tiina Süomijarvi from Orsay who tirelessly helped with the electronics setup.

My thanks go out to the staff of the NSCL without whom this work would not have been possible. I wish to especially thank Craig Snow and Dave Sanderson for their continuos help, especially those last minute lifesavers.

Perhaps the most enjoying part of working at the NSCL was working alongside members of our group Easwar Ramakrishnan, Shigeru Yokoyama, Bob Kryger, Thomas Baumann, Peter Thirolf, and Marcus Chromik. I also had the pleasure of interacting with Jim Brown, Michael Fauerbach, Jon Kruse, Phil Zecher, Barry Davis, Mathias Steiner, Raman Pfaff, Stefan Hannuschke, Sally Gaff, Jing Wang, Richard Ibbotson, and John 'Ned' Kelley who always kept me on my toes.

Closer to home, I would like to thank my beloved wife Nancy for all her patience and moral support throughout my graduate years. My heartfelt thanks go out to my aunt and uncle Guity and Ataolah Modir Massihai for all they have done for me and are as dear to me as my own parents. As a final note, I would like to thank my mother and sister Mahvash and Maryam for their encouragements and aid, and to my father Nader who made my dream come true.

TABLE OF CONTENTS

List of Tables

List of Figures

Chapter 1

Introduction

Although nuclei near and beyond the particle drip lines exhibit extremely short lifetimes, typical of strong interaction time scale, they play an important role in the observed abundance of elements in the universe. On the proton rich side of the valley of stability, the rp-process is a major contributor to nucleosynthesis within supernovae. Therefore, an understanding of the structure of these exotic nuclei is of high priority to astrophysical calculations.

The exact location of the particle drip lines is one of the most stringent tests of nuclear structure models, especially in the extension of mass formulas to and beyond the drip lines. Beyond the proton drip line, the Coulomb and centrifugal barriers can lead to relatively long lifetimes (proton radioactivity) [Hof94]. Several of these ground state proton emitters have been observed [Pag92] and provide a unique probe of the nuclear structure since their lifetimes are sensitive to the nuclear potential [Pag94, Tig94].

However, the production of these exotic nuclei at rates needed for experimental studies has posed a major challenge to experimenters. The recent availability of

radioactive nuclear beams has opened a new doorway into the production of unstable nuclei away from the valley of stability. Since radioactive beams of nuclei can be created which are already deficient in neutron number, nuclei near and beyond the proton dripline can be formed at higher rates.

In the absence of the centrifugal barrier, such as an *s*-wave proton, the lifetime of the ground state of nuclei beyond the proton drip line can be extremely small. One such possible candidate is ^{11}N. A simple shell model picture of ^{11}N predicts the ground state to be a $1/2^-$ state, however the ground state of ^{11}Be (the mirror nucleus of ^{11}N) is a $1/2^+$ state [Ajz90]. The 0.32 MeV gap between the $1/2^+$ ground state and the $1/2^-$ first excited state of ^{11}Be can be accounted for in terms of three distinct physical contributions [Bro94]. First (I), the $1s_{1/2}$ single-particle energy is calculated to be about 3.6 MeV above the $0p_{1/2}$ single-particle energy. (ii) There is an extra pairing energy in the $1/2^+$ configuration due to the two neutron holes in the 0p shell which lowers the $1/2^+$ energy, relative to the $1/2^-$ configuration, by about 2.2 MeV. (iii) There is mixing with the $[2^+ \otimes d_{5/2}](1/2^+)$ configuration which lowers the energy by about 1.5 MeV [Bro94]. Adding the three aforementioned effects, the $1/2^+$ and $1/2^-$ configurations become essentially degenerate. Also, a linear extrapolation between the $p_{1/2}$ - $s_{1/2}$ difference in ^{13}C (3.09 MeV) and the corresponding difference between the center of mass in ^{12}B (1.44 MeV) gives the predicted difference in ^{11}Be [Tal60]. Figure 1.1 shows the result of such a calculation. Therefore, the ground state of ^{11}N is expected to also consist of $1/2^+$ intruder state.

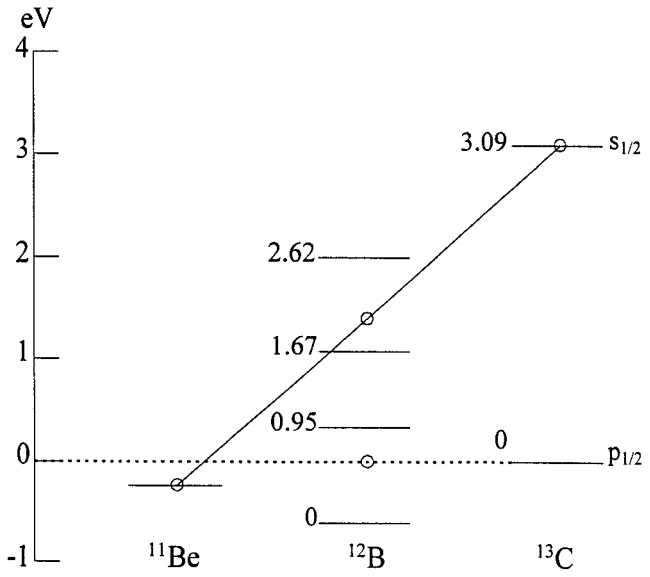

Figure 1.1: Competition between $s_{1/2}$ and $p_{1/2}$ levels [Tal60].

Primary interest in the structure of ^{11}N arose from the results of an experiment to study the two-proton decay of ^{12}O. Goldanskii [Gol61] predicted the existence of ground state diproton decay in proton-rich even-Z nuclei where the pairing energy between the last two protons would forbid the one proton decay branch. Based on current mass measurements [Ajz91], ^{12}O is one such candidate. Previous to the experimental study of ^{12}O, calculations of the ground state of ^{11}N reported the ground state at 1.9 MeV above proton decay threshold. If the ground state of ^{11}N was located at 1.9 MeV, a sequential decay of ^{12}O via ^{11}N would not be energetically possible. In addition, the sequential decay through the tail of a broad (Γ = 1.5 MeV) ^{11}N state at 1.9 MeV is strongly suppressed by penetrability and does not reproduce the measured width of the ^{12}O ground state. Therefore, the ground state of ^{12}O was believed to decay by a di-proton to ^{10}C since the sequential proton decay of ^{12}O would have been suppressed by the predicted ground

state energy of ^{11}N. However, Kryger *et al.* [Kry95] established an upper limit of 7% on the di-proton decay branch and discovered that the data could be reproduced with the assumption of an intermediate state in ^{11}N at about 900 keV.

The first experimental study of ^{11}N used the reaction ^{14}N(^{3}He,^{6}He)^{11}N to reconstruct the levels of ^{11}N by observing the kinematics of the ^{6}He [Ben74]. Figure 1.2 shows the spectrum that was obtained in this experiment. The solid line is a fit attributed to the $1/2^-$ excited state of ^{11}N. A decay energy of 2.24 ± 0.10 MeV and a width of 740 ± 100 keV were obtained from this fit [Ben74]. The $1/2^+$ ground state was deduced from the Isobaric Multiplet Mass Equation (IMME) to be at 1.9 MeV [Ben74].

Recently the ground state of ^{11}N has been reexamined by several theoretical approaches. Sherr [She95] suggested that the isobaric analog states in ^{11}B and ^{11}C could have been misidentified and used a new set of energies to calculate a decay energy of 1.5 ± 0.1 MeV for the $1/2^+$ ground state of ^{11}N from the IMME. Fortune *et al.* [For95] (hereafter referred to as FKL) also pointed out the possibility of the misidentification of the states in ^{11}B and ^{11}C. However, FKL believe that the IMME does not apply to lightly bound (or unbound) $2s\frac{1}{2}$ states. Instead they carry out a potential model calculation to obtain $E_{decay} = 1.60 \pm 0.22$ MeV and $\Gamma = 1.58^{+0.75}_{-0.52}$ MeV for the ground state. Barker [Bar96] attempted the same calculations performed by FKL, but could not obtain the same results. Barker suggests that the potential model calculation of FKL applies only to single-particle states where the spectroscopic factor is of the order of 1. This is not valid for the levels in ^{11}Be, the isobaric analogue of ^{11}N which was used to obtain the parameters of the potential well, since the spectroscopic factor for all levels are

considerably less than one. By incorporating a significant amount of *d*-wave contribution, Barker calculated a decay energy of 1.60 MeV and a width of 1.39 MeV, in agreement with the results obtained by FKL but not using the same method.

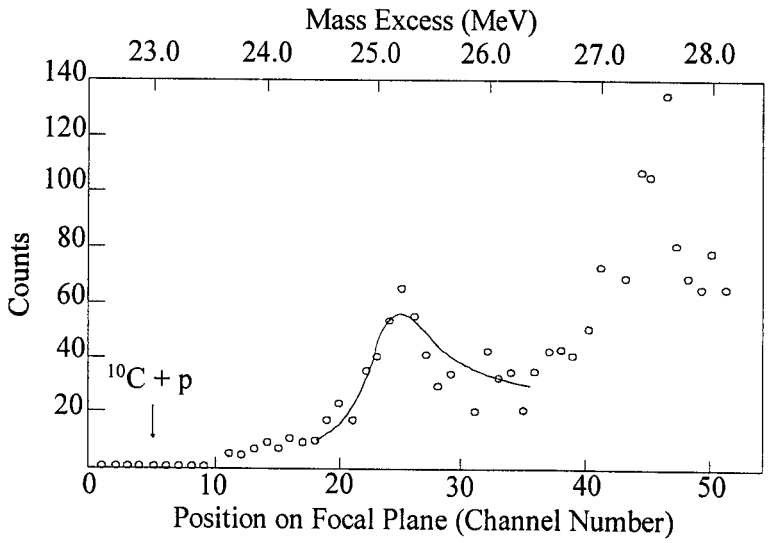

Figure 1.2: Spectrum obtained for ^{11}N from ^{14}N(^{3}He,^{6}He)^{11}N [Ben74]. The solid peak is a theoretical fit of the first excited state. Indicated on the spectrum is the proton decay threshold for ^{11}N.

These apparent inconsistencies could be resolved by an experimental study of the ground state of ^{11}N. The recent availability of radioactive nuclear beams has made the task of studying exotic nuclei such as ^{11}N more feasible. Therefore, we designed an experiment to study ^{11}N using a radioactive beam of ^{12}N. The detailed structure of the setup and analysis of this experiment will be provided in the following chapters.

Chapter 2

Theoretical Overview

2.1 Calculation of the Ground State

Although an experimental study of ^{11}N has been previously performed, only the $1/2^-$ first excited state was observed and the ground state was calculated to be at 1.9 MeV above proton decay threshold [Ben74]. As yet, the only information available on the ground state has come from theoretical calculations using various methods. This section will present an overview of these calculations and their results.

2.1.1 The IMME

The Isobaric Multiplet Mass Equation was first proposed by Wigner [Wig57] and was successfully applied to 22 cases by Benenson *et al.* [Ben79]. This success prompted the application of the IMME to the ground state of ^{11}N. Due to the quadratic nature of the IMME, at least three known states are needed to calculate the coefficients within the equation. Therefore, it can only be applied to a minimum of an isobaric quartet. In principle all nuclear states with isospin T belong to a group of 2T+1 levels with similar

wavefunctions but different charges as measured by the T_z component of T. As an example with direct bearing here, ^{11}N belongs to the quartet containing ^{11}C, ^{11}B, and ^{11}Be.

A thorough derivation is presented by Benenson *et al.* [Ben79] which yields the total energy of a state as

$$\langle \eta T T_z | H_{CI} + H' | \eta T T_z \rangle = \alpha + \beta T_z + \gamma T_z^2 \tag{2.1}$$

where H_{CI} is the charge independent Hamiltonian, H' is the two-body perturbation Hamiltonian, T_z is the z-component of the nuclear isospin defined by

$$T_z = \frac{N - Z}{2}, \tag{2.2}$$

α, β, and γ are constant coefficients and η represents the rest of the quantum numbers. From Equation 2.1 one can calculate the mass of a state from

$$M(T_z) = a + bT_z + cT_z^2. \tag{2.3}$$

Equation 2.3 is known as the IMME and can be used to find a mathematical equality for the coefficient of T_z^3 which must be zero. Calculation of this coefficient yields

$$d = \frac{1}{6}\left[M(-3/2) - M(3/2) - 3\left(M(-1/2) - M(1/2)\right)\right] = 0. \tag{2.4}$$

Table 2.1 contains the parameters used by Benenson *et al.* [Ben79] to calculate the mass of the ground state of ^{11}N. The last column contains the atomic mass excesses. Inserting these values into Equation 2.4 one obtains the ground state mass of ^{11}N to be higher than the mass of the ground state of ^{10}C [Ajz88] plus a proton by 1.9 MeV using

$$M(T_Z) = A(T_Z) \times u + E_x(T_Z) + \Delta(T_Z)$$

where A is the atomic number, u is the atomic mass unit, E_X is the excitation energy, and Δ is the atomic mass excess of the state.

Table 2.1: Parameters used with the IMME for the calculation of the ground state of ^{11}N shown in the last row [Ben79]. The last column contains the mass excess of each state.

Nucleus	T_z	E_x (MeV)	Δ (MeV)
^{11}Be	3/2	0.0	20.176
^{11}B	1/2	12.91	21.580
^{11}C	-1/2	12.50	23.150
^{11}N	1/2	0.0	24.98

The form of the IMME shows a strong dependence on the accuracy of the excitation energy of the states used therein, especially the states in ^{11}B and ^{11}C since these values are multiplied by a factor of three in Equation 2.4. Therefore, a small error or misidentification can create large discrepancies in the calculation of the unknown state. Sherr [She95] stated that the energy of the relevant state in ^{11}C could be lower by 100 - 150 keV which would lower the IMME prediction by 300 - 450 keV resulting in a ground state energy of 1.5 ± 0.1 MeV for ^{11}N.

2.1.2 Potential Model Calculations

FKL [For95] used a Woods-Saxon potential including Coulomb and spin-orbit forces to describe ^{11}Be and ^{11}N. The geometric parameters r_0, a, and the spin-orbit potential $V_{\text{spin-orbit}}$ were obtained from satisfactory fits of the $2s\frac{1}{2}$ single-particle energies

of ^{17}O and ^{17}F. Known energies of the states in ^{11}Be were used to obtain the potential depth. These parameters were then applied to ^{11}N. It should be noted that this method applies only to single-particle states, however the use of this method was justified by FKL by observing that the first three states of ^{11}Be are dominated by single-particle configurations.

The width of the states were defined by FKL as

$$\frac{4}{\Gamma} = \left| \frac{d(\sin 2\delta)}{dE} \right| \tag{2.5}$$

where δ is the total nuclear phase shift. This is equivalent to defining the width as the energy interval over which δ changes from $\pi/4$ to $3\pi/4$. Table 2.2 shows the results of this calculation where the observed width of the state was calculated from the single-particle width incorporating the spectroscopic factors from ^{11}Be in the relation $\Gamma_{pred} = S \cdot \Gamma_{sp}$.

Table 2.2: ^{11}N states calculated by FKL using a Woods-Saxon potential [For95].

J^{π}	E_{decay} (MeV)	Γ_{sp} (MeV)	Γ_{pred} (MeV)
$1/2^{+}$	1.60 ± 0.22	$2.1^{+1.0}_{-0.7}$	$1.58^{+0.75}_{-0.52}$
$1/2^{-}$	2.48	1.45	0.91 ± 0.22

Barker [Bar96] argued that the above definition for the width is best suited for narrow levels and that it could result in large uncertainties for broader states. He also points out that FKL do not show how they obtain the resonance energy.

Barker introduced two definitions for the energy; the resonance energy E_r at which the resonant nuclear phase shift β goes through $\pi/2$, and the peak energy E_m where the density of states function ρ passes through a maximum. The single-particle widths were then defined as the energy interval over which β goes from $\pi/4$ to $3\pi/4$ and the FWHM of ρ. These definitions were used in a potential model calculation similar to FKL using states of ^{11}Be to adjust the Woods-Saxon potential parameters. A decay energy of 1.40 MeV and a width of 1.01 ± 0.07 MeV were calculated for the ground state of ^{11}N. These values do not match those obtained by FKL. The disagreement was attributed to the uncertainty in the definitions used by FKL [Bar96].

Barker [Bar96] argued that this method is only applicable to single-particle states and that the states in ^{11}Be are not totally single-particle states. By incorporating d-wave contributions into the wavefunction of ^{11}Be and calculating the Coulomb displacement energies for ^{11}N, a decay energy of 1.60 MeV and a width of 1.39 MeV were obtained for the ground state of ^{11}N.

2.2 Proton Decay

If the resonance energy of a proton unbound state is lower than the Coulomb and centrifugal barrier, the decay via proton emission can only occur through barrier penetration. The wave function of the decaying state can be written as

$$\psi(r,\theta,\phi) = \frac{\chi_L(r)}{r} Y_{Lm}(\theta,\phi). \qquad (2.6)$$

The decay rate $\lambda = 1/\tau$ is defined as the product of the probability of finding the proton at the surface multiplied by the flux of the proton. In the limiting case of the proton leaving the surface, the decay rate can be written as

$$\lambda = \left(\frac{\hbar k}{\mu}\right) \lim_{r\to\infty} \int_{\Omega} |\psi(r,\theta,\phi)|^2 r^2 d\Omega . \tag{2.7}$$

where μ and k are given by

$$\mu = \frac{M_p M_c}{M_p + M_c}, \qquad k = \frac{\sqrt{2\mu E_p}}{\hbar}.$$

The subscripts p and c have been used to denote the proton and the core nucleus, respectively. Since the spherical harmonics are normalized, the integral over the solid angle is equal to one. This normalization can be inserted into Equation 2.7 to obtain

$$\lambda = \frac{\hbar k}{\mu} |\chi_L(\infty)|^2 . \tag{2.8}$$

The tunneling effect through the Coulomb and centrifugal barriers for a free particle is given by the penetrability as [Rol88]

$$P_L(E,R_n) = \left|\frac{\chi_L(\infty)}{\chi_L(R_n)}\right|^2 \tag{2.9}$$

where R_n is the distance between the center of the core nucleus and the particle being emitted and is given by

$$R_n = R_p + R_c .$$

The penetrability can be inserted into Equation 2.8 to give

$$\lambda = \frac{\hbar k}{\mu} P_L(E,R_n) |\chi_L(R_n)|^2 . \tag{2.10}$$

The nuclear oscillator model [Bla91] can be used to obtain

$$|\chi_L(R_n)|^2 = \frac{2}{R_n}\theta_L^2 \tag{2.11}$$

where θ_L^2 is the spectroscopic factor. Inserting Equation 2.11 into Equation 2.10 gives the partial width, defined as $\Gamma_L \equiv \hbar\lambda$, of a state as

$$\Gamma_L(E,R_n) = \frac{2\hbar^2 k}{\mu R_n} P_L(E,R_n)\theta_L^2 \,. \tag{2.12}$$

Therefore, calculations of the partial width require a knowledge of the penetrability factor $P_L(E,R_n)$. The solution of the Schrödinger equation, containing the Coulomb and centrifugal potential terms, for a particle outside the nucleus is a linear combination of the regular and irregular Coulomb functions $f_L(r)$ and $g_L(r)$ [Rol88] which can be written as

$$\chi_L(r) = af_L(r) + bg_L(r) \tag{2.13}$$

where a and b are constant coefficients. Since we are considering a decay, the radial solution $\chi_L(r)$ must be an outgoing wave which implies that $a = i \cdot b$ [Rol88]. Using this relation in Equation 2.13 and inserting the result into Equation 2.9 yields

$$P_L(E,R_n) = \frac{1}{f_L^2(E,R_n) + g_L^2(E,R_n)} \,. \tag{2.14}$$

The form of the Coulomb functions is quite complex for the decay of a proton, especially when considering angular momenta greater than zero. Therefore a pre-existing code [Kry94] was used to calculate these functions at given energies and radii.

Chapter 3

Experimental Setup

3.1 Production of the Radioactive Beam

3.1.1 Introduction

The experiment was performed at the National Superconducting Cyclotron Laboratory at Michigan State University. A primary beam of ^{16}O was used in a fragmentation reaction to produce the radioactive beam of ^{12}N. Purification was achieved by using the A1200 [She92] mass analysis device in conjunction with the Reaction Products Mass Separator (RPMS) [Cur86, Har81]. The purified ^{12}N beam was incident on a thin secondary target to produce the ^{11}N via one neutron stripping.

Due to a very short lifetime (~10^{-21} seconds), ^{11}N decays within the target into a proton and ^{10}C. The decay products were observed in coincidence and the momentum of each particle was measured which allowed for a complete kinematic reconstruction of the originating state within ^{11}N.

3.1.2 Production and Purification of ^{12}N

An 80 MeV/nucleon primary beam of $^{16}O^{6+}$ was extracted from the K1200 cyclotron at an average current of 750 enA and bombarded a 980 mg/cm^2 thick ^{9}Be target in front of the A1200 mass separator. A schematic diagram of the A1200 indicating the position of elements used in the production and purification of the beam is shown in Figure 3.1. The ^{12}N secondary beam was produced along with many other fragments. The A1200 uses a series of dipoles, quadrupoles, and degraders to filter the fragments according to their rigidity. The rigidity is defined as the particle momentum divided by total charge. Therefore, the A1200 was tuned to improve the purity of the ^{12}N and to focus the beam at the focal plane. The magnetic field settings required for the tuning of the A1200 were calculated using the code INTENSITY [Win92].

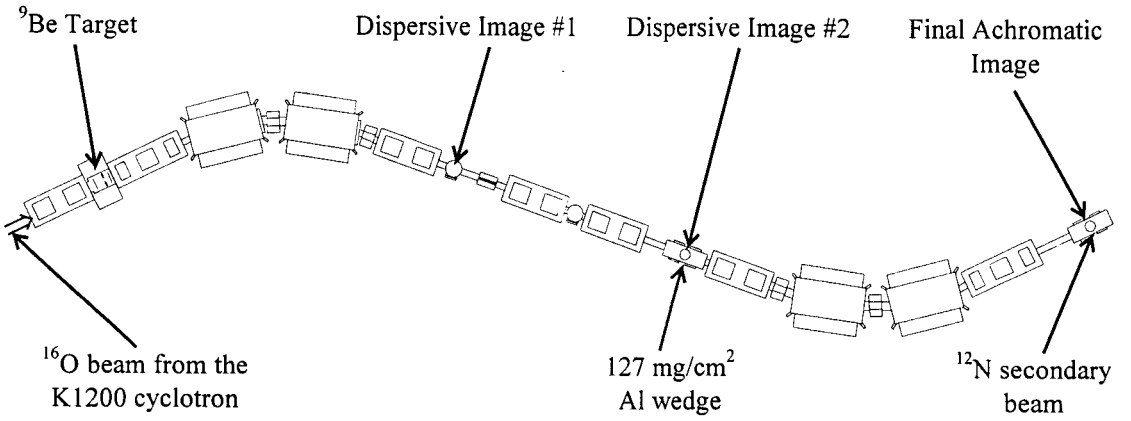

Figure 3.1: Diagram of the A1200 mass separator in the configuration used to produce and purify the ^{12}N secondary beam.

The ^{12}N fragments were produced with a 10% momentum spread [Win92]. To reduce the momentum spread, the 3% momentum slits in the dispersive image #2 of the A1200 were inserted. The fragmentation method used to produce the ^{12}N also produced other proton rich fragments with rigidities close to that of ^{12}N. Therefore, these fragments were also focused at the focal plane of the A1200 as contamination.

A 300 μm Silicon ΔE detector in the focal plane along with a thin timing scintillator were used to identify the incoming particles. Figure 3.2 shows a plot of the energy loss versus time-of-flight of the fragments at the focal plane. The radio frequency (RF) structure of the cyclotron was taken advantage of to check for wrap-around in the time spectrum of Figure 3.2. By observing the down-scaled RF pulses in coincidence with fragments at the focal plane, an identical image translated in time was obtained. This effect can be seen by comparing the events in Figure 3.2 on each side of a vertical line near the center of the spectrum.

The amount of the ^{12}N present at the focal plane was only 0.3%, therefore a 127 mg/cm^2 aluminum wedge was placed in the second dispersive image chamber of the A1200. This wedge acted as a degrader where different fragments lose different amounts of energy, leading to a larger spread in their rigidity. Due to the changes in the rigidity of all fragments, the last part of the A1200 was retuned for the new rigidity of ^{12}N. This resulted in a secondary beam of 40.8 MeV/nucleon ^{12}N fragments at the focal plane of the A1200, increasing the amount of the ^{12}N to 1.3%. The difference in rigidity resulted in a spatial separation in the horizontal direction at the focal plane allowing further purification by the insertion of a pair of slits, driven into the beam in the horizontal

direction, at the focal plane. To determine the most effective slit opening, a position sensitive Parallel Plate Avalanche Counter (PPAC) was used in the focal plane. A plot of the vertical versus the horizontal position of the fragments in the PPAC is shown in Figure 3.3. The dashed vertical lines represent the position of the slits.

Figure 3.4 shows a time-of-flight spectrum for the fragments before and after the insertion of the slits. Although the slits did not affect the ^{12}N and ^{11}C rates, the amount of ^{10}B and ^{16}O were reduced, thus increasing the amount of ^{12}N to 1.7%.

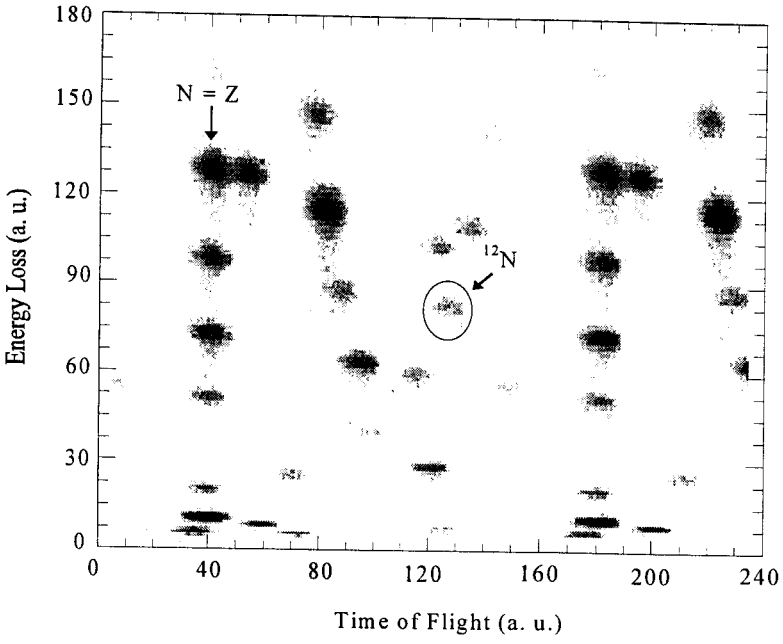

Figure 3.2: A plot of the energy loss versus time-of-flight of the fragments seen at the focal plane of the A1200. Indicated within the figure are fragments with equal number of protons and neutrons, and the secondary radioactive beam of ^{12}N.

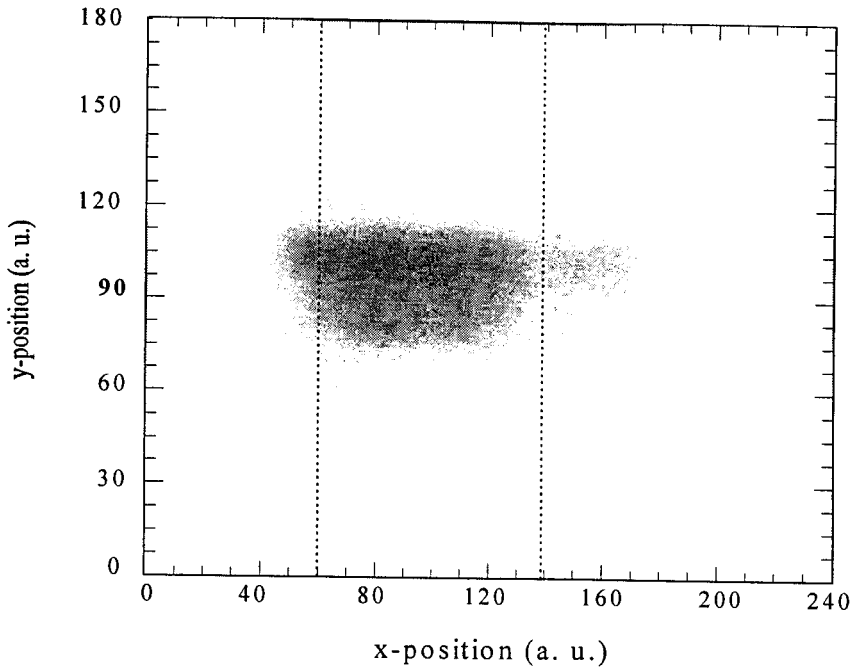

Figure 3.3: Vertical versus horizontal positions of the fragments in the PPAC at the focal plane of the A1200. The dashed lines represent the position of the horizontal slits.

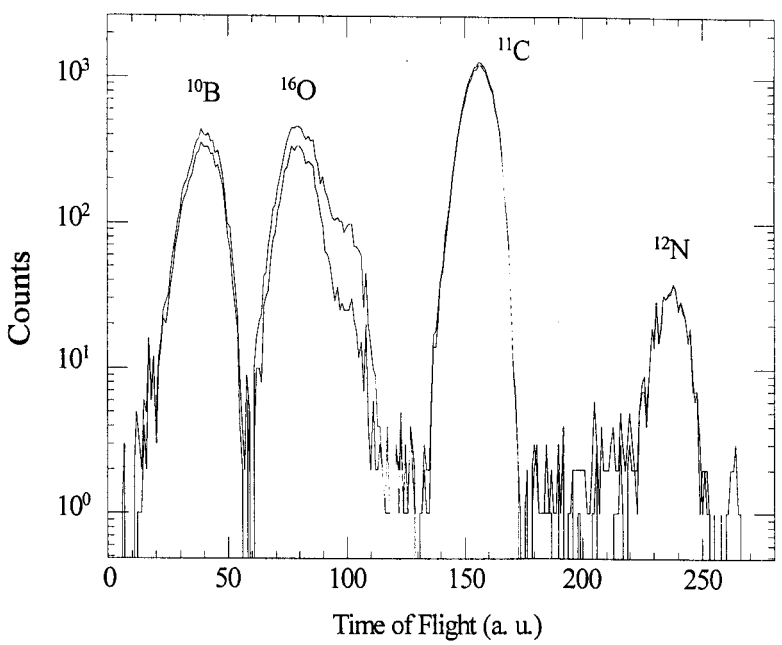

Figure 3.4: Time-of-flight of fragments seen at the focal plane of the A1200 before and after the insertion of the slits.

To achieve higher purity, the ^{12}N fragments along with the contaminants were transported to the Reaction Product Mass Separator (RPMS). The RPMS consists of a quadrupole doublet followed by a Wien filter, a dipole, and a second quadrupole doublet. This configuration is shown in Figure 3.5. A Wien filter consists of perpendicular electric and magnetic fields to select particles according to their velocities. The selected velocity is proportional to the ratio of the electric field to the magnetic field. Particles with significantly different velocities from the tuned setting are bent away and are stopped in the walls of the Wien filter. The contaminants entering the RPMS had the same rigidity as the ^{12}N fragments, and thus different velocities. Therefore, the RPMS created a spatial separation between the ^{12}N and the contaminants. However, not all of the contaminants were stopped in the walls of the RPMS. These contaminants were transported out of the RPMS parallel to the ^{12}N beam, but spatially separated in the vertical direction.

Behind the Wien filter a magnetic dipole followed by a quadrupole acted as a rigidity filter and focused the fragments further down the beam line. These magnets also served another important role. The beam entering the Wien filter had a non-zero radius, therefore corrections had to be made to the beam to allow for a good focus on the target placed further down the line from the second quadrupole doublet. This was achieved by optimizing the magnet settings such that by pivoting the beam line to an angle of 4.5 degrees, at the pivot point indicated in Figure 3.5, the beam would be focused at the secondary target position. The parameters required for the tuning of the RPMS were calculated using the code GIOS [Wol88]. Input parameters needed for this calculation

were the electric field of the Wien filter, the fragment of interest (^{12}N), and the fragment energy.

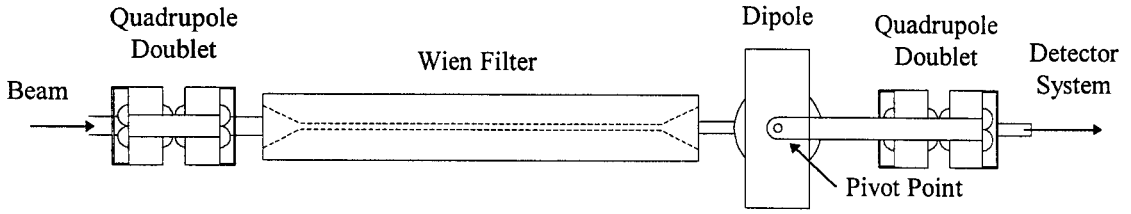

Figure 3.5: The Reaction Products Mass Separator.

In addition to the ^{12}N, spatially separated ^{11}C and ^{13}O were also transported through the Wien filter and had to be identified and eliminated before the target. Figure 3.6 shows a diagram of the tail of the RPMS and the components used therein. The timing scintillator and the ΔE silicon detector in the first chamber were used to identify the particles coming out of the RPMS by plotting the time-of-flight versus the energy loss. Although the RPMS successfully removed the ^{11}C fragments from the beam, a small amount of ^{13}O was still present. Identification of the impurities was performed using the fragment telescope, described in Section 3.2.3. Figure 3.7 shows a plot of the energy loss versus the total energy of the particles seen in the fragment telescope. The small amount of contamination by ^{13}O can be seen in Figure 3.7.

The spatial separation between the ^{13}O and ^{12}N fragments was observed by PPAC 2 and is shown in Figure 3.8. By observing the fragments in PPAC 2 the vertical slits were used to block the ^{13}O resulting in a 95% pure ^{12}N beam at an average rate of 15,000 particles per second.

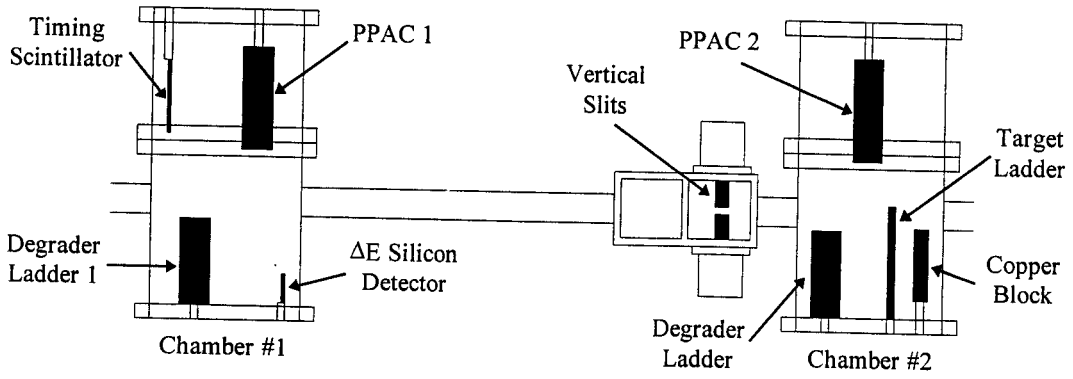

Figure 3.6: Beam line components behind the RPMS.

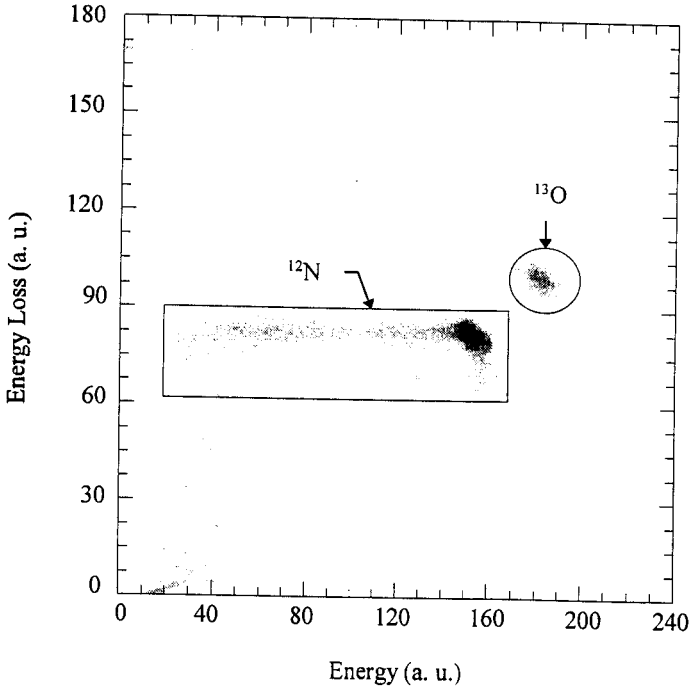

Figure 3.7: Energy loss versus time-of-flight spectrum of fragments seen in the fragment telescope prior to the insertion of the vertical slits.

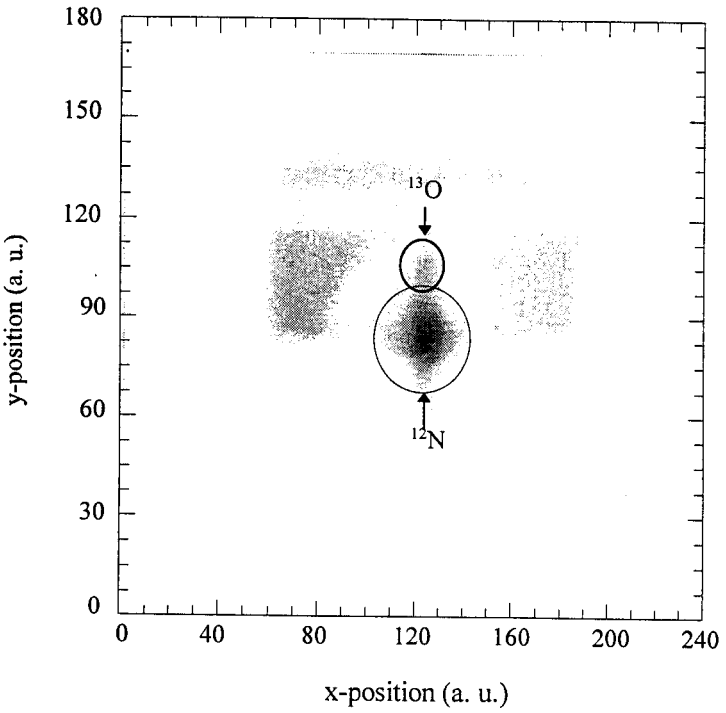

Figure 3.8: Vertical versus horizontal spectrum of PPAC 2. This spectrum shows the spatial separation between ^{12}N and ^{13}O fragments and was used to optimize the position of the vertical slits for the ^{12}N beam.

3.2 Detector Assembly

3.2.1 The Tail of the RPMS

Figure 3.6 shows the setup at the tail of the RPMS. Beam trajectory information was obtained from the two PPACs in the chambers. The copper block in the second chamber was used to protect the proton and fragment detectors during the tuning of the ^{12}N beam and the calibration beams. Aluminum degraders in the degrader ladders were used in conjunction with the calibration beams to provide a broad range of energies and more specific information will be presented later. The target ladder contained a

scintillator for tuning the beam, an empty target holder for target out measurements, a 37 mg/cm^2 thick ^{9}Be foil as the secondary target, and the last position was occupied by a 94 mg/cm^2 gold foil for proton calibrations.

^{11}N was produced by the one neutron stripping reaction ^{9}Be(^{12}N,^{11}N) in the secondary target. Due to the very short lifetime (~10 $^{-21}$ ns) ^{11}N decayed immediately by emitting a proton already inside the target. The proton and ^{10}C daughter nuclei were observed in detectors placed in a large chamber behind chamber #2, (Figure 3.9). The protons were detected using an annular silicon detector (ASI) backed by the Maryland Forward Array (MFA) [Llo92] which consists of a ring of plastic phoswich detectors. This array was placed such that the ASI was at a distance of 20 cm from the target. Due to their larger mass, the ^{10}C fragments were more forward focused than the protons and passed through the central hole of the ASI and MFA. The heavy fragments were collected in a fragment telescope consisting of a position sensitive PPAC, a thin silicon ΔE detector, and a thick silicon energy detector. The fragment telescope PPAC (FTPPAC) was placed 62 cm from the target.

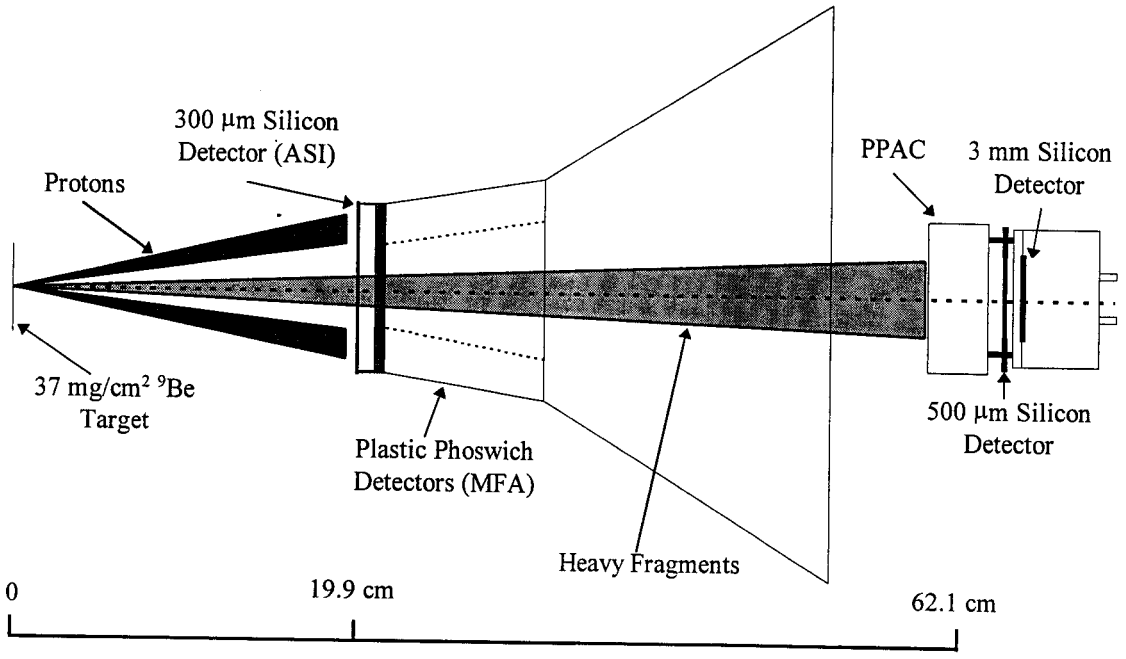

Figure 3.9: Detector setup at the end of the RPMS tail. The ASI and the MFA provided position, ΔE, and E information for the protons. The fragment telescope provided position, ΔE, and E for the heavier fragments.

3.2.2 Proton Detectors

The protons were detected and identified by the ASI and the MFA. The double sided annular 300 μm thick silicon detector (ASI) had an inner radius of 2.4 cm and an outer radius of 9.6 cm. The ASI consists of 16 pie shaped segments on one side and 16 concentric strips on the other, providing 256 pixels. This detector was used to measure the angular distribution of incoming particles along with their energy loss. The MFA, mounted directly behind the ASI, contains a ring of 16 plastic phoswich detectors. The front face of each plastic detector has the same dimensions as the pie segments of the ASI. Each phoswich detector is constructed of a 1 mm thick fast plastic detector optically

coupled to a 10 cm thick slow plastic detector. The light from the two plastic detectors passes through a light guide and into a photomultiplier tube (PMT). Therefore, the signal from the PMT contains a fast and a slow component arising from the two different types of plastic detectors.

Particle identification was achieved in a ΔE - E plot from the ASI versus the total signal from the PMT (total energy). Alternatively pulse shape discrimination between the slow and fast components of the signals from the PMT was also used.

3.2.3 Fragment Detectors

The fragment telescope consisted of three detectors. A position sensitive PPAC (FTPPAC) with an active area of 5x5 cm^2 was used to measure the position of the incoming particles. Mounted behind the PPAC was a 5x5 cm^2 500 μm thick quadrant silicon detector. This detector was used to measure the energy loss of the heavy fragments. The last component was a quadrant 3 mm thick, 5 cm radius Lithium drifted silicon detector. This detector was thick enough to stop the ^{10}C daughter nuclei within the energy range of interest. It also stopped other fragments of similar mass and velocity, therefore measuring the energy of these particles. Particle identification was achieved by plotting the energy loss in the thin silicon detector against the energy measured in the thick Si(Li) detector.

All silicon detectors exhibit a current in the absence of any incoming particles. This current is due to thermal movement of electrons and holes in the presence of impurities and lattice defects. Since this is essentially a diffusion effect and ultimately

dependent upon temperature, the fragment telescope was cooled to -20° to lower the thermal noises in the silicon detectors. By reducing the noise within the detector, the signal to noise ratio was improved which in turn improved the energy resolution of the detector.

The fragment telescope had to be shielded during the proton calibrations of the MFA. The fragment telescope was mounted on two rods which would allow one to move it closer or further from the proton detectors. A thick copper plate was mounted such that once the telescope was pulled away from the MFA, one could swing the copper plate in front of the telescope and stop all incoming protons, thus protecting the telescope.

The fragment identification spectra exhibited some smearing of the fragments. This effect can be seen in Figure 3.7. The horizontal tail on the ^{12}N fragments is due to incomplete charge collection within the silicon energy detector. A spread at the bottom edge of the ^{12}N fragments is also present in Figure 3.7. This spread is due to two effects within the silicon ΔE detector. The first contribution is from the incomplete charge collection effect similar to that of the energy detector. The second contribution arises from lattice defects within the ΔE detector which makes it possible for a fragment to pass through these sites without interacting completely with the detector, resulting in a spread in energy loss. This effect did not create a problem for the energy detector because the fragments were stopped in that detector, thus losing all their energy.

3.3 Calibration Beams

3.3.1 Proton Beams

Molecular beams of 70 MeV/nucleon $^{3}(D\text{-}H)^{+}$ and 30 MeV/nucleon $^{5}(H\text{-}He)^{+}$ were used to calibrate the proton detectors. The beams were extracted from the K1200 cyclotron and passed through a 5 mg/cm^2 aluminum stripper foil breaking the molecular beam into its individual components. Separation of the protons from the other components, i.e. He or D, was achieved through the A1200 mass separator and the protons were then transported to the tail of the RPMS.

The above procedure provided proton beams of 70 MeV and 30 MeV at the secondary target position. Since the proton energy range of interest extended from 10 MeV to 70 MeV, degrader ladders were placed in the chambers at the tail of the RPMS to degrade the proton beams to within the desired range. The ladder in the first chamber contained 600, 1200, and 2400 mg/cm^2 thick aluminum degraders and the second chamber contained 200, 400, and 600 mg/cm^2 aluminum degraders. By using these degraders in combination with each other and the two proton beams, calibration points were obtained covering proton energies from 12 MeV to 70 MeV. The gold foil in the target ladder was used to elastically scatter the protons to irradiate all pixels of the ASI and the MFA.

3.3.2 Carbon Beams

Calibration of the fragment telescope was achieved by using beams of ^{10}C at 44.63 MeV/nucleon and ^{11}C at 46.42 MeV/nucleon and 35.89 MeV/nucleon. These fragments were produced in the fragmentation of the primary ^{16}O beam in the primary target at the front of the A1200, therefore no additional beams were tuned in the cyclotron. The 35.89 MeV/nucleon ^{11}C beam had the same rigidity as the ^{12}N beam, therefore only the RPMS had to be retuned. The degraders within the degrader ladder of the second chamber were used with the above beams to obtain calibration points for carbon isotopes with total energies from 110 to 510 MeV.

3.4 Electronics

Figure 3.10 shows a schematic diagram of the electronics setup. Two separate modes were used in the electronics, one for tuning and calibration, and one for the coincidence runs during the main part of the experiment. The difference between these two modes was the method the ΔE1, PPAC1, and PPAC2 were integrated into the electronics. The fragment telescope was shielded during the tuning of all beams and the proton calibration phase. Similarly, the ASI and MFA were shielded during the tuning of the beams. Therefore an alternate source was needed to generate the master gates and the "or" of the signals from PPAC1, PPAC2, and ΔE1 detectors was used for this purpose. This signal, represented by the dashed line in Figure 3.10, was taken out during the coincidence runs of the experiment.

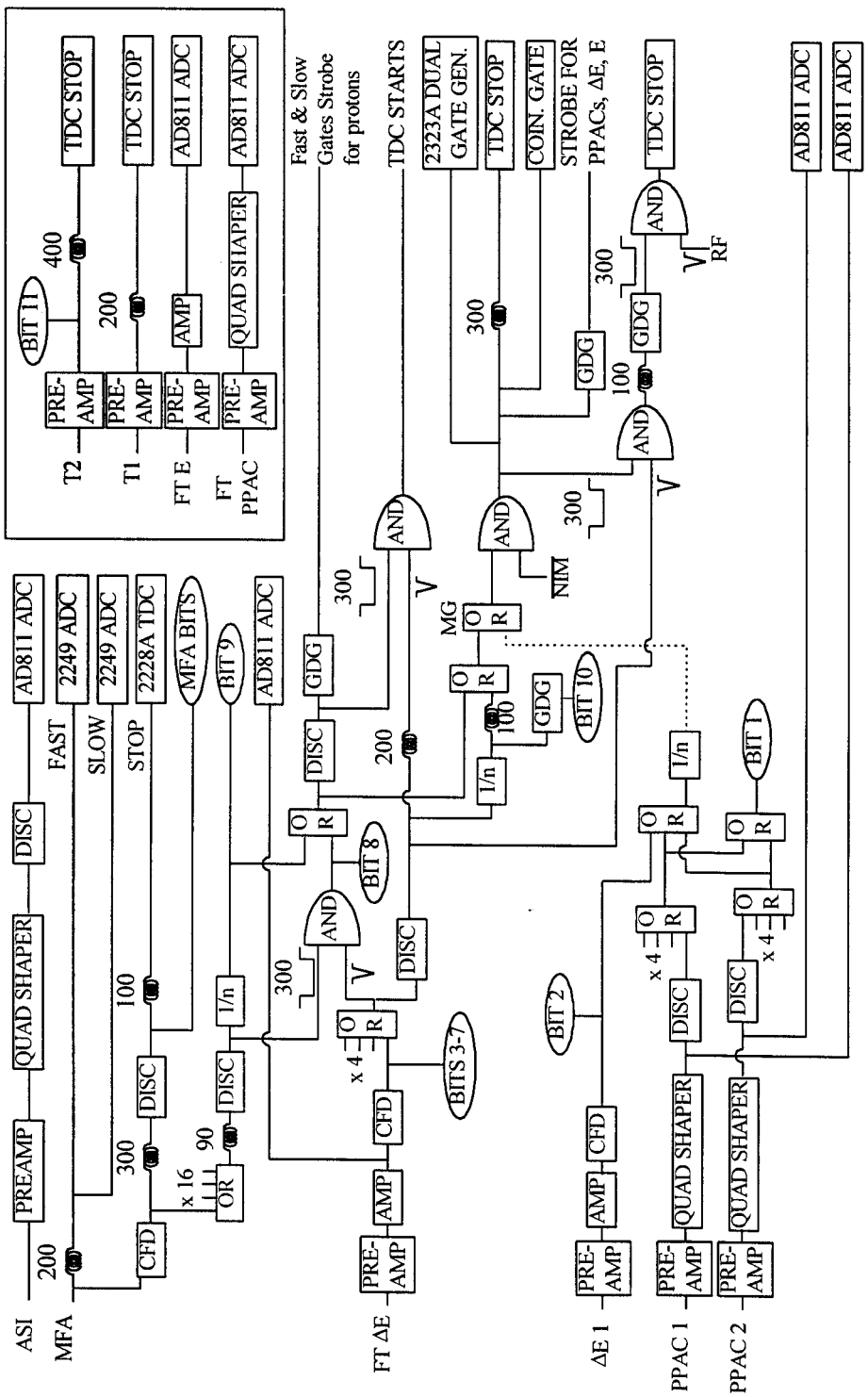

Figure 3.10: Schematic diagram of the electronics. All times are in nanoseconds.

The coincidence mode was used to detect the decay products of the unstable nuclei, i.e. protons and daughter nuclei. In coincidence experiments it is necessary to subtract the "random" coincidences from "real" coincidences. In the present measurement, random coincidences are events where a proton and daughter nucleus are seen in coincidence but did not originate from the same decay. These random events can be identified by timing against the radio frequency (RF) of the cyclotron. Uncorrelated events are evenly spread in time resulting in several equal peaks separated in time by the RF frequency whereas correlated events result in one peak only. However, this main peak also contains contributions from the uncorrelated events which can be subtracted by using the average of the other uncorrelated peaks.

Since the coincidence rate was very small, scaled down proton and fragment singles were taken simultaneously with the coincidence events to obtain the necessary statistics for particle identification.

The "or" of the proton signals from the MFA created a wide 300 ns signal indicating the detection of a proton. The "or" of the fragment ΔE detectors produced a narrow 50 ns output pulse timed to fall within the proton signal at the input of the coincidence "and" unit, thus providing a coincidence signal timed on the arrival of the fragments. The "or" of the coincidence output with the scaled down proton singles provided coincidence information timed on the fragments, and proton singles timed on the protons. The "and" of this output with the delayed "or" of the fragments provided a delayed coincidence signal timed on the fragments. This signal was then used to start all the TDCs. Figure 3.11 shows a logic diagram which depicts the procedure described

above. It was necessary to time the coincidence output on the fragments since this provided the "start" signal for the TDC units which were "stopped" by the arrival of the protons.

The "or" of the scaled down fragment singles with the "or" of the scaled down proton singles and the coincidences produced the master gate which was enabled by the computer "not busy" to generate the mater-gate-live.

The 80 channels of the ΔE signals from the ASI were amplified through a preamplifier and a shaping amplifier and fed into peak sensing ADCs. The 16 energy signals from the MFA were each separated into three parts. Two of the signals were taken to charge integrating ADCs (QDCs). A short gate was applied to one QDC covering the fast part of the signal and a long gate was applied to the other covering the whole signal, thus creating ΔE and E signals which were used for particle identification. The fast and slow gates for the protons were obtained from the "or" of the coincidence and the scaled down proton singles. The third signal from the MFA was used to stop the MFA TDCs to provide timing for the protons.

The coincidence gate and the strobes were generated from the master-gate-live signal. The RF time was obtained from the "and" of a narrow fragments signal with a wide master-gate-live signal to produce a wide pulse timed to contain the RF pulses. The TDC stop for the RF was obtained from the "and" of the RF and the wide pulse.

The inset at the top right corner of Figure 3.10 shows the remaining signals such as the FTPPAC and fragment telescope energy detector which were amplified and fed into peak sensing ADCs. T1 and T2 were the beam-line timing detectors at the end of the

A1200 and in the first chamber at the tail of the RPMS, respectively. These detectors were used only during the tuning of the beams.

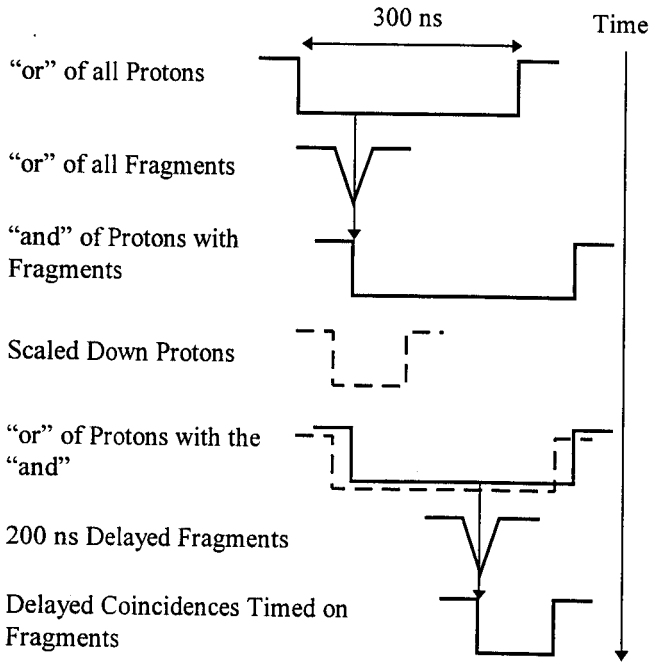

Figure 3.11: Logic signal diagram for the creation of the TDC common start signal.

3.5 Data Acquisition

The CAMAC electronics were used inside the experimental vault for the data acquisition. A front end code was written specifically for this experiment to control the CAMAC units. This code instructed the front end to read specific modules based on an array of bits received from the two bit registers used in the electronics. One bit register consisted of 16 bits, one for each detector in the MFA. Upon receiving these bits, the front end proceeded to read the corresponding channel of the MFA and all 80 channels of

the ASI. The second bit register contained information for several different detectors. Bit 1 was generated by PPAC2 and controlled the readout of the PPAC1 and PPAC2 signals. Bit 2 was generated by ΔE1 to read ΔE1. Bits 3 through 7 were generated by the four quadrants of the fragment telescope ΔE detector to read the corresponding channel in the ΔE detector, the FTPPAC, and all four channels of the fragment telescope E detector. Bit 8 was generated by the "and" of the protons with the fragments representing the coincidence bit which triggered the reading of all the proton, and RF TDCs. Bits 9 and 10 were the proton and fragment singles bits respectively. These were present to measure the ratio of singles to coincidences. Bit 11 was produced by the timing scintillator in the first chamber at the tail of the RPMS and it was used to read the beam-line timing detector and the timing scintillator TDCs.

The incoming data stream was recorded on 8 mm tapes for off-line analysis. The program SARA [She94] was used to create histograms of the parameters within the data stream which could then be displayed for online monitoring and data analysis.

Chapter 4

Data Analysis

4.1 Analysis Software

The data was analyzed using the programs SARA [She94] and DAMM [Mil92]. SARA was used to read the 8 mm tapes containing the data and to create histograms for viewing spectra of interest. To speed up the data analysis, the coincidence data were filtered onto disk using SARA. The filtered data was created by imposing certain criteria based on software gates defined on spectra in SARA. These software gates were imposed on the protons, fragments, PPAC2, and FTPPAC spectra. A valid event was defined as an event which satisfied all the aforementioned gates. These events were then filtered and put on disk for faster retrieval and analysis.

SARA uses a set of predefined parameters based on the electronics used in the experiment. These parameters can be used to create one and two dimensional histograms. SARA also allows for the definition of "pseudo" parameters based on the predefined parameters which can be histogrammed. For example, histograms of the calibrated energies and the decay energies were created by this method.

The histograms created by SARA were converted into a format readable by DAMM. Direct comparisons between the data and simulations were made by converting the output of the simulations to DAMM format also.

4.2 Energy Calibrations

4.2.1 Proton Detectors

The protons from the molecular beams in conjunction with several aluminum degraders of known thickness were used to calibrate the MFA. A 94 mg/cm^2 Au target was used to elastically scatter the protons onto the proton detectors. The energy loss of the protons in the degraders were calculated using the code TRIM91 [Bie80].

Table 4.1 shows the degrader combinations used in the calibration and the degraded proton energies obtained. The first three rows represent calibration energies using the 35 MeV proton beam, while the remainder were obtained from the 70 MeV proton beam. It should be pointed out that the energies listed in Table 4.1 represent proton energies out of the target and do not include energy loss in the ASI nor the material used to create a light-tight environment for the MFA. Therefore, the proton energies measured from the actual decays represent the energy out of the target since the energy loss within materials after the target are folded into the calibrations.

The peaks obtained during the proton calibrations of the MFA exhibited lower resolutions than were expected. This was caused by the difference in light collection within the photo-multiplier tubes, effectively introducing a position dependence on the

detection of the protons. Figure 4.1 shows the detected pulse height in channels versus the position of the event where the radial number 1 corresponds to the outermost ring and the radial number 15 corresponds to the innermost ring. In the absence of any position dependence the spectrum in Figure 4.1 would be a horizontal line. This position dependence worsens the energy resolution of the MFA, therefore a position dependent energy calibration was performed. This was achieved by calibrating the MFA separately for each radial strip of the ASI. Figure 4.2 shows the calibration curve obtained for one of these pixels. Due to the geometry of the MFA, high energy protons near the outside edge of the plastic detector punched through the detectors leaving only a fraction of their total energy. These events were identified by gating on the outer three rings of the ASI and were excluded from the analysis. The proton energy calibration spectra were fitted using a second order polynomial and the fit parameters were used to convert channel numbers into proton energies. The average energy resolution of the proton detectors was about 5%.

Table 4.1: Degrader combinations and proton energies obtained during the calibration of the MFA. The 35 MeV proton beam was used to obtain the values in the first three rows. The remainder were obtained using the 70 MeV proton beam.

Degraders (mg/cm^2)	Proton Energy (MeV)
1213 Al + 94 Au	11.96
600 Al + 94 Au	25.49
94 Au	34.25
2400 Al + 600 Al	41.96
2400 Al + 389 Al	44.28
2400 Al + 94 Au	47.79
1213 Al + 600 Al	53.97
1213 Al + 389 Al	55.90
1213 Al + 94 Au	58.83
1213 Al	59.34
600 Al + 94 Au	63.96
600 Al	64.43
389 Al	66.10
94 Au	68.63

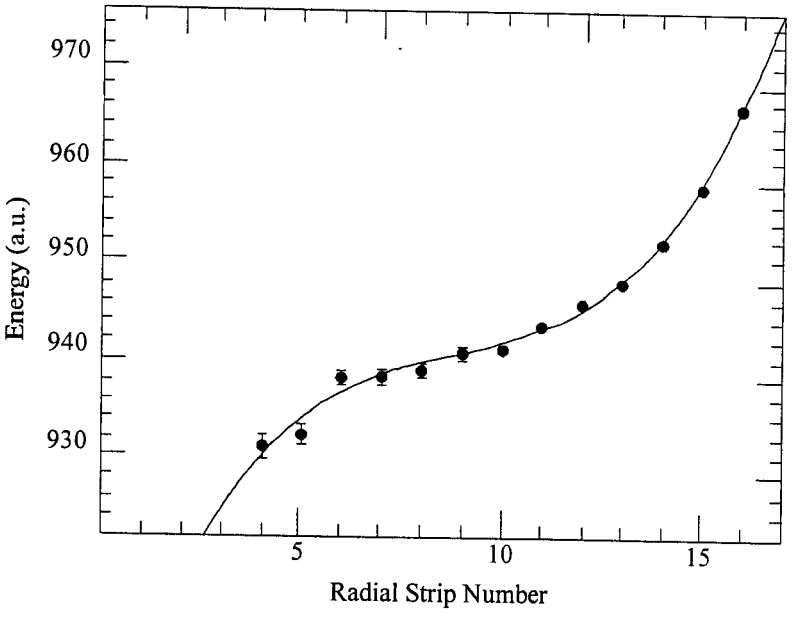

Figure 4.1: Proton energy versus the radial strip of the ASI for 63.96 MeV protons.

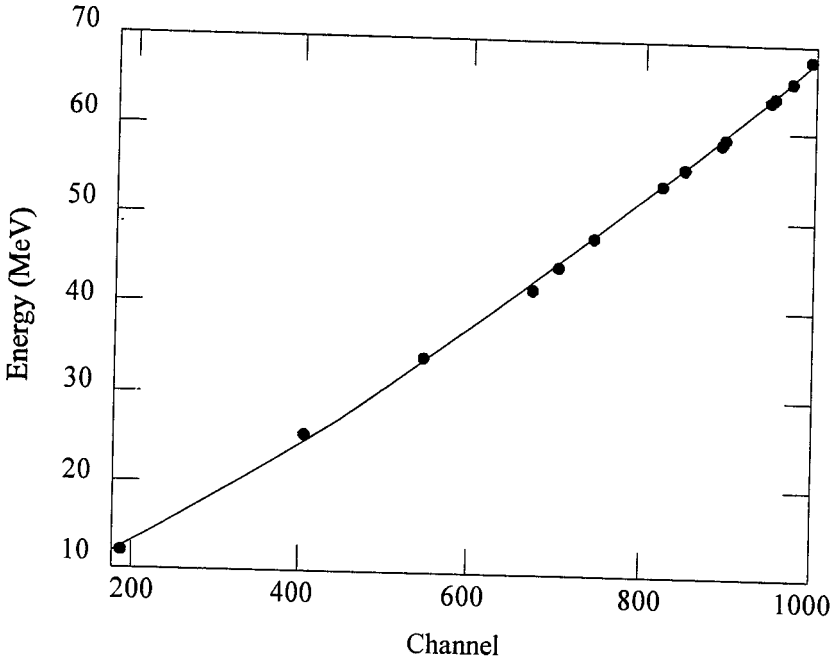

Figure 4.2: Energy calibration of the MFA gated on one ASI pixel.

4.2.2 Fragment Detectors

The thick silicon detector in the fragment telescope, used to measure the total energy of heavy particles, was calibrated with beams of ^{10}C and ^{11}C. By modifying the A1200 rigidity two beams of ^{11}C at 35.89 MeV/nucleon and 46.42 MeV/nucleon, and one beam of ^{10}C at 44.63 MeV/nucleon were separately obtained. The same aluminum degraders as in the proton calibrations were used with these beams to provide additional calibration points. Table 4.2 shows the degraders and the corresponding total energies calculated from TRIM91 [Bie80]. Similar to the protons, these energies reflect the energy of the particles out of the target and do not include the energy loss in the FTPPAC and the ΔE detector.

Table 4.2: Energy calibration points obtained for the fragment telescope.

Beam	Aluminum Degraders	Total Energy (MeV)
395 MeV ^{11}C	-	395
511 MeV ^{11}C	-	511
511 MeV ^{11}C	389 mg/cm^2	344
511 MeV ^{11}C	600 mg/cm^2	219
446 MeV ^{10}C	-	446
446 MeV ^{10}C	389 mg/cm^2	268
446 MeV ^{10}C	600 mg/cm^2	109

The four calibration spectra, one for each quadrant of the thick silicon detector, were fitted and the fit parameters were used to convert the channel numbers into particle energies. Figure 4.3 shows the fit obtained from the calibration of one of the quadrants of the fragment telescope. The energy resolution of the fragment detectors was determined to be about 3%.

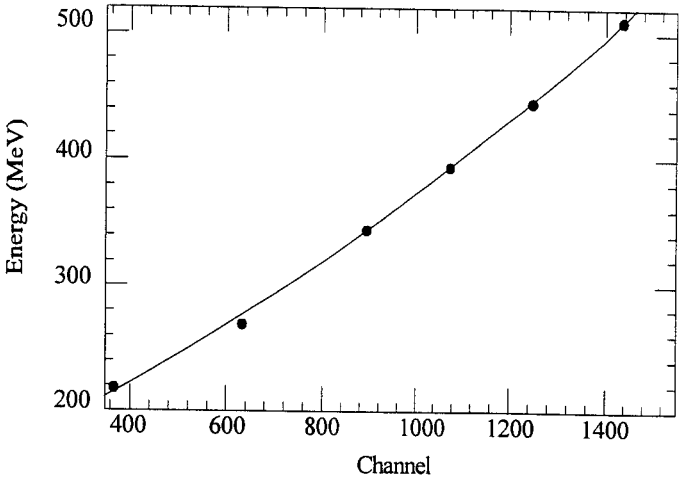

Figure 4.3: Calibration spectrum for one quadrant of the fragment silicon detector.

4.3 Position Calibrations

4.3.1 Fragment Telescope PPAC

The FTPPAC was calibrated using a thin aluminum mask with holes in an asymmetric pattern. The asymmetric pattern is required to ensure the correct orientation of the mask relative to the axis and direction of the beam. The calibration was performed with an alpha source at a distance of about 20 cm in front of the mask. Figure 4.4 shows the FTPPAC spectrum obtained during the calibration. The holes in the mask had a diameter of 2.34 mm which was used to obtain the position resolution, and the distance between each adjacent hole was 6.35 mm which provided the position calibration. A Monte Carlo simulation was written to fit the individual peaks in the FTPPAC using the position resolution as a variable of the fit. This yielded a value of 1.0 mm full width at half maximum (FWHM) for the position resolution of the FTPPAC.

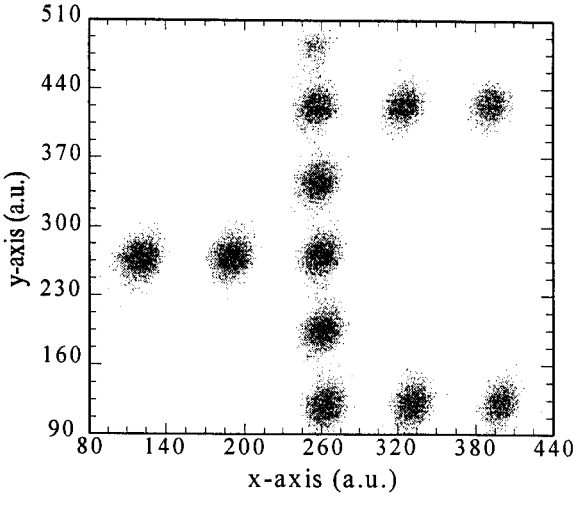

Figure 4.4: Calibration spectrum for the fragment telescope PPAC.

The data acquisition recorded events on the condition that the thin silicon ΔE detector of the fragment telescope fired. This detector was subdivided into four quadrants with a thin dead layer between each active surface. Therefore, fragments hitting these dead layers were not recorded and thus resulted in gaps in the FTPPAC spectrum. Figure 4.5 shows the spectrum of the FTPPAC projected on the x-axis. This gap was used to define the center of the x-axis. The same method was applied to the projection of the FTPPAC spectrum on the y-axis to obtain the center in the vertical direction.

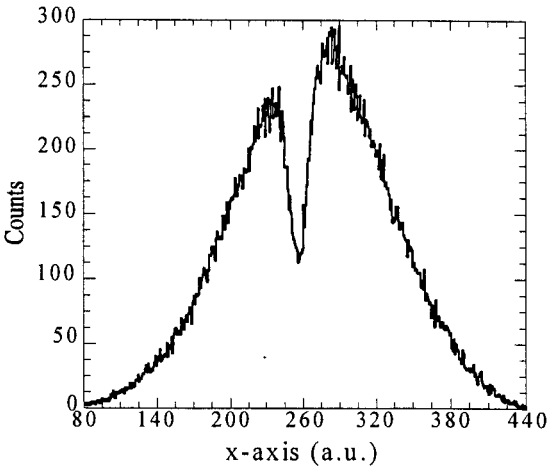

Figure 4.5: Fragment telescope PPAC spectrum gated on fragment telescope silicon and projected onto the x-axis.

4.3.2 Beamline PPACs

PPAC2 was calibrated and centered using the same technique applied to the FTPPAC. The position resolution measured for this PPAC was 1.0 mm FWHM.

Position calibration for PPAC1 was carried out using the same mask as PPAC2 and a position resolution of 1.3 mm FWHM was observed. However, due to the large distance between PPAC1 and the fragment telescope, the center of PPAC1 could not be found by the same method used for PPAC2 and the FTPPAC. A line was projected through the center of PPAC2 and FTPPAC which also crossed the center of PPAC1 at an unknown channel number on PPAC1. A similar line was reconstructed for each beam particle using the FTPPAC and PPAC2 in the absence of a target. By plotting the relative position of the beam particles in PPAC1 to the projected center of PPAC1, a spectrum was obtained with a peak denoting the center of the detector.

4.4 Particle Identification

The protons in the ASI and MFA had to be identified and separated from other light charged particles entering the detectors. The combination of fast and slow signals from the MFA allowed fragment identification by pulse shape discrimination. The fast plastic produced a pulse with a fast rise time corresponding to an energy loss, whereas the slow plastic produced a pulse with a slow rise time corresponding to the total energy of the particle. By plotting the total area under the signal versus the area of the fast component, the ΔE - E plot shown on the left in Figure 4.6 was obtained. Alternatively, the ΔE signal form the ASI could be used instead of the fast plastic signal. Figure 4.6 shows the ΔE - E spectrum (right) obtained using the ASI signal. Both spectra in Figure 4.6 exhibit excellent separation between the protons, deuterons and tritons (p, d, t).

The fragments were identified using the ΔE - E spectra obtained from the thin silicon versus the thick silicon detector in the fragment telescope. Figure 4.7 shows the raw ΔE - E spectrum (left) and the same spectrum with a proton coincidence condition imposed on it (right). Due to the large number of ^{12}N and ^{13}O from the beam, other fragments can not be seen in the raw ΔE - E spectrum. By gating on protons the number of observed ^{12}N and ^{13}O fragments in the ΔE - E spectrum was reduced dramatically allowing the rest of the fragments to show more clearly. The ^{12}N in the gated spectrum was identified from the position of the ^{12}N beam in the raw ΔE - E spectrum. Carbon isotopes were identified from the ΔE - E spectra of the ^{10}C and ^{11}C calibration beams.

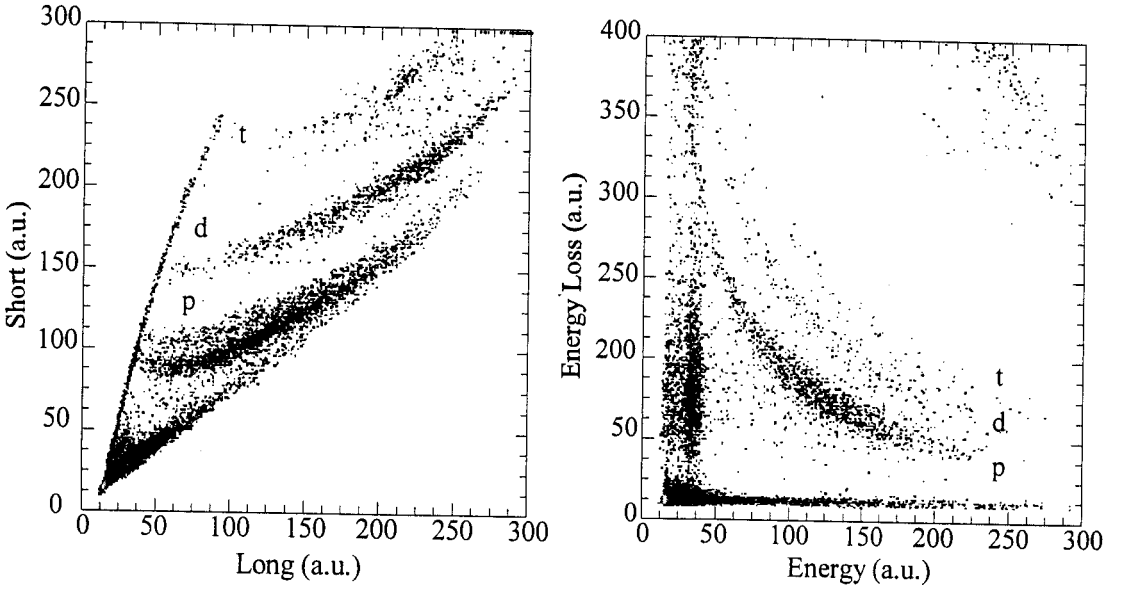

Figure 4.6: Total energy versus energy loss (left) and long versus short (right) spectra used to identify the protons.

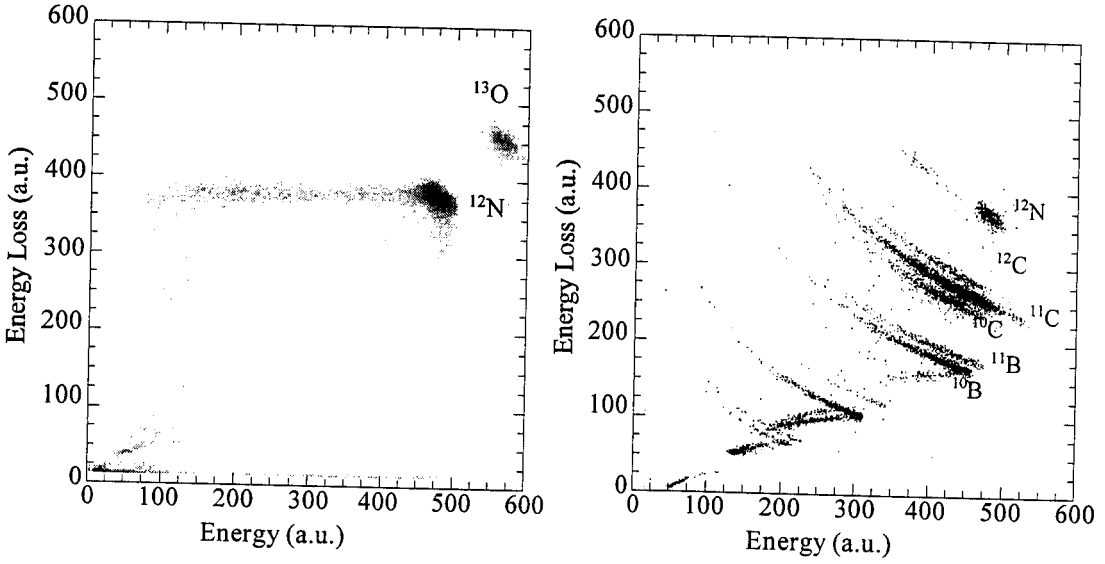

Figure 4.7: Energy loss versus energy spectra for the fragment telescope. Raw spectrum (left) and gated on all protons (right).

4.5 Contamination

One possible source of contamination in the data were events generated not within the target, but from the target frame or the beam pipes. An empty target frame was used to reproduce such events. The empty target frame would only reproduce reactions that were not target related and would result in a spectrum that could be subtracted from the data. However, the contribution of these events to the data was less than 1% and a subtraction was not necessary.

4.6 Decay Energy

In a proton decay of the form $X \rightarrow D + p$, the laboratory rest mass of the decaying particle X can be calculated using

$$M_X^2 = M_p^2 + M_D^2 + 2(T_p + M_p)(T_D + M_D) - 2\sqrt{(T_p^2 + 2T_pM_p)(T_D^2 + 2T_DM_D)}\cos\theta \quad (4.1)$$

where M is the rest mass (including any excitation energies), T is the kinetic energy of the particles in the laboratory frame, and θ is the laboratory opening angle between the proton and the daughter nucleus D. Equation 4.1 is a relativistic reconstruction of the mass of the parent nucleus using the experimental observables kinetic energy and opening angle. The decay energy can be calculated using Equation 4.1 in

$$E_{decay} = M_X - M_p - M_D$$

If the mass of the daughter nucleus is known, one can reconstruct the mass of the state from which the decay occurred. Although this allows the calculation of the decay energy of a state, it does not provide information about neither the decaying state nor the state within the daughter nucleus.

The kinetic energy of the protons and fragments were obtained from the energy calibrated spectra of the proton and fragment detectors respectively. The laboratory opening angle between the proton and the fragment were reconstructed from three quantities (i) the position at which the decay occurred, (ii) the position of the protons in the ASI, and (iii) the position of the fragments in the FTPPAC. Figure 4.8 shows the geometrical reconstruction of the opening angle. Due to the close proximity of PPAC2 to the target (~2 cm) the origin $(x_o,y_o,0)$ was measured directly from PPAC2. The proton

position $(x_p,y_p,199)$ was obtained from the pixels of the ASI, and the fragment position $(x_D,y_D,621)$ was measured by the FTPPAC where all distances are in millimeters. From these positions, the opening angle θ can be calculated by using the definition of a vector dot product to obtain

$$\cos\theta = \frac{(x_p - x_o)(x_D - x_o) + (y_p - y_o)(y_D - y_o) + (199 \times 621)}{\sqrt{[(x_p - x_o)^2 + (y_p - y_o)^2 + 199^2][(x_D - x_o)^2 + (y_D - y_o)^2 + 621^2]}}. \quad (4.2)$$

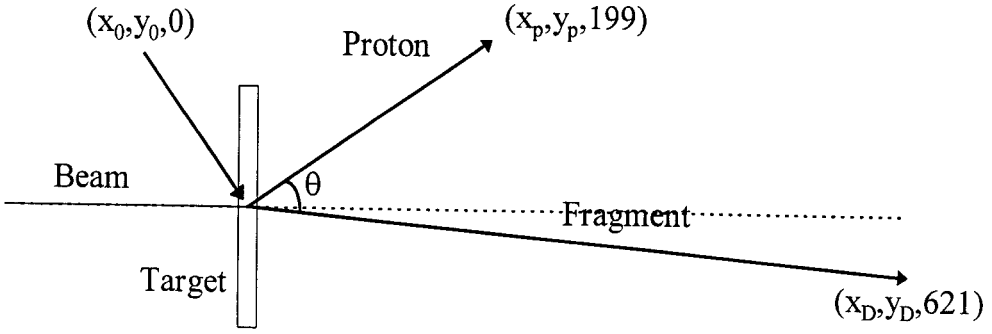

Figure 4.8: Vector diagram of a proton decay. All distances are in millimeters.

4.7 Monte Carlo Simulations

A Monte Carlo simulation was written to include the experimental observables describing the beam, the energy loss within the target, and the detector geometry. In addition, theoretical treatments of the transfer reaction and the decay were incorporated in this code. The body of this code and a brief description of each unit therein is given in Appendix A.

4.7.1 Secondary Beam

The first step within the simulation was a description of the ^{12}N beam. The kinetic energy of the ^{12}N beam was calculated from the final A1200 rigidity to be 40.77 MeV/nucleon. The spread in energy was calculated using the 3% setting of the momentum slits in the A1200 which corresponds to a 6% spread in energy. Although a secondary beam has a Gaussian distribution, the FWHM of the distribution was about 10% for ^{12}N [Win92] compared to the 3% cut imposed by the momentum slits. Therefore, a flat distribution is a good approximation for the energy distribution.

The position spectra from PPAC1 and PPAC2 were converted into Gaussian distributions by measuring the position and width of the beam in each PPAC. These parameters were then used in the simulation to calculate the trajectory of the beam.

4.7.2 Interactions in the Target

Due to the finite thickness of the target, the exact location of the interaction could not be measured experimentally, however the probability of an interaction in the target along the beam trajectory is constant and was included in the simulations as such.

The energy loss of the ^{12}N beam, the proton, and all daughter nuclei of interest within the ^{9}Be target, as a function of distance traveled in the target, were calculated with the code STOPI [Mil88]. The energy loss for the parent nuclei was not included because of their negligible distance of travel ($\sim 10^{-19}$ mm).

The calculated distances included all the angles as the particles traversed the target. The angle of the incoming beam was calculated from PPAC1 and PPAC2 while the angle of the proton and daughter nuclei were calculated from the scattering angle and the decay, as described in the next sections.

4.7.3 The Reaction

Figure 4.9 depicts the kinematics of the ^{12}N interaction in the target to produce the fragments of interest. The scattering angle θ' was simulated to describe the distribution shown in Figure 4.10 where θ_c was chosen to be 0.05 radians and the slope of the tail of the probability distribution was set to 37.56 deg^{-1}. These values were obtained from experimental studies of transfer reactions for nuclei with similar mass and charge [Oer70].

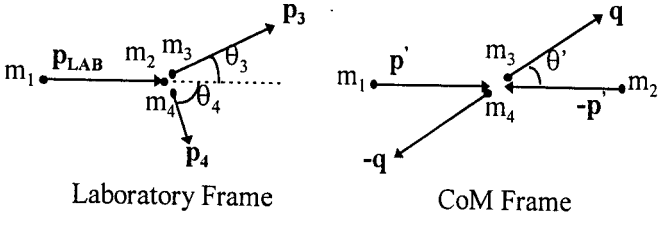

Figure 4.9: Scattering reaction between projectile and target in laboratory and center of mass frames.

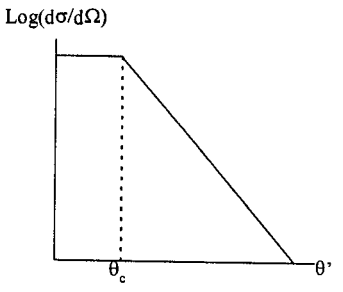

Figure 4.10: Distribution used to simulate the scattering angle in the laboratory frame.

The magnitude of the momentum **q** in Figure 4.9 is given by

$$q^2 = \frac{(W^2 - m_3^2 - m_4^2)^2 - 4m_3^2 m_4^2}{4W^2} \tag{4.3}$$

where

$$W^2 = m_1^2 + m_2^2 + 2m_2\sqrt{p_{LAB}^2 + m_1^2} \tag{4.4}$$

is the square of the total energy in the center of mass frame. Throughout these calculations *c* is set to 1. By using the Lorentz transformation parameters for the center of mass v_{cm} and γ_{cm} defined as [Jac75]

$$\overline{v}_{cm} = \frac{\overline{p}_{LAB}}{m_2 + \sqrt{p_{LAB}^2 + m_1^2}}, \qquad \gamma_{cm} = \frac{m_2 + \sqrt{p_{LAB}^2 + m_1^2}}{W} \tag{4.5}$$

one can calculate the laboratory scattering angle θ_3 from

$$\tan\theta_3 = \frac{v_3 \sin\theta'}{\gamma_{cm}(v_3\cos\theta' + v_{cm})} \tag{4.6}$$

and the laboratory velocity

$$v_3 = \frac{\sqrt{v^2 + v_{cm}^2 + 2vv_{cm}\cos\theta' - (vv_{cm}\sin\theta')^2}}{1 + vv_{cm}\cos\theta'} \tag{4.7}$$

where

$$v \equiv \frac{q}{q^2 + m_3^2} \ . \tag{4.8}$$

These equations define the momentum of the outgoing proton unbound nucleus. However, the laboratory angle calculated in Equation 4.6 is relative to the angle of the incoming beam. Since the beam does not always travel exactly on the center of the beam pipe, a matrix rotation was applied to transform the fragments to a frame where the z-axis lies along the center of the beam pipe.

4.7.4 The Decay

The unstable parent nuclei decay instantly into the daughter nuclei by emitting a proton. The important parameters of the decay are the decay energy and width of the state. The decay energy is incorporated by adding it to the sum of the masses of the proton and the daughter nucleus to obtain the mass of the decaying state in the parent nucleus.

The cross section for barrier penetration has a Breit-Wigner form given by

$$\sigma = N \frac{\Gamma_L(E, R_n)}{(E - E_r)^2 + \Gamma_L^2(E, R_n)/4} \tag{4.9}$$

where N is a constant used to normalize the distribution within the simulations. Due to the factor of $\Gamma_L^2(E, R_n)$ in the denominator of Equation 4.9, the center of the peak is pushed towards lower decay energies as the width of the state increases. The calculation

of the width in Equation 4.9 requires the calculation of the partial widths. The reduced width of a state γ_L is defined as

$$\gamma_L \equiv \frac{\hbar^2}{2\mu R_n}\left|\chi_L(R_n)\right|^2 . \tag{4.10}$$

Note that the reduced width depends only on the nuclear radius and angular momentum and is a constant with respect to energy. Using Equation 2.11 for the radial wave function and Equation 2.12 for the partial width of a state Equation 4.10 becomes

$$\gamma_L = \frac{\Gamma_L(E_r, R_n)}{2k_r R P_L(E_r, R_n)} \tag{4.11}$$

where E_r is the resonance energy, the penetrability is defined by Equation 2.14, and the radius and wave number are given by

$$k_r = \frac{\sqrt{2\mu E_r}}{\hbar}, \qquad R_n \equiv R_p + R_D = 1.4(1 + A_D^{1/3}) .$$

Once the reduced width has been calculated, the width $\Gamma_L(E,R_n)$ at any energy can be calculated from a rearrangement of Equation 4.11:

$$\Gamma_L(E) = 2kR_n\gamma_L P_L(E, R_n) . \tag{4.12}$$

The momenta of the proton and daughter nucleus were calculated using simplified versions of the equations discussed in Section 4.7.3. However, an isotropic distribution was used for the decay angle instead of the distribution given for the scattering angle in Figure 4.10. As in the case of the scattering, a rotation was applied to the final momenta to transform them into a frame where the z-axis lies along the center of the beam pipe. The angles calculated for the proton and daughter nucleus were used to calculate the energy-loss within the target as well as the location of interaction within the detectors.

4.7.5 Detectors

By tracing the trajectory of the protons and fragments, only those events were included when both particles hit their perspective detectors. Defective pixels within the ASI were identified in the simulations and events where a proton was detected in these strips were eliminated. The fourth segment of the fragment telescope had insufficient energy resolution and was not included in the data analysis, and thus excluded in the simulations. This procedure for incorporating the shape and position of each detector into the simulation accounted for the geometric efficiency of the detection system.

4.7.6 Decay Energy

Once the decay has been simulated and the proton and the daughter nucleus have been traced into the detectors, Equation 4.1 was used to calculate the decay energy. By varying the decay parameters within the input file, decay energy spectra were generated and fitted to the data.

4.7.7 Efficiency and Resolution

The Monte Carlo simulation code contained the geometry of the detectors, and thus was used to obtain the geometric efficiency of the experimental setup. By running a flat decay energy distribution for the decay of ^{11}N the spectrum in Figure 4.11 was obtained. Similarly, the experimental resolution was obtained from the simulations. Figure 4.12 shows the observed FWHM of the decay energy peak versus the input width

of a $1/2^+$ state at 1.9 MeV decay energy. By observing the FWHM of the observed peak at an input width of 0.0, the experimental resolution of 400 keV was obtained from Figure 4.12. The flattening off of the spectrum in Figure 4.12 is a direct effect of the geometric efficiency.

The effects of the efficiency and experimental resolution on the decay energy spectrum is shown in Figure 4.13 which was obtained from the simulation of a $1/2^+$ state at 1.6 MeV decay energy. Decay widths of 200 keV and 2.0 MeV were used to obtain the left and the right spectra, respectively. The solid lines in Figure 4.13 represent the decay energy spectrum at 100% geometric efficiency, whereas the dashed lines represent the same decay including the geometric efficiency. The dashed lines were normalized to the height of the solid lines to show the effect of the efficiency on the shape of the decay energy peak.

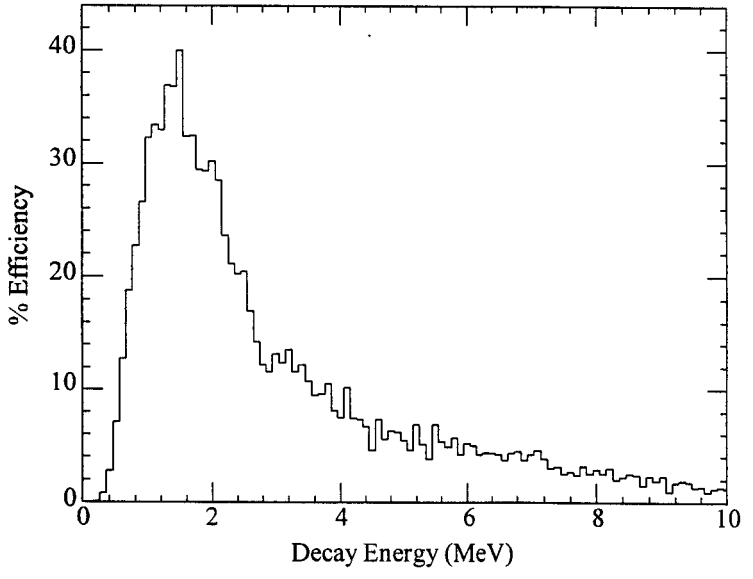

Figure 4.11: Simulated geometric efficiency of the decay of ^{11}N.

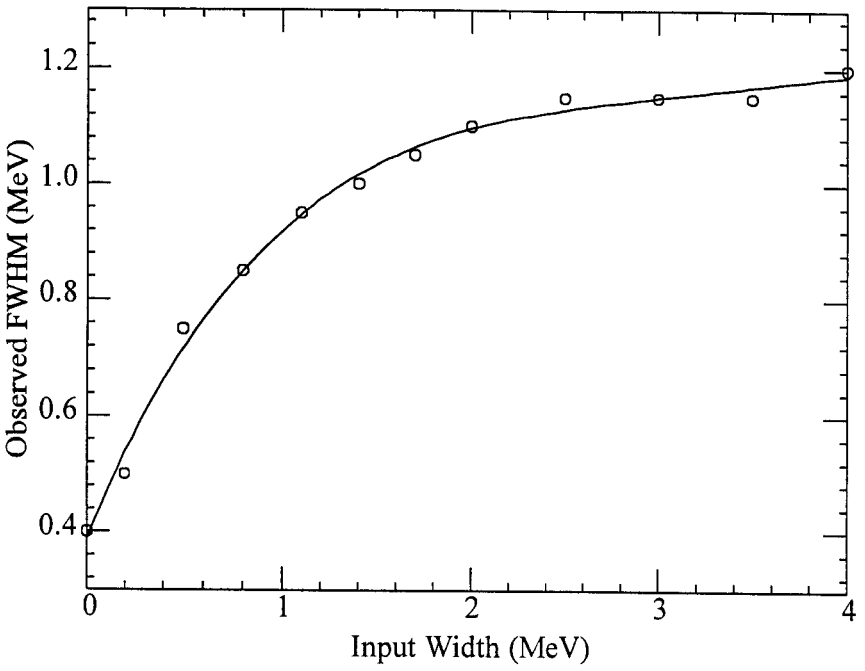

Figure 4.12: Simulated width of the decay energy peak versus the input width of a $1/2^+$ state at 1.9 MeV decay energy in ^{11}N.

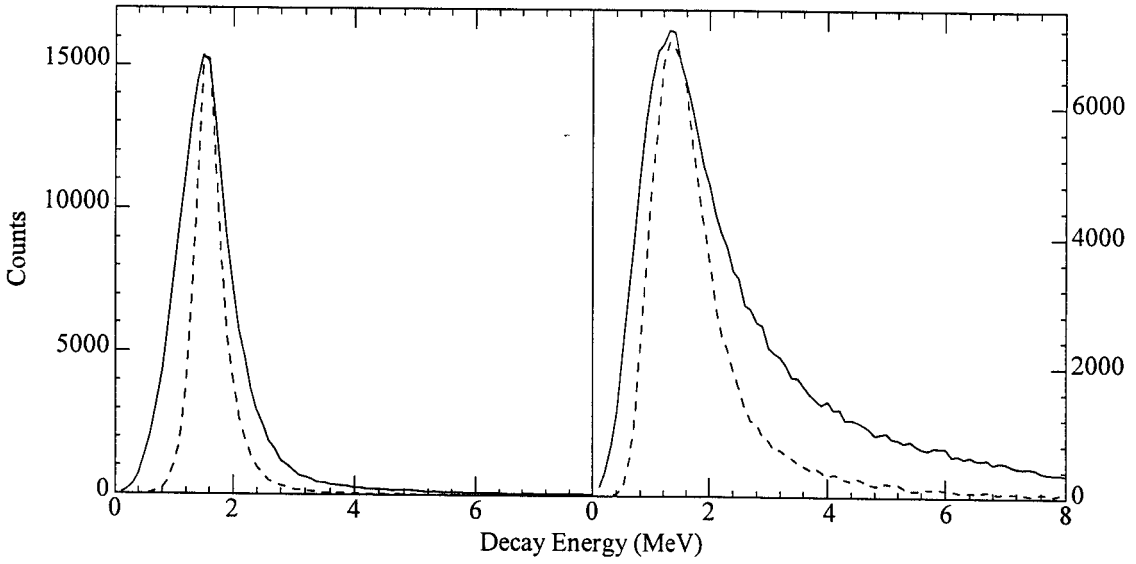

Figure 4.13: Simulated decay energy spectra for a $1/2^+$ state in ^{11}N at decay energies of 1.6 MeV. Decay widths of 200 keV and 2.0 MeV were used to obtain the left and the right spectra, respectively. The solid lines were obtained at a geometric efficiency of 100%. The dashed lines include the experimental geometric efficiency and were normalized to the height of the solid lines for comparison.

4.8 Fitting of Data

Spectra obtained from the data were interpreted by comparing them to the results of the simulations. The quality of these fits were calculated using the reduced χ^2 which is defined as

$$\chi^2_R = \frac{1}{N-M}\sum_{i=1}^{N}\frac{\left(y_i - \sum_{j=1}^{M} y'_{i,j}\right)^2}{\sigma_i^2} \tag{4.13}$$

where N is the number of points used in the fit, M is the number of free parameters, y_i is the number of counts in the i^{th} channel of the data, $y'_{i,j}$ is the number of counts in the i^{th} channel of the j^{th} simulated peak, and σ_i is the uncertainty in y_i.

Within the Poisson distribution the mean of the reduced χ^2 (hereafter referred to as χ^2) is equal to 1 with a variance of 1. This implies that a good fit would yield a value of 1 for the χ^2 and the uncertainties of the fit can be obtained when the value of the χ^2 varies by one from the minimum. Values of χ^2 higher than one denote an inadequate fit, while values below 1 imply a fit that is better than average. One possibility for obtaining χ^2 values significantly different from 1 is in the uncertainties or error bars. If the error bars are too large, the value of the χ^2 will be smaller, and vice versa. Also, the value of χ^2 can be less than one if there are more parameters than are needed to fit the data.

The Monte Carlo simulations were run using sufficient numbers of events that statistical error bars within the simulated peaks could be ignored when normalized to the data. The χ^2 test was used to optimize the normalization of the simulations to the data.

For a general case of fitting a spectrum from the data with M number of simulated peaks, we would need M normalization constants n_j, where j is an integer from 1 to M. A slight modification to Equation 4.15 can be performed to calculate the χ^2 for this case. The $y'_{i,j}$ in Equation 4.25 must be multiplied by the normalization constants n_j thereby including the normalization constants in the calculation of the χ^2 to get

$$\chi^2 = \frac{1}{N-M}\sum_{i=1}^{N}\frac{\left(y_i - \sum_{j=1}^{M} n_j \cdot y'_{i,j}\right)^2}{\sigma_i^2}. \qquad (4.14)$$

The best possible fit would be the one with the lowest χ^2, therefore the optimum normalization constants are obtained when the χ^2, given in Equation 4.16, is minimized. The minimum of χ^2 can be found by setting the partial derivatives of the χ^2 with respect to each n_j to zero. This results in M equations of the form

$$\frac{\partial \chi^2}{\partial n_k} = \frac{1}{N-M}\sum_{i=1}^{N}\frac{(-2y'_{i,k})\left(y_i - \sum_{j=1}^{M} n_j y'_{i,j}\right)}{\sigma_i^2} = 0 \qquad (4.15)$$

where the n_j can be solved for using

$$\begin{pmatrix} \sum_i \frac{y'^{\,2}_{i,1}}{\sigma_i^2} & \sum_i \frac{y'_{i,1}\cdot y'_{i,2}}{\sigma_i^2} & \cdots & \sum_i \frac{y'_{i,1}\cdot y'_{i,M}}{\sigma_i^2} \\ \sum_i \frac{y'_{i,2}\cdot y'_{i,1}}{\sigma_i^2} & \sum_i \frac{y'^{\,2}_{i,2}}{\sigma_i^2} & \cdots & \sum_i \frac{y'_{i,2}\cdot y'_{i,M}}{\sigma_i^2} \\ \vdots & \vdots & \ddots & \vdots \\ \sum_i \frac{y'_{i,M}\cdot y'_{i,1}}{\sigma_i^2} & \sum_i \frac{y'_{i,M}\cdot y'_{i,2}}{\sigma_i^2} & \cdots & \sum_i \frac{y'^{\,2}_{i,M}}{\sigma_i^2} \end{pmatrix} \begin{pmatrix} n_1 \\ n_2 \\ \vdots \\ n_M \end{pmatrix} = \begin{pmatrix} \sum_i \frac{y_i \cdot y'_{i,1}}{\sigma_i^2} \\ \sum_i \frac{y_i \cdot y'_{i,2}}{\sigma_i^2} \\ \vdots \\ \sum_i \frac{y_i \cdot y'_{i,M}}{\sigma_i^2} \end{pmatrix}.$$

Solving the above simultaneous equations will provide a solution for the normalization factors that minimize the χ^2.

Chapter 5

Results and Discussion

5.1 Decay Energies

In addition to the one neutron stripping reaction ^{9}Be(^{12}N, ^{11}N), one neutron pickup reactions populating ^{13}N, one proton pickup reactions producing ^{13}O, and two proton stripping reactions creating ^{10}B were also recorded. Evidence for the production of these nuclei can be seen in Figure 4.7 (right) where the daughter nuclei of these fragments are seen in coincidence with protons. These nuclei all have proton unbound excited states [Ajz88, Ajz90,Ajz91] and were used to test and calibrate the method.

Some of the input parameters of the simulations, i.e. energy resolution, could be adjusted by comparing the results of the simulations for these nuclei to the data. Once all the input parameters were optimized for these test cases, they were applied to ^{11}N.

5.1.1 Decay of ^{13}N

Although the ground state of ^{13}N is bound to proton decay, all excited states of this nucleus are proton unbound. Applying Equation 4.1 to the ^{12}C fragments detected in

the fragment telescope in coincidence with protons, the decay energy of ^{13}N was calculated. The raw decay energy spectrum obtained for ^{13}N is shown in Figure 5.1.

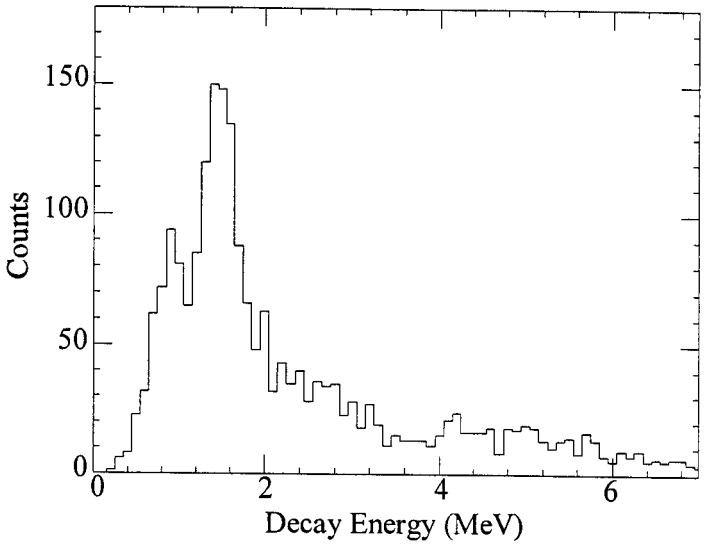

Figure 5.1: Raw decay energy spectrum of ^{13}N.

Figure 5.2 shows a comparison of the data (left) to the simulation (right) for the total kinetic energy of the ^{12}C daughter nuclei versus the decay energy for ^{13}N. The dashed line at fragment energy of 360 MeV shows the low end cut off energy obtained from the simulations. However, the ^{12}C energy spectrum obtained from the data (left) exhibits a tail extending into regions below 360 MeV. The absence of such a tail in the simulations indicates that this tail is due to background events.

By applying a software gate to the fragment energy spectrum to contain all events with ^{10}C fragment energies lower than 360 MeV, the background spectrum shown in Figure 5.3 was obtained. This background was normalized to the 4.0 to 7.0 MeV region

of the decay energy spectrum, containing events with ^{12}C energies above 360 MeV, and subtracted. The resulting background subtracted decay energy spectrum for ^{13}N is shown in Figure 5.4, where the statistical error bars have been included. A prominent peak at a decay energy of about 1.5 MeV can be seen.

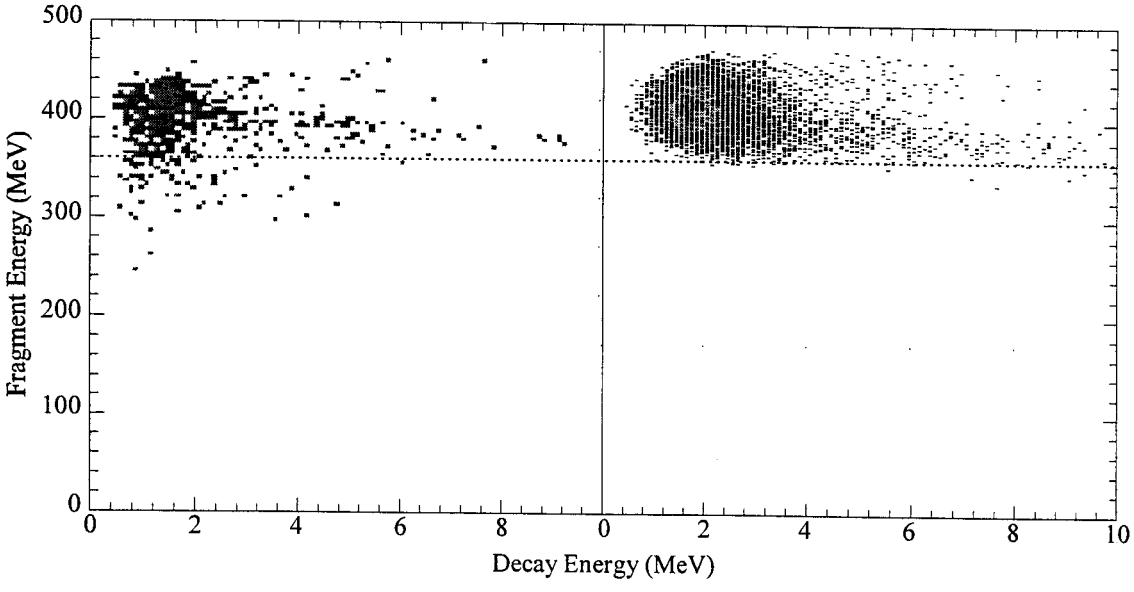

Figure 5.2: ^{12}C fragment energy versus decay energy data (left) and simulation (right). Points below the 360 MeV dashed line are background events.

Figure 5.5 shows the level diagram for ^{13}N [Ajz91]. The proton decay threshold is at 1.944 MeV, therefore a decay energy of about 1.5 MeV would correspond to the decay of the $3/2^-$ and the $5/2^+$ states. The experimental width of about 400 keV does not allow the separation of these states. The width of the $3/2^-$ and $5/2^+$ states are much narrower than the experimental resolution and could thus be used to calculate the energy resolution of the detectors.

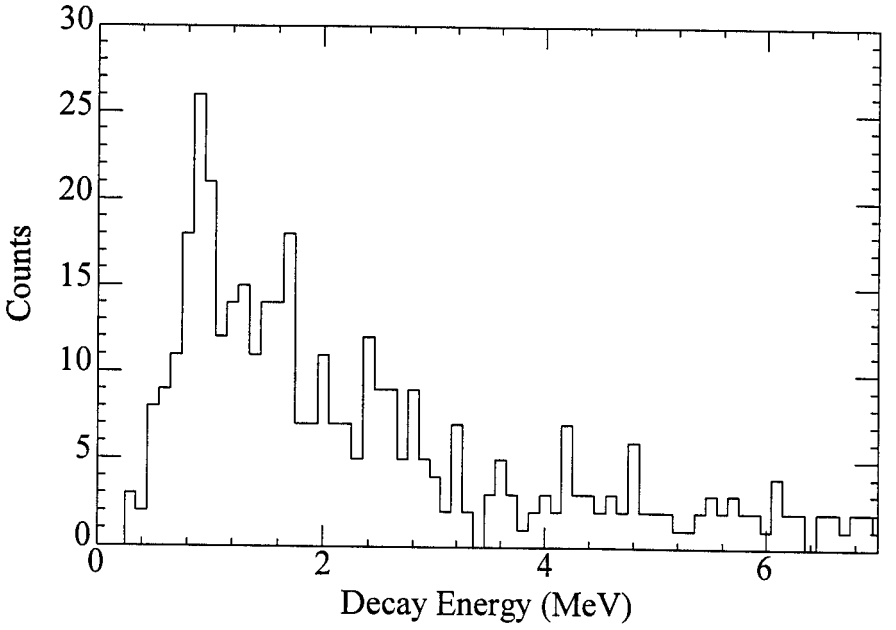

Figure 5.3: Background spectrum of ^{13}N. This spectrum was obtained by gating on ^{12}C fragments with energies lower than 360 MeV.

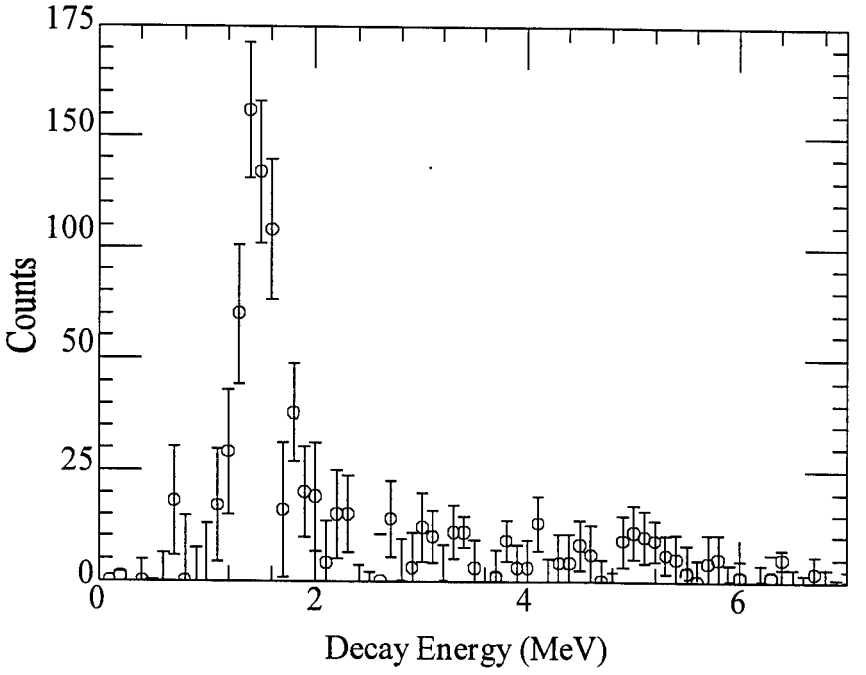

Figure 5.4: Background subtracted spectrum of the decay energy of ^{13}N. The error bars represent the statistical uncertainties only.

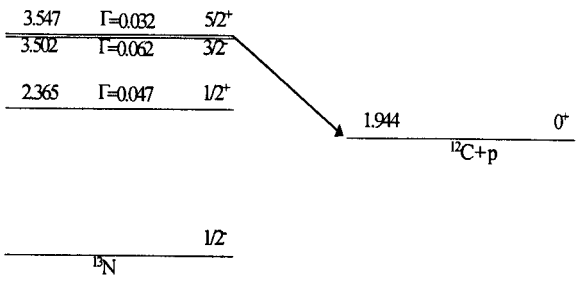

Figure 5.5: Level diagram of ^{13}N [Ajz91]. The excited state proton decay to ^{12}C is indicated by the arrow. All energies are in units of MeV.

Monte Carlo simulations were performed for the 3/2$^-$ state. By fitting the proton energy spectrum an adequate fit was obtained using an energy resolution of 5% FWHM for the MFA in the simulations. The fragment energy resolution was obtained by fitting the data using the tabulated values of the 3/2$^-$ state [Ajz91] and varying the fragment energy resolution to obtain the best fit. These simulations revealed an average energy resolution of 3% for the fragment detectors, measured at FWHM.

By varying the excitation energy and width for the 3/2$^-$ state of ^{13}N in the simulations, the χ^2 surface plot shown in Figure 5.6 was obtained. The minimum χ^2 of 0.8 is indicated by the dashed lines at $E^* = 3.45$ MeV and $\Gamma = 90$ keV and a scale of 0.1 is used for the χ^2 lines. The shaded area corresponds to the space within the $\chi^2_{min} + 1.0$ boundary line. At this boundary the maximum and minimum values of the excitation energy and width were obtained resulting in an excitation energy of $3.45^{+0.05}_{-0.10}$ MeV and a width of 90^{+390}_{-90} keV which are in good agreement with the known values of 3.50 MeV and 62 keV respectively [Ajz91]. The fit of the data using the excitation energy and width obtained above is shown in Figure 5.7.

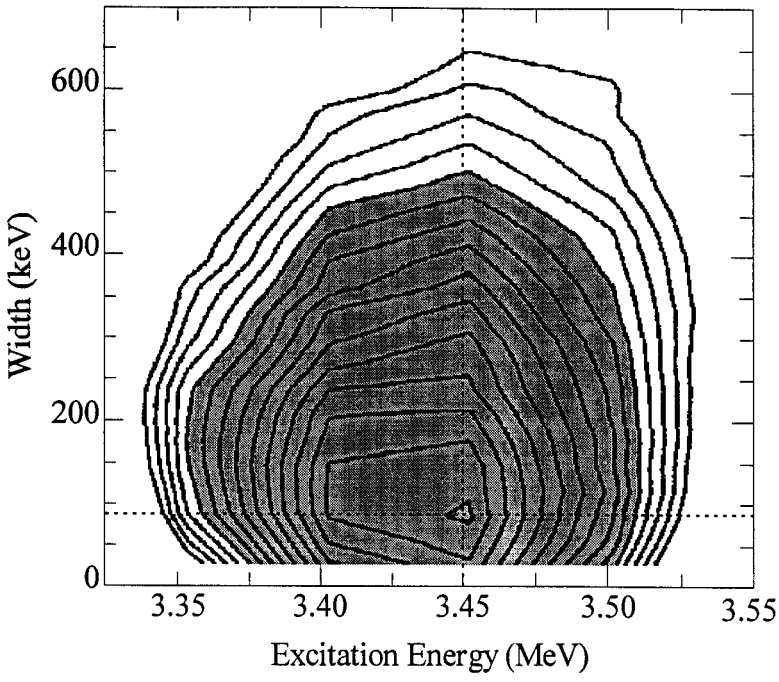

Figure 5.6: χ^2 surface plot as a function of excitation energy and width of the simulated $3/2^-$ excited state of ^{13}N. The dashed lines intersect at the minimum χ^2 and the shaded area shows the region within $\chi^2_{min}+1$.

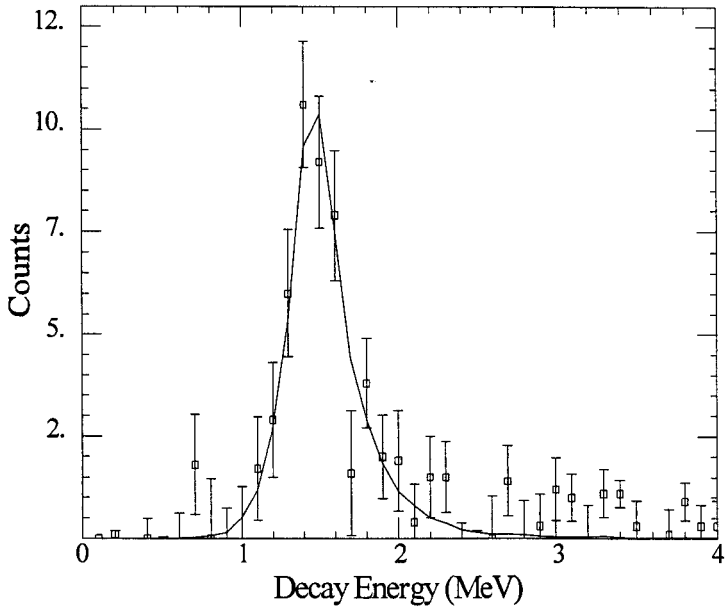

Figure 5.7: Background subtracted decay energy spectrum of ^{13}N fitted by a Monte Carlo simulation of a state at an excitation energy of 3.45 MeV and a width of 90 keV (solid line).

5.1.2 Decay of ^{13}O

The decay energy spectrum of ^{13}O was obtained by requiring a coincidence between protons and ^{12}N. However, the secondary beam used in the experiment was ^{12}N, therefore a distinction had to be made between the actual decay fragments and random coincidences with the beam. When gated on ^{12}N, the fragment energy spectrum shown in Figure 5.8 contained two distinct peaks. The prominent peak at higher energies is due to the beam whereas the smaller peak at lower energies is due to decays from ^{13}O. Also, events within the lower energy peak contained no random coincidences. Therefore, the decay energy spectrum was constructed from events within the low energy peak only.

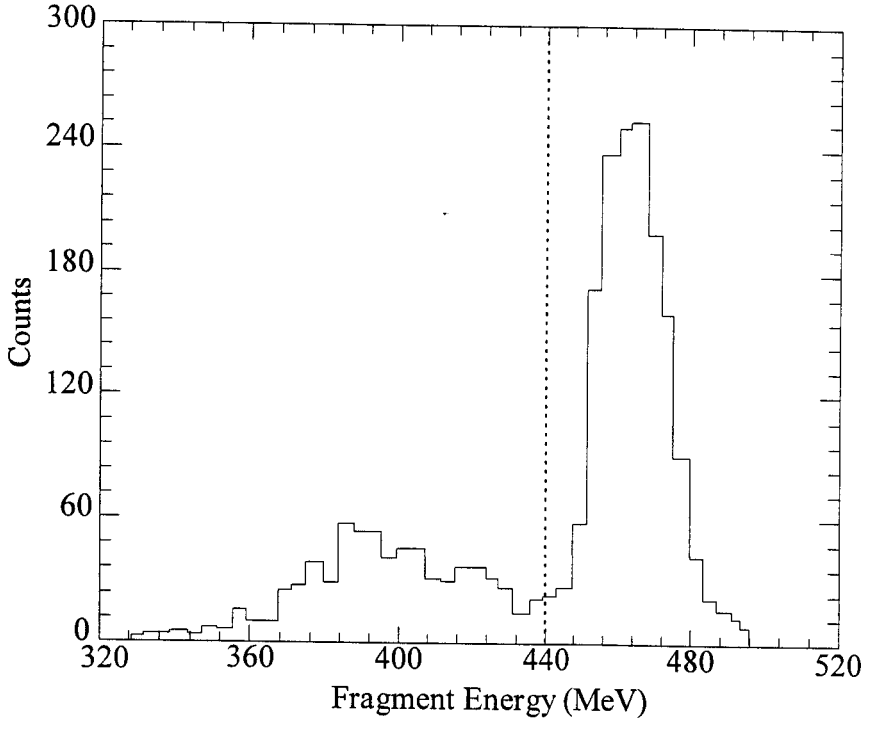

Figure 5.8: Raw energy spectrum of ^{12}N fragments.

A search for the background was performed using the same methods that were applied to ^{13}N. However, no background events were present. Figure 5.9 shows the decay energy spectrum for ^{13}O including statistical error bars. Three peaks are apparent at decay energies of about 1.2, 2.8 and 4.5 MeV. Figure 5.10 shows the level diagram of ^{13}O [Ajz91]. The decay of the first three excited states of ^{13}O to the ground state of ^{12}N exhibit energies close to the center of the peaks in Figure 5.9.

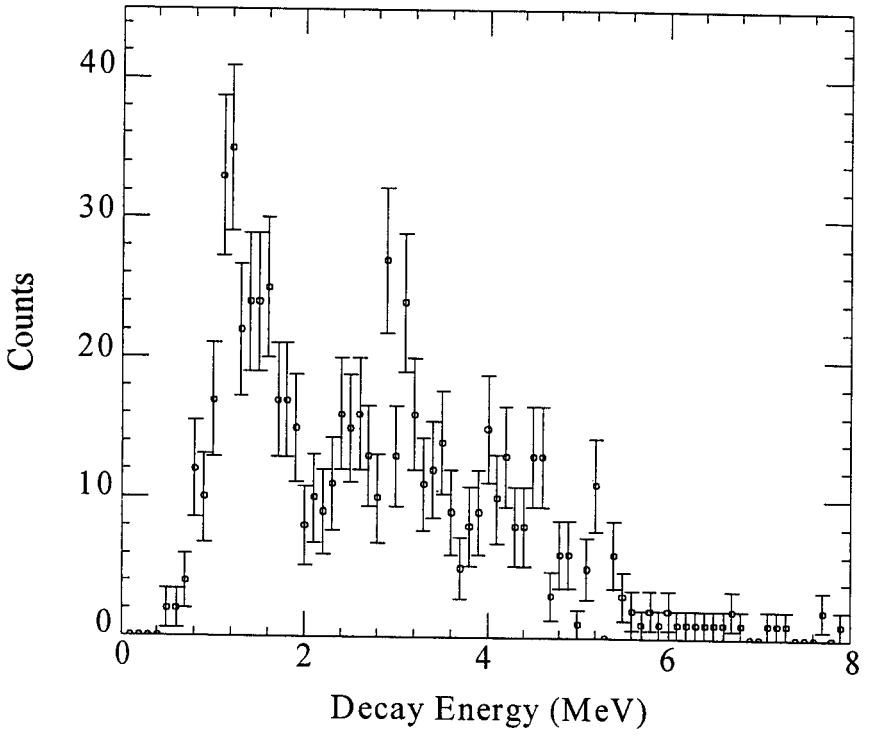

Figure 5.9: Decay energy spectrum for ^{13}O. The data is shown as points with statistical error bars.

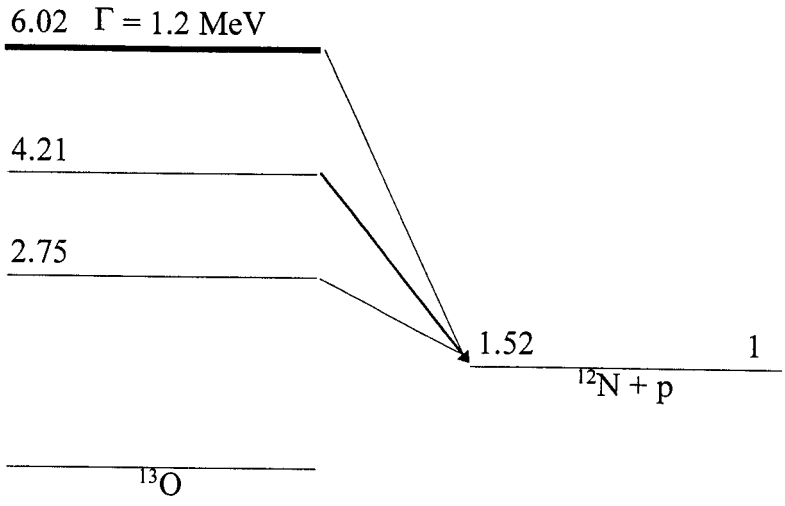

Figure 5.10: Energy levels and decay scheme for ^{13}O. The widths of the first two excited states of ^{13}O were not known. All energies are in units of MeV.

The excited states of ^{12}N are proton unbound, therefore proton decays of ^{13}O to excited states of ^{12}N would not be observed. Monte Carlo simulations of the decay scheme shown in Figure 5.10 were performed. Although χ^2 minimizations for the excitation energies and widths of the states in ^{13}O were not performed, a satisfactory fit of the data using the parameters in Table 5.1 was obtained and is shown in Figure 5.11. The values in Table 5.1 are in good agreement with the tabulated values [Ajz91] and further strengthen the feasibility of the applied methods.

The normalization constants used to fit the decay energy spectrum were used to calculate the relative population ratios of the states in ^{13}O following the reaction ^{9}Be(^{12}N,^{13}O) and are also listed in Table 5.1.

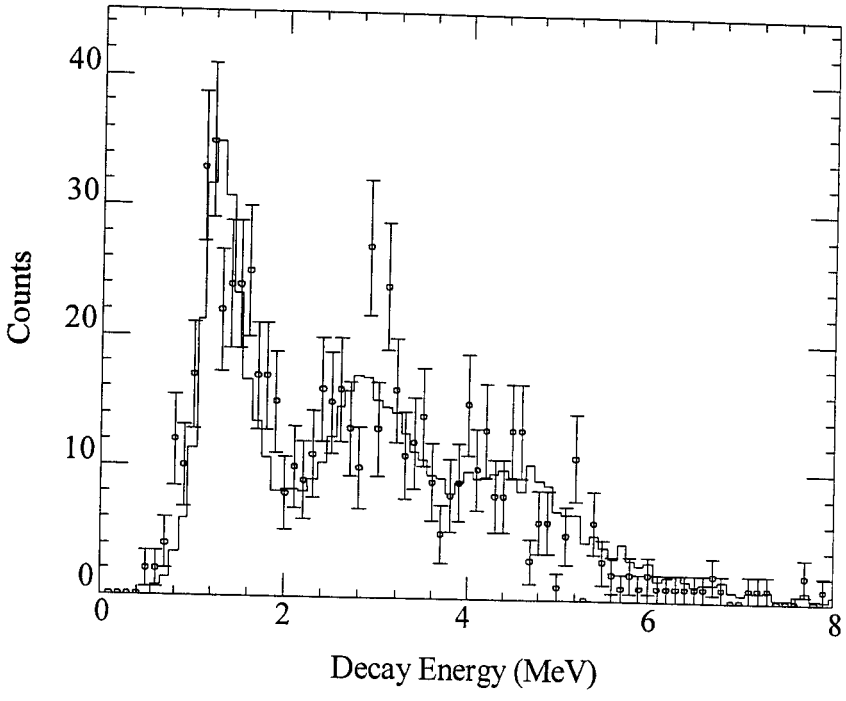

Figure 5.11: Fit of the decay energy spectrum of ^{13}O. The points with the error bars are the data, the solid line was obtained from the sum of the simulations for the first three excited states.

Table 5.1: Excitation energies and widths used to simulate the ^{13}O decay energy spectrum. Also included are the relative population ratios calculated from the simulations.

State (MeV)	Width (keV)	Population (%)
2.85	400	58.3
4.41	500	26.7
6.0	1200	15.0

5.1.3 Decay of ^{10}B

The decay energy spectrum of ^{10}B was constructed by requiring a coincidence between protons and ^{9}Be fragments. Similar to the ^{13}O treatment, background events

were not present. The level structure of ^{10}B above the proton decay threshold is more complex than in the previous two cases. This structure is shown in Figure 5.12 [Ajz88]. Therefore, only the first nine states above the proton threshold were considered.

Figure 5.13 shows the decay energy spectrum calculated for ^{10}B. Due to the inherent 400 keV resolution of the experiment, the states in ^{10}B could not be separated. However, the position of each state is identified in Figure 5.13 by the solid lines.

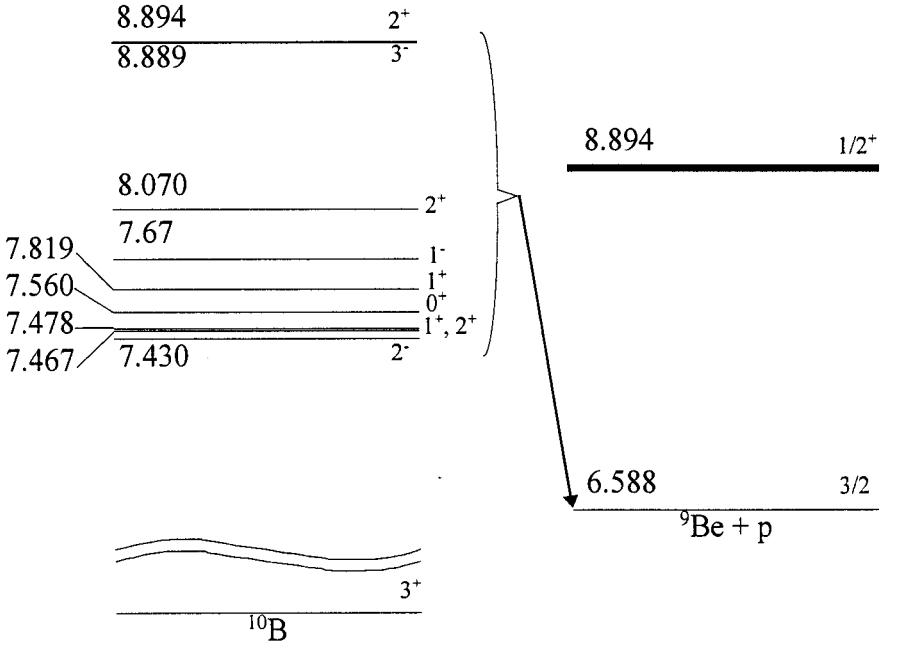

Figure 5.12: Level structure of ^{10}B. All energies are in units of MeV.

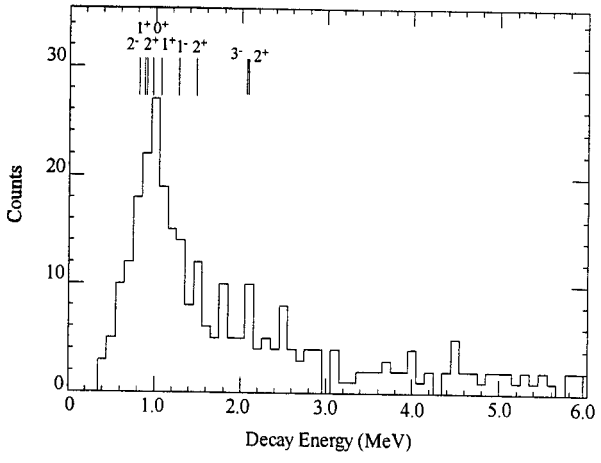

Figure 5.13: Decay energy spectrum for ^{10}B. Contributing states are indicated by the lines.

5.1.4 Decay of ^{11}N

The decay energy spectrum for ^{11}N was obtained by observing coincidences between protons and ^{10}C fragments. Figure 5.14 shows the raw spectrum without background subtraction.

Simulations of the decay of ^{11}N indicated that the ^{10}C fragments must have total kinetic energies above 360 MeV. Similar to the case of ^{13}O, the ^{10}C energy spectrum showed the presence of a tail extending below the 360 MeV limit. Therefore, the background decay energy spectrum for ^{11}N was obtained by gating on ^{10}C fragments energies below 360 MeV. This background spectrum is shown in Figure 5.15 (solid). Superimposed on the data is the simulated efficiency curve for the setup. This curve was obtained by simulating a flat decay energy distribution and describes the experimental background very well, justifying the methods used to obtain the experimental background.

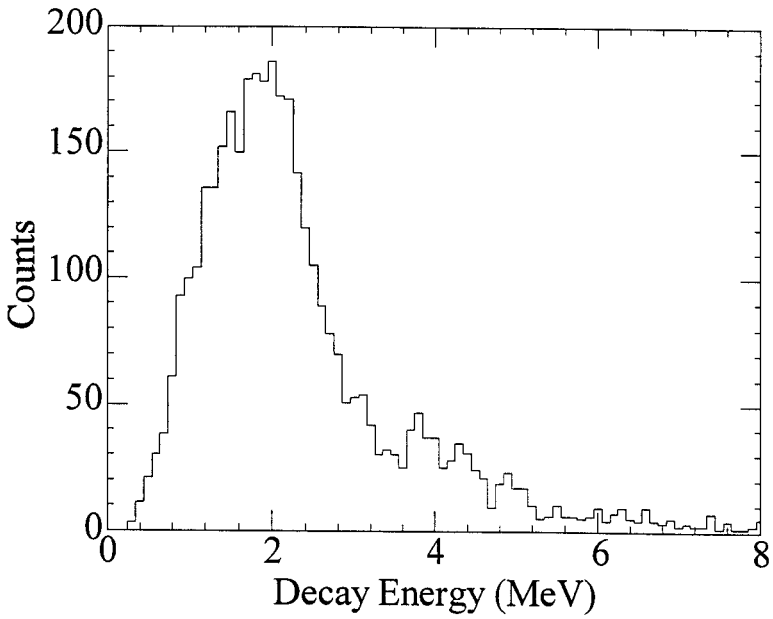

Figure 5.14: Raw decay energy spectrum for ^{11}N.

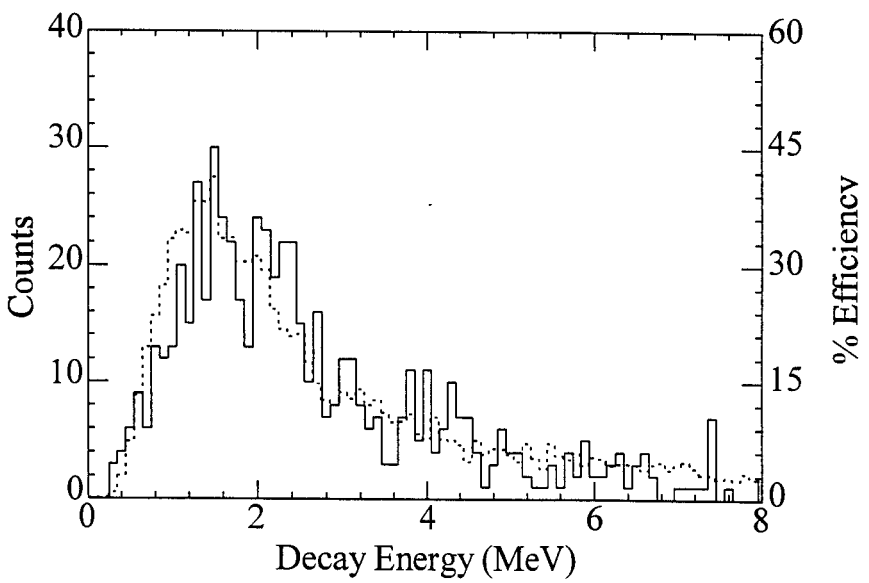

Figure 5.15: Background spectrum for the decay of ^{11}N. The background was obtained by gating on ^{10}C fragments with energies below 360 MeV (solid). The dashed line indicates a simulation of the efficiency of the setup.

The background was normalized within the 5.0 to 8.0 MeV region of the decay energy spectrum and subtracted resulting in the decay energy spectrum of Figure 5.16. Also shown in Figure 5.16 is a simulation of the $1/2^-$ excited state of ^{11}N with the parameters E_{decay} = 2.24 MeV and Γ = 740 keV (dashed line). Although this state is populated, it can not explain the entire peak observed in the data. The enhancement at lower decay energy could be evidence for the ground state of ^{11}N, therefore simulations for a $1/2^+$ ground state were performed.

By varying the decay energy from 0.1 MeV to 6.0 MeV and the width from 0.1 MeV to 4.5 MeV for the $1/2^+$ state by 50 keV steps within the simulations, a grid was obtained. A similar grid was also obtained for the $1/2^-$ excited state, except the variations in decay energy and width were kept within the known uncertainties of these parameters [Ben74]. Fits to the data were performed using every combination of these grid points resulting in a χ^2 value for each fit. A search for the minimum χ^2 was performed using the normalization method described in Section 4.8. The fit using E_{decay} = 1.45 MeV, Γ = 2.4 MeV for the $1/2^+$ state, and E_{decay} = 2.15 MeV, Γ = 750 keV for the $1/2^-$ excited state provided the minimum χ^2 value of 0.838. A fit of the data using the above values is shown in Figure 5.17. The solid line was obtained by summing the normalized simulations for the $1/2^-$ excited state (short dashes) and the $1/2^+$ ground state (long dashes).

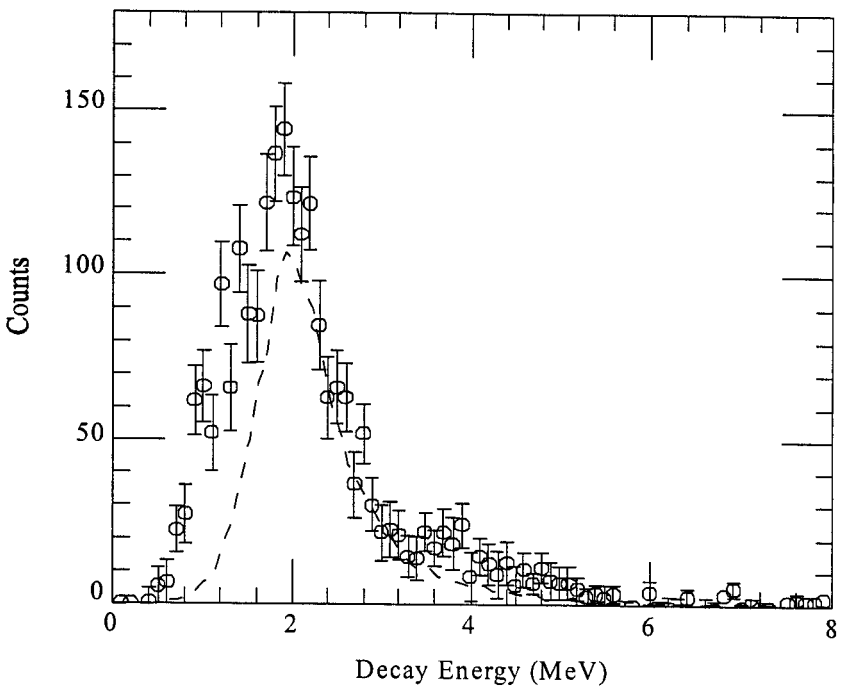

Figure 5.16: Background subtracted decay energy spectrum of ^{11}N.

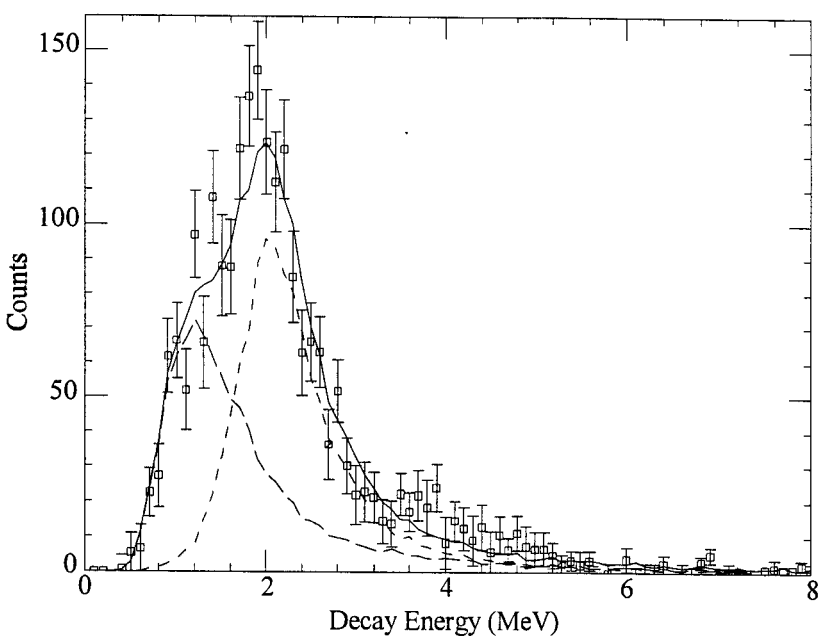

Figure 5.17: Fit of the ^{11}N decay energy spectrum. The fit to the data (solid) is a sum of the contributions from the known $1/2^-$ excited state (short dashes) and a $1/2^+$ state at E_{decay} = 1.45 MeV and Γ = 2.4 MeV (long dashes).

The uncertainties in the decay energy and width of the $1/2^+$ state were found by searching the χ^2 space for the energies and widths where the value of the χ^2 deviated from the minimum by 1. This search was performed using the known parameters and uncertainties for the $1/2^-$ state [Ben74]. A plot of the χ^2 surfaces as a function of decay energy and width of the $1/2^+$ state is shown in Figure 5.18. Lines of constant χ^2 values show the boundaries on the energy and width. Particular emphasis has been put on the $\chi^2_{min} + 1.0$ line which can be used to determine the uncertainties in the decay parameters. The position of the minimum χ^2 is represented by the star. For comparison, the values obtained by recent theoretical calculations for the $1/2^+$ ground state are represented by the filled square with error bars [For95] and the filled circle [Bar96]. These values are in good agreement with the data.

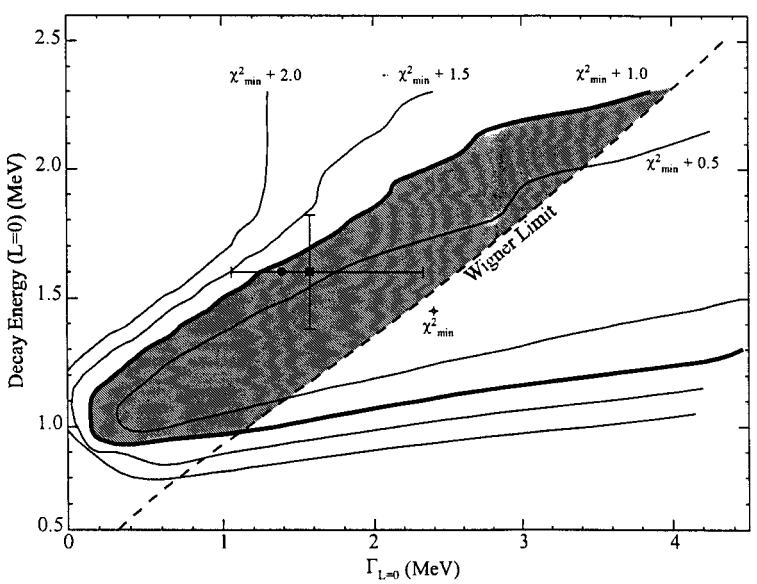

Figure 5.18: χ^2 surfaces as a function of decay energy and width of the $1/2^+$ state. Recent theoretical predictions are indicated by the filled square with the error bars [For95] and the filled circle [Bar96]. The Wigner limit on the decay width is represented by the dashed line. The position of minimum χ^2 is marked by the star.

An upper limit on the width of the $1/2^+$ state could not be obtained experimentally, however the dashed line in Figure 5.18 represents the Wigner limit which provides an upper bound on the width of a state as a function of the decay energy and angular momentum of that state. In order to derive the Wigner limit, we must first introduce the concept of the reduced width. The reduced width γ_L is defined as

$$\gamma_L = \frac{\hbar^2}{2\mu R_n}\left|\chi_L(R_n)\right|^2 \tag{5.1}$$

where the $\chi_L(R)$ is the radial wave function defined by Equation 2.11 where the spectroscopic factor θ_L^2 is the probability of the proton being at the surface of the ^{11}N nucleus and is usually measured experimentally. Since θ_L^2 is a probability, it has an upper limit of 1. This is called the Wigner limit. Incorporating this limit in Equation 5.1 gives

$$\gamma_L\Big|_{max} = \frac{\hbar^2}{\mu R_n^2}. \tag{5.2}$$

Inserting this into Equation 4.14 we obtain an upper limit on the partial width of a state given by

$$\Gamma_L(k,R_n)\Big|_{WL} = \frac{2\hbar^2 k}{\mu R_n} P_L(k,R_n). \tag{5.3}$$

As can be seen in Figure 5.18, the Wigner limit provides an upper limit on the width. The valid space of decay energies and widths is highlighted within the shaded area of Figure 5.18.

The relative intensities for the states included in the fit were used to calculate the relative population of the states in the parent nucleus. Table 5.2 contains the population ratios calculated for the $1/2^+$ and $1/2^-$ states of ^{11}N.

Table 5.2: The relative population ratios of the states in ^{11}N.

State	Population (%)
$1/2^+$	44.7
$1/2^-$	55.3

5.2 Comparisons to Theory

5.2.1 Population Ratios

The production of ^{11}N has been assumed to follow the one neutron stripping reaction $^{9}Be(^{12}N,^{11}N)$, however theoretical calculations for this reaction result in population ratios different from the ones in Table 5.2. Shell model calculations of this transfer reaction result in a population of only 1% for the $1/2^+$ state [Bro96]. Although there is a large discrepancy between the theoretical population and that shown in Table 5.2, the shell model calculations do not include multi-step processes or fragmentation reactions that could contribute to the production of the $1/2^+$ state. Figure 5.19 shows the fragment energy spectrum for the ^{10}C daughter nuclei. Marked in Figure 5.19 are the expected energies of ^{10}C from ^{11}N nuclei formed in transfer reactions (E_t) and fragmentation reactions (E_f). Clearly both mechanisms contribute to the population of the

states in ^{11}N. This mixture of fragmentation and transfer reactions was also observed in an experimental study of ^{16}B [Kry96]. Therefore, the population of the $1/2^+$ state in ^{11}N could be larger than the predicted 1%. Other possibilities for the discrepancy between the experimental and theoretical population ratios for the $1/2^+$ state were considered and will be presented in the following sections.

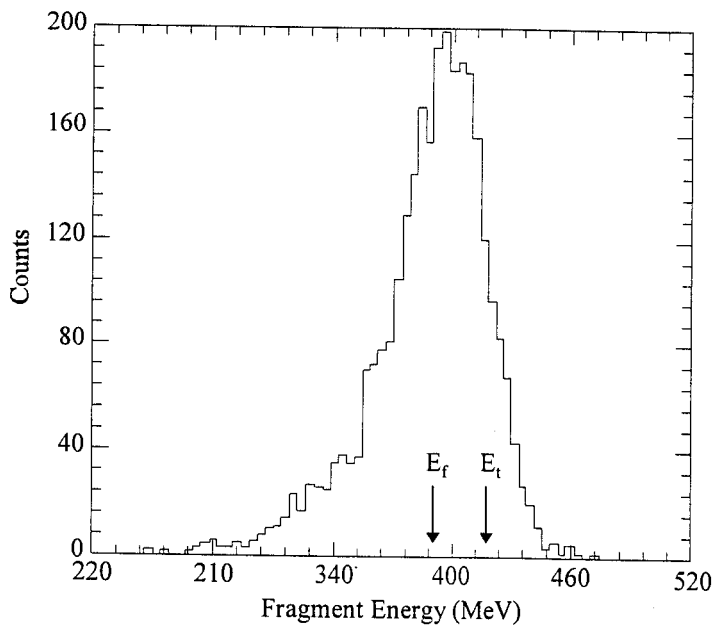

Figure 5.19: ^{10}C energy spectrum. The arrows indicate energies corresponding to formation of ^{11}N via transfer reactions (E_t) and fragmentation reactions (E_f).

5.2.2 Higher Excited States

The construction of the decay energy spectra is sensitive to the relative energy between the parent and daughter states and not the excitation energy of each state alone, therefore decays from other excited states of ^{11}N to the ground and excited states of ^{10}C must also be studied. Although excited states above the $1/2^-$ state in ^{11}N have not been

studied experimentally, theoretical calculations based on the mirror nucleus ^{11}Be have predicted the presence of higher excited states. Aside from the 2.24 MeV state in Figure 1.2, an enhancement is present at about 4.5 MeV decay energy which was interpreted as higher excited states of ^{11}N [Ben74]. An equivalent enhancement can also be seen in the decay energy spectrum of ^{11}N obtained in this study at 4.5 MeV, Figure 5.16. Theoretical calculations predict the existence of $3/2^-$ and $5/2^-$ excited states in ^{11}N at 4.6 MeV and 5.7 MeV, respectively, above the proton decay threshold [Mil96]. The $3/2^-$ state would contain decay branches to both the ground state and the first excited state of ^{10}C as depicted in Figure 5.20. The $5/2^-$ state would decay prominently to the first excited state of ^{10}C since the centrifugal barrier for an $f_{5/2}$ decay is large. Calculations of the partial width of each decay branch of the $3/2^-$ state were performed and $\Gamma(3/2^- \rightarrow 2^+) = 200$ keV and $\Gamma(3/2^- \rightarrow 0^+) = 300$ keV were obtained [Mil96]. These partial widths are denoted in Figure 5.20 as percentages for each decay branch. Table 5.3 contains the calculated energies, partial widths and ratios of the contribution of each excited state of ^{11}N [Mil96].

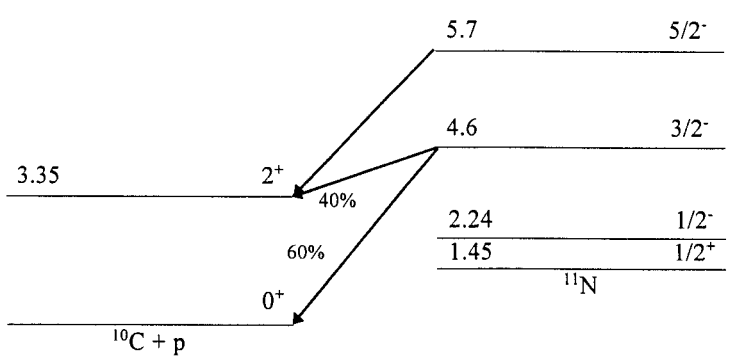

Figure 5.20: Decay scheme for the theoretically predicted [Mil96] $3/2^-$ and $5/2^-$ excited states of ^{11}N. All energies are in units of MeV.

Table 5.3: Parameters for the calculated excited states of ^{11}N [Mil96].

State	Decay Energy (MeV)	Width (keV)	Ratio (%)
$1/2^-$	2.24	790	24.5
$3/2^-$	4.61	300	31.1
$3/2^-$	1.26	200	20.7
$5/2^-$	2.35	640	23.7

The decay of the $3/2^-$ state to the ground state of ^{10}C by 4.6 MeV is a plausible explanation for the enhancement at 4.5 MeV seen in Figure 5.20. However, the decay branch to the first excited state of ^{10}C has a decay energy of 1.25 MeV. This energy is close enough to the 1.45 MeV decay energy, obtained in this study, that they are indistinguishable from each other. This raises the possibility that the enhancement in the decay energy of ^{11}N, which has so far been treated as the $1/2^+$ ground state, could be entirely due to the decay of the $3/2^-$ state.

Up to now the use of Equation 4.13 to calculate the decay line-shape was valid because we have been considering states that have only one decay branch. Therefore, the total width was equal to the partial width of the state. However, the $3/2^-$ state has two decay branches of comparable widths and the total width is now the sum of the two partial widths. Therefore, slight modifications were applied to Equation 4.13 to obtain a line-shape for each decay branch. The new form is given by

$$\sigma_i = N' \frac{\Gamma_i(E, R_n)}{(E - E_r)^2 + \Gamma_T^2(E, R_n)/4} \tag{5.4}$$

where *i* represents the ith decay branch, and the total width of the state is defined by

$$\Gamma_T(E,R_n)=\sum_i \Gamma_i(E,R_n). \tag{5.5}$$

The reduced width was calculated using Equation 4.10 and inserted into Equation 4.14 to obtain the partial width for each decay branch as a function of the decay energy.

Figure 5.21 shows the result of the simulations for the states listed in Table 5.3. The solid line is the sum of the four components (dashed) marked in the figure, and was normalized to the data within the 2.5 to 6.0 MeV decay energy range.

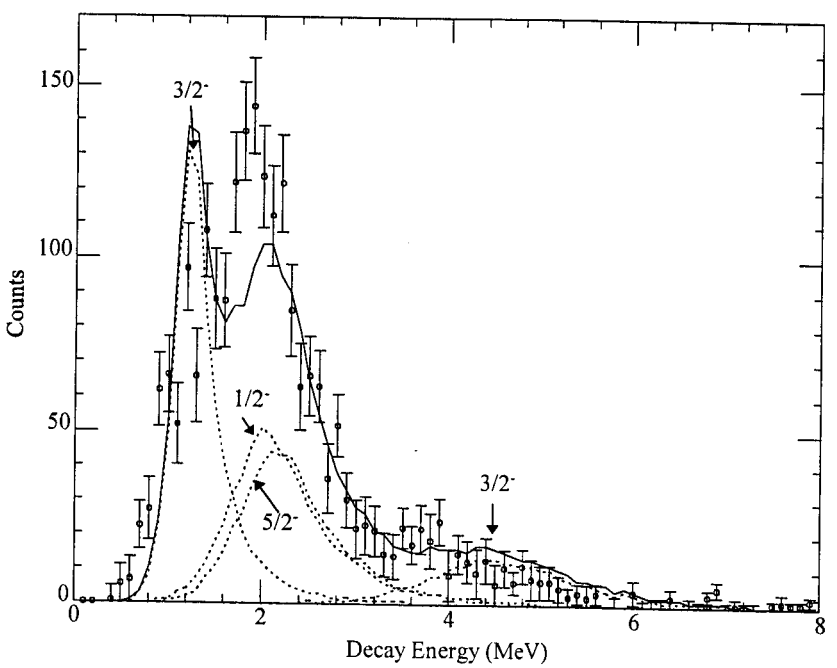

Figure 5.21: Simulation of the decay of the excited states of ^{11}N to the ground and first excited states of ^{10}C.

An overabundance of the 1.26 MeV decay of the 3/2$^-$ state is apparent in Figure 5.21. Although a reasonable fit to the data could possibly be obtained by varying the parameters given in Table 5.3, without the inclusion of a 1/2$^+$ ground state, one can not

rule out the possibility of contribution from a $1/2^+$ state by using arbitrary parameters for the excited states. Since the population ratio of the ground state is strongly dependent on the parameters describing the excited states of ^{11}N, a concrete ratio for the $1/2^+$ state can not be obtained without accurate information on these excited states.

Chapter 6

Summary and Conclusions

In this experiment radioactive nuclear beams were successfully applied to the study of light nuclei beyond the proton dripline, in particular ^{11}N. These nuclei were formed via transfer reactions and decayed immediately by emitting a proton. By observing the proton and the daughter nucleus in coincidence, a complete kinematic reconstruction of the parent nucleus was performed to obtain the decay energy.

A Monte Carlo simulation program incorporated all aspects of the experiment, especially the decay kinematics and the detector geometry. Testing and calibration of this code was achieved using the decay of well known nuclei which were produced in conjunction with the ^{11}N. Fits to the data were obtained at various decay energies and widths. These fits were used to obtain χ^2 surfaces which in turn provided the optimum values of the decay energy and width along with their uncertainties.

A decay energy spectrum was calculated for ^{13}N. Fits of this spectrum yielded an excitation energy of $3.45^{+0.05}_{-0.10}$ MeV and a width of 90^{+390}_{-90} keV for the $3/2^-$ second excited state of ^{13}N. These values compare well with the tabulated values of 3.50 MeV and 62 keV, respectively [Ajz91].

The decay spectrum for ^{13}O was also obtained and fitted. In this case the first three excited states were observed. Although these states were previously studied, the width of the first two excited states were unknown. The excitation energies of the first three excited states were measured at 2.85 MeV, 4.41 MeV, and 6.0 MeV with widths of 400 keV, 500 keV, and 1.2 MeV respectively. Uncertainties for these values were not calculated since ^{13}O was not the primary nucleus of interest and the obtained decay parameters were in good agreement with the tabulated values [Ajz91]. A comparison of the number of events used within the simulations and the normalization factors used to fit the data allowed for the calculation of the relative population of these states in the reaction forming ^{13}O.

The decay energy spectrum of ^{11}N was reconstructed by observing the protons in coincidence with ^{10}C fragments. The previously known $1/2^-$ first excited state was identified successfully. An enhancement was observed in the lower decay energy region of the spectrum and χ^2 optimizations were performed to fit this region with a $1/2^+$ state. The best fit was obtained for a decay energy of 1.45 MeV and a width of 2.4 MeV. Uncertainties could not be obtained for these values directly, however a valid region within the decay energy and width space was calculated. These parameters are in good agreement with recent theoretical calculations [Bar96,For95].

Relative population ratios were obtained for these states using the normalization factors obtained from the fits to the data. Although shell model calculations predicted a population ratio of only 1% for the ground state of ^{11}N [Bro96], a ratio of 45% was measured from the data. However, the shell model calculations did not include

contributions from fragmentation reactions which contributed to the population of the states of ^{11}N. Simulations were performed to observe the possible contribution of theoretically predicted $3/2^-$ and $5/2^-$ excited states in ^{11}N decaying to the first excited state of ^{10}C. However, the contribution from these states over-predicted the data in the low decay energy region. Therefore, a population ratio could not be obtained for the $1/2^+$ state in the presence of the excited states.

The lower decay energy of the ground state of ^{11}N, compared to the previously predicted value of 1.9 MeV, could explain the low branching ratio observed for diproton decay of ^{12}O. A ^{11}N state at 1.45 MeV would provide the intermediate state needed for the sequential proton decay of ^{12}O within the constraints of the observed width of the ground state of ^{12}O. Also, further analysis of the ^{12}O data could provide further limits on the decay parameters of the ground state of ^{11}N.

APPENDIX

Appendix A

Monte Carlo Simulation

A.1 Description

The Monte Carlo simulation code was written in Fortran, except for the random number generator which was written in C. All routines were adapted to run in double precision mode. The program, along with all subroutines and functions have been commented, therefore only brief descriptions will be provided.

PRO_DECAY: This is the main body of the program. All inputs, kinematic calculations, and outputs are handled by this unit.

GASDEV: This function generates Gaussian [Pre92], Lorentzian, and flat distribution of random numbers between -0.5 and 0.5.

UNIRAN: In conjunction with ERAND48, these functions provide random numbers between 0 and 1 based on two seeds.

THERMAL: Generates a thermal distribution according to

$$\frac{2}{T}\sqrt{\frac{E}{\pi T}}\exp(-E/T)$$

where E is the energy and T is the temperature.

DAUGHTER1: Allows the simulation of a square grid detector system for the fragments.

DAUGHTER3: Contains the geometric information for the fragment telescope in the ^{11}N experiment.

PROTON1: Allows the simulation of a square grid detector system for the protons.

PROTON2: Contains the geometric information for the MFA.

DAFTAN: A function to calculate the arc-tangent from the division of two numbers.

BINSEARCH: Uses a binary search pattern to find the array element containing the desired data.

LINESHAPE: Calculates the line-shape of the decay based on the width of the state. This routine incorporates Coulomb and Centrifugal barriers in the line-shape. There are two versions of this code listed. One is for use with states that have only one proton decay branch, the second simulates a state with two proton decay branches.

PENETRATE: This subroutine calculates the penetrability at a given energy and nuclear radius. This subroutine calls on another subroutine, COULL, which calculates the Coulomb functions. The body of the code for COULL is not included here.

ERAND48: This code is written in C and uses two seeds to generate two random numbers.

A.2 Input File

A sample input file is included at the end of the code with a brief description of each input parameter, however a more expanded description follows.

Line 1a: First seed needed for random number generation.
Line 1b: Second seed needed for random number generation.

Line 2: Number of decays to simulate.

Line 3a: Output mode. A value of zero creates a decay energy spectrum only, whereas a value of 1 creates an event file containing a description of every event. This event file will be described fully later.

Line 3b: Factor used to define the width of the binning in the decay energy spectrum.

Line 4: Selects either a fragmentation reaction or a transfer reaction to populate the parent nucleus.

Line 5a: Selects the distribution used to describe the decay. Available distributions are Lorentzian, penetrability, thermal, and flat.
Line 5b: Sets the angular momentum when using the penetrability distribution.
Line 5c: Sets the temperature for the thermal distribution, or the width of the flat distribution (MeV).

Line 6a: Switch to turn the target excitation on or off.
Line 6b: Sets the temperature for the thermal distribution used to obtain the target excitation (MeV)

Line 7a: Switch to turn on the singles mode where the scattering angle and decay angle of the proton can be fixed.
Line 7b: Scattering angle in radians (CoM).
Line 7c: Decay angle of the proton in radians (CoM).

Line 8a: Atomic number of the beam.
Line 8b: Proton number of the beam.
Line 8c: Mass of the beam including any excitation (MeV).

Line 9a: Beam energy (MeV/nucleon).
Line 9b: % spread in the momentum of the beam (FWHM).

Line 10a: FWHM of the beam in the x-projection of PPAC2 (mm).
Line 10b: FWHM of the beam in the y-projection of PPAC2(mm).

Line 11a: Beam offset in the x direction on PPAC2 (mm).
Line 11b: Beam offset in the y direction on PPAC2 (mm).

Line 12a: FWHM of the beam in the x-projection of PPAC2 (mm).
Line 12b: FWHM of the beam in the y-projection of PPAC2(mm).

Line 13a: Beam offset in the x direction on PPAC1 (mm).
Line 13b: Beam offset in the y direction on PPAC1 (mm).

Line 14a: Atomic number of the unstable nucleus.
Line 14b: Proton number of the unstable nucleus.
Line 14c: Mass of the unstable nucleus including any excitation (MeV).

Line 15: Width of the decaying state (MeV).

Line 16a: Atomic number of the daughter nucleus.
Line 16b: Proton number of the daughter nucleus.
Line 16c: Mass of the daughter nucleus including any excitation (MeV).

Line 17a: Atomic number of the target nucleus.
Line 17b: Proton number of the target nucleus.
Line 17c: Mass of the target nucleus including any excitation (MeV).

Line 18a: Atomic number of the residue nucleus.
Line 18b: Proton number of the residue nucleus.
Line 18c: Mass of the residue nucleus including any excitations (MeV).

Line 19a: Target thickness (mm)
Line 19a: Target thickness (mg/cm^2)

Line 20: Average energy loss of the beam per mm in the target (when not using the energy loss equations).

Line 21: Average energy loss of the daughter nucleus per mm in the target (when not using the energy loss equations).

Line 22: Average energy loss of the protons per mm in the target (when not using the energy loss equations).

Line 23a: Distance of the proton detector from the target (mm).
Line 23b: Distance of the fragment detector from the target (mm).

Line 24a: % energy resolution of the proton detectors (FWHM).
Line 24b: % energy resolution of the fragment detectors (FWHM).

Line 25a: Grid size for the proton detectors (mm) (only when using subroutine PROTON1).
Line 25b: Grid size for the fragment detectors (mm) (only when using subroutine DAUGHTER1).

Line 26a: θ_c used in calculating the scattering angle in the CoM (rad.)
Line 26b: Slope of the distribution used to calculate the scattering angle ($deg.^{-1}$)

Line 27: Switch to turn energy loss equations on or off.

Line 28a: Lower limit on the beam energy where the energy loss equations are no longer valid (MeV)
Line 28b: Upper limit on the beam energy where the energy loss equations are no longer valid (MeV).

Line 29: Constant term in the quadratic used to fit the energy loss of the beam in the target.

Line 30: Coefficient of the linear term in the quadratic used to fit the energy loss of the beam in the target.

Line 31: Coefficient of the squared term in the quadratic used to fit the energy loss of the beam in the target.

Line 32a: Lower limit on the daughter energy where the energy loss equations are no longer valid (MeV)

Line 32b: Upper limit on the daughter energy where the energy loss equations are no longer valid (MeV).

Line 33: Constant term in the fourth order equation used to fit the energy loss of the daughter in the target.

Line 34: Coefficient of the linear term in the fourth order equation used to fit the energy loss of the daughter in the target.

Line 35: Coefficient of the squared term in the fourth order equation used to fit the energy loss of the daughter in the target.

Line 36: Coefficient of the cubic term in the fourth order equation used to fit the energy loss of the daughter in the target.

Line 37a: Lower limit of the first region of fit for the proton energy loss equations (MeV).

Line 37b: Lower limit of the second region of fit for the proton energy loss equations (MeV).

Line 37c: Lower limit of the third region of fit for the proton energy loss equations (MeV).

Line 37d: Upper limit of the third region of fit for the proton energy loss equations (MeV).

Line 38a: Constant coefficient for the first region of the proton energy loss equation.

Line 38b: First order coefficient for the first region of the proton energy loss equation.

Line 39a: Second order coefficient for the first region of proton energy loss equation.

Line 39b: Third order coefficient for the first region of proton energy loss equation.

Line 40a: Constant coefficient for the second region of proton energy loss equation.

Line 40b: First order coefficient for the second region of proton energy loss equation.

Line 41a: Second order coefficient for the second region of proton energy loss equation.

Line 41b: Third order coefficient for the second region of proton energy loss equation.

Line 42a: Constant coefficient for the third region of the proton energy equation.

Line 42b: First order coefficient for the third region of the proton energy equation.

Line 43a: Second order coefficient for the third region of the proton energy equation.

Line 43b: Third order coefficient for the third region of the proton energy equation.

Line 44: Same as Line 1a. Used for cross checking the input procedure.

A.3 Output

Depending on the output mode selected in Line 3a of the input file one of two forms of output is generated. If Line 3a contains a zero, a decay energy file is created which contains the decay energy in the first column and the number of counts per channel in the second column. However, if Line 3a is set to one then a binary event file is created. The pattern used to store the information is:

Integer *4	Ievent(4)
Real *8	Revent(40), event(44)
Equivalence	(event(1), Ievent(1)), (event(5), Revent(1))

where the arrays 'Ievent' and 'Revent' contain the parameters created by the simulation. Table A.1 gives the description of the variables in the array 'Revent' and Table A.2 gives similar descriptions for the array 'Ievent'.

Table A.1: Variables in the array 'Revent'.

Revent(#)	Variable Description
1	Fragment mass + width (MeV)
2	x on PPAC1 (mm)
3	y on PPAC1 (mm)
4	x on PPAC2 (mm)
5	y on PPAC2 (mm)
6	Beam radius on PPAC2 (mm)
7	Theta of beam in laboratory (deg)
8	Phi of beam in laboratory (deg)
9	Theta of beam with respect to the average beam angle
10	Phi of beam with respect to the average beam phi
11	Target Penetration (mm)
12	Beam energy at scattering (MeV)
13	Theta scattering in CoM (rad)
14	Velocity of fragment in CoM (v/c)
15	Velocity of fragment in beam coordinates (v/c)
16	Theta of scattering relative to beam (rad)
17	Velocity of fragment in the laboratory frame (v/c)
18	Theta of fragment in the laboratory frame (rad)
19	Velocity of proton in CoM (v/c)
20	Theta of proton in CoM (rad)
21	Velocity of daughter in CoM (v/c)
22	Theta of daughter in CoM (rad)
23	Velocity of proton in laboratory frame (v/c)
24	Theta of proton in laboratory frame (rad)
25	Velocity of daughter in laboratory frame (v/c)
26	Theta of daughter in laboratory frame (rad)
27	Proton energy loss in target (MeV)
28	Daughter energy loss in target (MeV)
29	Kinetic energy of proton including experimental resolutions (MeV)
30	Kinetic energy of daughter including experimental resolutions (MeV)
31	x position of proton in detector not including position resolution (mm)
32	y position of proton in detector not including position resolution (mm)
33	x position of daughter in detector not including position resolution
34	y position of daughter in detector not including position resolution

Table A.1 (cont'd)

Revent(#)	Variable Description
35	x position of proton in detector including position resolution (mm)
36	y position of proton in detector including position resolution (mm)
37	x position of daughter in detector including position resolution (mm)
38	y position of daughter in detector including position resolution (mm)
39	Laboratory opening angle between proton and daughter (rad)
40	Experimental decay energy (keV)

Table A.2: Description of variable in the array 'Ievent'.

Ievent(#)	Description
1	Event number
2	Non-zero if event was dropped
3	Iseed(1)
4	Iseed(2)

If Ievent(2) is not zero that indicates that a 'bad' event occurred. The values of Ievent(2) and the cause of the 'bad' event are given in Table A.3.

Table A.3: Values of Ievent(2) and description of the cause of the 'bad' event.

Value of Ievent(2)	Description
1	Negative decay energy
2	Transfer reaction did not occur
3	Proton stopped in target
4	Daughter Stopped in Target
5	Proton missed detector
6	Daughter missed detector

A.4 Pro_Decay

```
      PROGRAM PRO_DECAY

c     this program was written to simulate the proton decay of nuclei
c     beyond the proton drip line and all the observed effects within
c     the experiment.
c
c                        by
c
c                              Afshin Azhari
c                              1994-1996

      real*4 fac
      integer*4 iaf(7),eloss_mode,ievent(4),therm,singles,
      integer*4 i,k,d,hexact(0:1000),hexp(0:1000),flag,icount
      integer*4 a_beam,z_beam,a_frag,z_frag,a_dau,z_dau
      integer*4 a_tar,z_tar,a_prod,z_prod,iii,iseed(2),eventn
      integer*4 j,out,itemp1,itemp2,itemp3,itemp4,itemp5
      integer*4 itemp6,itemp7,reaction,prod_term,check,l_mom
      real*8 Uniran,erand48,gasdev,ep_res,ed_res,res_p,res_d
      real*8 e_p_res,a1,a2,vfrag_z,m_beam,e_beam1,rad_1,rad_2
      real*8 l,temp_r,detz_p,detz_d,x_p,y_p,x_d,y_d,relvel
      real*8 e_beam,dp_beam,p_beam,de_beam,e_d_res,rbin
      real*8 p_beam1,x1_beam,y1_beam,z1_beam,gamma_d,m_frag
      real*8 e_frag,v_frag,phi_d,e_d,pen_tar,b_eloss,e_p,v_p1
      real*8 v_frag1,ke_d,loss_d,m_frag1,x_p_res,m_dau,theta_d1
      real*8 v_d1,theta_d,v_d,theta2,phi2,p_2,m_tar,tar_thick
      real*8 d_eloss,p_eloss,m_prod,mar_thd,m_prot,theta_p1,phi_p
      real*8 theta_p,v_p,gamma_p,ke_p,mar_rd,loss_p,pi,w_decay
      real*8 theta1,l1,l2,vp_x,vp_y,vp_z,vd_x,vd_y,vd_z,vfrag_x
      real*8 phi1,w_2,q,gamma,beta,vfrag_y,vp_x1,vp_y1,vp_z1
      real*8 norm,cons,a_c,x_d_res,mar_rp,vd_x1,vd_y1,vd_z1
      real*8 y_d_res,grid_p,grid_d,vp_res,vd_res,revent(40),r_emit
      real*8 temp1,temp2,temp3,temp4,event(44),x1res_beam
      real*8 y1res_beam,max_rad,th_emit,vfragy,vfragz,e
      real*8 b,c,mf_exact,mf_exp,cos_exact,cos_exp
      real*8 ep_exact,ed_exact,ep_exp,ed_exp,phi_emit,vfragx
      real*8 theta_c,slope,y_p_res,mar_thp,fwhm,a,sing1,sing2
      real*8 offset(2),v1p(3),v1d(3),v2p(3),v2d(3),temp,xoff
      real*8 e_therm(0:20000),daftan,rad_beam1,rad_beam2,yoff
      real*8 xoff2,yoff2,rtemp(7),mgcmsq,v_beam,prod_temp
      real*8 bemin,bemax,beloss(0:2),prod_th(0:20000),x2_beam
      real*8 demin,demax,deloss(0:3),m_prod1,y2_beam
      real*8 plimit(4),peloss(3,0:3),z2_beam
      real*8 x2res_beam,y2res_beam,rad_beam3,rad_beam4
      real*8 prob(0:1000),energy(0:1001)
      equivalence (event(1),ievent(1)),(event(5),revent(1))
      common /daughter/ x_d,y_d,x_d_res,y_d_res,grid_d,pi
      common /proton/ x_p,y_p,x_p_res,y_p_res,grid_p
      common /all/ ievent,flag
      common /seeds/ iseed
```

```
      common /penetr1/ m_frag,a_dau,z_dau,m_dau,m_prot,l_mom
      common /penetr2/ w_decay,prob,energy

      pi = dacos(-1.d0)
      fwhm = 2.d0 * dsqrt(2.d0 * dlog(2.d0))
      v1p(1)=0.d0
      v1p(2)=0.d0
      v1p(3)=0.d0

      read(5,*) iseed(1),iseed(2)
      read(5,*) eventn

c     read output mode (out=1 eventfile, out=0 masses only)
      read(5,*) out,fac

c     read type of reaction in target (transfer or fragmentation)
      read(5,*) reaction

c     read type of lineshape to use for decay
      read(5,*) therm,l_mom,temp

c     read in the thermal info for target product
      read(5,*) prod_term,prod_temp

c     read in the singles info
      read(5,*) singles,sing1,sing2

c     read in beam parameters
      read(5,*) a_beam,z_beam,m_beam
      read(5,*) e_beam,dp_beam
      read(5,*) rad_beam1,rad_beam2
      read(5,*) xoff,yoff
      read(5,*) rad_beam3,rad_beam4
      read(5,*) xoff2,yoff2

c     read in fragment parameters
      read(5,*) a_frag,z_frag,m_frag
      read(5,*) w_decay
      if ((therm.eq.1).and.(w_decay.le.1.d-2)) therm = 0

c     read in daughter parameters
      read(5,*) a_dau,z_dau,m_dau

c     some data about protons
      m_prot = 938.27231d0

c     read in target parameters
      read(5,*) a_tar,z_tar,m_tar
      read(5,*) a_prod,z_prod,m_prod
      read(5,*) tar_thick,mgcmsq
      read(5,*) b_eloss
      read(5,*) d_eloss
      read(5,*) p_eloss
```

```
c       read detector parameters
        read(5,*) detz_p,detz_d
        read(5,*) res_p,res_d
        read(5,*) grid_p,grid_d

c       read the scattering parameters
        read(5,*) theta_c,slope

c       read energy loss parameters
        read(5,*) eloss_mode
        read(5,*) bemin,bemax
        read(5,*) beloss(0)
        read(5,*) beloss(1)
        read(5,*) beloss(2)
        read(5,*) demin,demax
        read(5,*) deloss(0)
        read(5,*) deloss(1)
        read(5,*) deloss(2)
        read(5,*) deloss(3)
        read(5,*) plimit(1), plimit(2), plimit(3), plimit(4)
        read(5,*) peloss(1,0),peloss(1,1)
        read(5,*) peloss(1,2),peloss(1,3)
        read(5,*) peloss(2,0),peloss(2,1)
        read(5,*) peloss(2,2),peloss(2,3)
        read(5,*) peloss(3,0),peloss(3,1)
        read(5,*) peloss(3,2),peloss(3,3)
        read(5,*) check

        if (check.ne.iseed(1)) then
          write(*,*) '-----------------------------------------'
          write(*,*) 'Warning:  Input file does not have the right'
          write(*,*) '        number of parameters'
          write(*,*) '-----------------------------------------'
          write(*,*)
          write(*,*)
          goto 1034
        endif
        write(*,*) 'Input completed successfully .....'

        if (out.eq.1) then
          open(unit=62,file='pro_decay.event',form='unformatted',status='new')
        endif

c1      calculate beam energy and momentum
        e_beam = e_beam * a_beam
        e_beam = e_beam + m_beam
        p_beam = dsqrt(e_beam**2.d0 - m_beam**2.d0)
        dp_beam= dp_beam * p_beam / 100.d0

c       now we can do some calculations to setup for the transfer reaction

c1.4    first calculate the normalization factor
        cons = 1.d0 + slope*theta_c
        norm = slope * dlog(10.d0) * dsin(theta_c) + dcos(theta_c)
```

```
      norm = norm * dexp(-1.d0*slope*theta_c*dlog(10.d0))
      norm = norm + dexp(-1.d0*slope*pi*dlog(10.d0))
      norm = norm * dexp(cons*dlog(10.d0)) / (slope * dlog(10.d0))**2.d0
      norm = norm + 10.d0 * (1.d0 - dcos(theta_c))
      norm = 1.d0 / norm

c1.7  now calculate the critical area and start the picking process
      a_c = 10.d0 * norm * ( 1.d0 - dcos(theta_c))

      write(*,*) 'Calculating Line Shapes ...'

c     now determine the thermal distributions
      if (therm.eq.1) call lineshape(icount)
      temp = temp * 1.d3
      if (therm.eq.2) then
            call thermal(temp,e_therm,0,20000)
            m_frag=m_dau+m_prot
      endif
      prod_temp = prod_temp * 1.d2
      if (prod_term.eq.1) then
            call thermal(prod_temp,prod_th,0,20000)
      endif
      m_prod1 = m_prod

c     now set the line-shapes for the ppacs

      call ppac_xy(3,rtemp(0),rtemp(1))

c     now start the main loop of events
      write(*,*) 'Entering the Monte Carlo loop .....'

      do 10000 iii=1,eventn

      j = int(iii/5000)
      if (j.eq.real(iii)/5.e3) write(*,*) 'Event ',j*5000

      ievent(1) = iii
      ievent(2) = 0
      ievent(3) = iseed(1)
      ievent(4) = iseed(2)

c2    put in the decay width
      if (therm.eq.0) then
            m_frag1 = m_frag + (w_decay * gasdev(iseed,2))
      elseif (therm.eq.1) then
            m_frag1 = uniran(iseed)

            call binsearch(prob,0,1000,m_frag1,i,rbin)

            rbin = (energy(i+1) - energy(i)) * rbin
            m_frag1 = m_dau + m_prot + energy(i) + rbin
      elseif (therm.eq.2) then
            m_frag1 = uniran(iseed)
```

```
            call binsearch(e_therm,0,20000,m_frag1,i,rbin)

            m_frag1 = m_frag + (float(i)+rbin)/1.d3
      elseif (therm.eq.3) then
            m_frag = m_dau + m_prot
            m_frag1 = m_frag + (temp/1.d3 * uniran(iseed))
      endif

      if(m_frag1.lt.m_prot+m_dau) then
            ievent(2) = 1
            goto 9999
      endif

c     this section will give the target recoil a thermal excitation
      if (prod_term.eq.1) then
            m_prod = uniran(iseed)

            call binsearch(prod_th,0,20000,m_prod,i,rbin)

            m_prod = m_prod1 + (float(i)+rbin)/1.d2
      endif

      revent(1) = m_frag1

c     now start the tracing:
c3    first calculate the distance penetrated into target
      pen_tar = tar_thick * uniran(iseed)

      revent(11) = pen_tar

c4    now calculate position for the beam
      x1_beam = uniran(iseed)
      y1_beam = uniran(iseed)
      call ppac_xy(2,x1_beam,y1_beam)

      x1_beam = x1_beam + xoff
      y1_beam = y1_beam + yoff
      z1_beam = pen_tar

c4.1  calculate beam position on PPAC1
      x2_beam = uniran(iseed)
      y2_beam = uniran(iseed)
      call ppac_xy(1,x2_beam,y2_beam)

      x2_beam = x2_beam + xoff2
      y2_beam = y2_beam + yoff2
      z2_beam = -1.85d3

c4.5  now fold in the position resolution on target
      x1res_beam = x1_beam
      y1res_beam = y1_beam
      x2res_beam = x2_beam
      y2res_beam = y2_beam
```

```
      revent(2) = x2res_beam
      revent(3) = y2res_beam
      revent(4) = x1res_beam
      revent(5) = y1res_beam

c4.6  now calculate the angles
      x2_beam = x2_beam - x1_beam
      y2_beam = y2_beam - y1_beam
      th_emit = dsqrt(x2_beam**2.d0 + y2_beam**2.d0)
      th_emit = dabs(datan(th_emit/z2_beam))
      phi_emit = pi + daftan(y2_beam,x2_beam)

      revent(9) = th_emit
      revent(10) = phi_emit

c5    now calculate the beam momentum right at the moment of scattering
      p_beam1 = p_beam + dp_beam * gasdev(iseed,3)
      de_beam = b_eloss * pen_tar / dcos(th_emit)
      e_beam1 = dsqrt(p_beam1**2.d0 + m_beam**2.d0)

      if (eloss_mode.eq.1) then
            rtemp(7) = e_beam1 - m_beam
             if (rtemp(7).lt.bemin .or. rtemp(7).gt.bemax) itemp5=itemp5+1
            de_beam = pen_tar / tar_thick * mgcmsq / dcos(th_emit)
            rtemp(7)=rtemp(7)**2.d0*beloss(2)+rtemp(7)*beloss(1)+beloss(0)
            de_beam = rtemp(7) * de_beam
      endif

      e_beam1 = e_beam1 - de_beam
      if (e_beam1.le.m_beam) then
            ievent(2)=7
            goto 9999
      endif
      p_beam1 = dsqrt(e_beam1**2.d0 - m_beam**2.d0)

      revent(12) = e_beam1 - m_beam

c     now the transfer reaction occurs, so find CoM angle of fragment

c6    first we find the area and then theta
      if (singles.eq.1) then
            theta1 = sing1
            goto 66
      endif
      a = uniran(iseed)
      if (a.le.a_c) then
            theta1 = dacos(1.d0 - a / (10.d0*norm))
      else
            l1=theta_c
            l2=pi
10          l=(l1+l2)/2.d0
            a1=slope*dlog(10.d0)*dsin(theta_c)+dcos(theta_c)
            a1=a1*dexp(-1.d0*slope*theta_c*dlog(10.d0))
            a2=slope*dlog(10.d0)*dsin(l)+dcos(l)
```

```
                a2=a2*dexp(-1.d0*slope*l*dlog(10.d0))
                a1=(a1-a2)*dexp(cons*dlog(10.d0))/(slope*dlog(10.d0))**2.d0
                a1=norm*(a1+10.d0*(1.d0-dcos(theta_c)))
                if (dabs(a1-a).le.0.00000001d0) goto 15
                if (a1.ge.a) then
                        l2=l
                else
                        l1=l
                endif
                goto 10
15              theta1 = l
        endif
66      revent(13) = theta1

c7      now find phi of reaction
        phi1 = 2.d0 * pi * uniran(iseed)

c8      convert theta1 to lab coordinates
        w_2 = m_beam**2.d0 + m_tar**2.d0 + 2.d0*m_tar*e_beam1
        if (reaction.eq.0)then
c       first the transfer reaction
         q = (w_2 - m_frag1**2.d0 - m_prod**2.d0)**2.d0
         q = (q - 4.d0 * m_prod**2.d0 * m_frag1**2.d0) / (4.d0*w_2)
        elseif (reaction.eq.1) then
c       now the fragmentation (basically v_frag = v_beam)
         v_beam = (m_tar * p_beam1)**2.d0 / w_2
         v_beam = dsqrt(v_beam / (v_beam + m_beam**2.d0))
         q = (m_frag1 * v_beam)**2.d0 / (1.d0 - v_beam**2.d0)
        endif

        if(q.lt.0.d0) then
          ievent(2) = 2
          goto 9999
        endif

        e_frag = dsqrt( q + m_frag1**2.d0 )
        v_frag = dsqrt(q) / e_frag

        revent(14) = v_frag

        gamma = (m_tar + e_beam1)/dsqrt(w_2)
        beta = p_beam1/(m_tar + e_beam1)

        theta2 = gamma*(v_frag*dcos(theta1)+beta)
        theta2 = daftan(v_frag*dsin(theta1),theta2)

        v_frag1 = v_frag**2.d0 + beta**2.d0 + 2.d0*v_frag*beta*dcos(theta1)
        v_frag1 = dsqrt(v_frag1 - (v_frag*beta*dsin(theta1))**2.d0)
        v_frag = v_frag1 / (1.d0 + v_frag * beta * dcos(theta1))
        phi2 = phi1

        revent(15) = v_frag
        revent(16) = theta2
```

```
c8.5    now the fragment is in the beam frame, so do a rotation to take
c       it into the lab frame.
        vfragx = v_frag * dsin(theta2) * dcos(phi2)
        vfragy = v_frag * dsin(theta2) * dsin(phi2)
        vfragz = v_frag * dcos(theta2)
        temp_r = vfragx * dcos(th_emit) * dcos(phi_emit)
        temp_r = temp_r - vfragy * dsin(phi_emit)
        temp_r = temp_r + vfragz * dsin(th_emit) * dcos(phi_emit)
        vfrag_x = temp_r

        temp_r = vfragx * dcos(th_emit) * dsin(phi_emit)
        temp_r = temp_r + vfragy * dcos(phi_emit)
        temp_r = temp_r + vfragz * dsin(th_emit) * dsin(phi_emit)
        vfrag_y = temp_r

        temp_r = vfragx * dsin(th_emit)
        temp_r = vfragz * dcos(th_emit) - temp_r
        vfrag_z = temp_r
        v_frag = dsqrt(vfrag_x**2.d0 + vfrag_y**2.d0 + vfrag_z**2.d0)
        theta2 = dacos(vfrag_z / v_frag)

        phi2 = daftan(vfrag_y,vfrag_x)

        revent(17) = v_frag
        revent(18) = theta2

c       now everything for the fragment is in lab coordinates, so now
c       we can do the decay of the fragment.

c9      first in CoM
        theta_p1 = dacos(2.d0*uniran(iseed) - 1.0d0)
        if (singles.eq.1) theta_p1 = sing2
        phi_p = 2.d0*pi * uniran(iseed)

        revent(20) = theta_p1

        theta_d1 = pi - theta_p1
        phi_d = pi + phi_p
        if (phi_d.gt.2.d0*pi) phi_d = phi_d - 2.d0 * pi

        revent(22) = theta_d1

        p_2 = (m_frag1**2.d0 - m_prot**2.d0 - m_dau**2.d0)**2.d0
        p_2 = (p_2 - 4.d0*(m_prot**2.d0)*(m_dau**2.d0))/(4.d0*m_frag1**2.d0)
        e_p = dsqrt(p_2 + m_prot**2.d0)
        e_d = dsqrt(p_2 + m_dau**2.d0)
        v_p1 = dsqrt(p_2) / e_p
        v_d1 = dsqrt(p_2) / e_d

        revent(19) = v_p1
        revent(21) = v_d1

c       now go to lab frame
```

```
c10     first transform to the fragments lab coordinates
        gamma = 1.d0 / dsqrt(1.d0 - v_frag**2.d0)
        theta_p=gamma*(v_p1*dcos(theta_p1)+v_frag)
        theta_p = daftan(v_p1*dsin(theta_p1),theta_p)
        theta_d=gamma*(v_d1*dcos(theta_d1)+v_frag)
        theta_d = daftan(v_d1*dsin(theta_d1),theta_d)
        v_p = v_p1**2.d0 + v_frag**2.d0 + 2.d0*v_p1*v_frag*dcos(theta_p1)
        v_p = dsqrt(v_p - (v_p1*v_frag*dsin(theta_p1))**2.d0)
        v_p = v_p / (1.d0 + v_p1*v_frag*dcos(theta_p1))
        v_d = v_d1**2.d0 + v_frag**2.d0 + 2.d0*v_d1*v_frag*dcos(theta_d1)
        v_d = dsqrt(v_d - (v_d1*v_frag*dsin(theta_d1))**2.d0)
        v_d = v_d / (1.d0 + v_d1*v_frag*dcos(theta_d1))

c11     now convert v_p and v_d to their x,y,z coords. using theta and phi
        vp_x1 = v_p * dsin(theta_p) * dcos(phi_p)
        vp_y1 = v_p * dsin(theta_p) * dsin(phi_p)
        vp_z1 = v_p * dcos(theta_p)
        vd_x1 = v_d * dsin(theta_d) * dcos(phi_d)
        vd_y1 = v_d * dsin(theta_d) * dsin(phi_d)
        vd_z1 = v_d * dcos(theta_d)

c12     now apply the rotation
        vp_x = vp_x1 * dcos(theta2) * dcos(phi2) - vp_y1 * dsin(phi2)
        vp_x = vp_x + vp_z1 * dsin(theta2) * dcos(phi2)
        vp_y = vp_x1 * dcos(theta2) * dsin(phi2) + vp_y1 * dcos(phi2)
        vp_y = vp_y + vp_z1 * dsin(theta2) * dsin(phi2)
        vp_z = vp_z1 * dcos(theta2) - vp_x1 * dsin(theta2)
        vd_x = vd_x1 * dcos(theta2) * dcos(phi2) - vd_y1 * dsin(phi2)
        vd_x = vd_x + vd_z1 * dsin(theta2) * dcos(phi2)
        vd_y = vd_x1 * dcos(theta2) * dsin(phi2) + vd_y1 * dcos(phi2)
        vd_y = vd_y + vd_z1 * dsin(theta2) * dsin(phi2)
        vd_z = vd_z1 * dcos(theta2) - vd_x1 * dsin(theta2)

c13     now convert back to v,theta,phi
        v_p = dsqrt(vp_x**2.d0 + vp_y**2.d0 + vp_z**2.d0)
        theta_p = daftan(dsqrt(vp_x**2.d0 + vp_y**2.d0),vp_z)
        if (vp_x.eq.0.d0) then
                phi_p = pi / 2.d0
                goto 78
        endif
        phi_p = daftan(vp_y,vp_x)
78      v_d = dsqrt(vd_x**2.d0 + vd_y**2.d0 + vd_z**2.d0)

        theta_d = daftan(dsqrt(vd_x**2.d0 + vd_y**2.d0),vd_z)
        if (vd_x.eq.0.d0) then
                phi_d = pi / 2.d0
                goto 79
        endif
        phi_d = daftan(vd_y,vd_x)

c
c HERE I WILL INSERT A PART WHERE WE CAN PUT IN INTENSITY [Win92] CALCULATED
c PARAMETERS FOR THE FRAGMENT
c
```

```
c       THETA_P = .298 * GASDEV(ISEED,1)
c       THETA_D = .065 * GASDEV(ISEED,1)
c
c       V_P = 254.7 * .3 * GASDEV(ISEED,1) + 254.7
c       V_P = V_P / DSQRT(M_PROT**2. + V_P**2.)
c
c       V_D = 3002.2 * .02 * GASDEV(ISEED,1) + 3002.2
c       V_D = V_D / DSQRT(M_DAU**2. + V_D**2.)

C  END OF INTENSITY INPUT


79      revent(23) = v_p
        revent(24) = theta_p
        revent(25) = v_d
        revent(26) = theta_d

c14     Need to find the energy loss for both of these particles so that I
c       can get them out of the target.  So find their KINETIC ENERGIES first.
        gamma_p = 1.d0 / dsqrt(1.d0 - v_p**2.d0)
        ke_p = (gamma_p - 1.d0) * m_prot
        gamma_d = 1.d0 / dsqrt(1.d0 - v_d**2.d0)
        ke_d = (gamma_d - 1.d0) * m_dau

        loss_p = (tar_thick - z1_beam) / dcos(theta_p) * p_eloss
        loss_d = (tar_thick - z1_beam) / dcos(theta_d) * d_eloss
        if (eloss_mode.eq.1) then
         if (ke_d.lt.demin .or. ke_d.gt.demax) itemp6=itemp6+1
         if (ke_p.lt.plimit(1) .or. ke_p.gt.plimit(4)) itemp7=itemp7+1
         loss_p = (1 - z1_beam/tar_thick) * mgcmsq
         loss_p = loss_p / dcos(theta_p)
         loss_d = loss_p / dcos(theta_d)
         rtemp(7) = ke_d**2.d0*deloss(2) + ke_d*deloss(1) + deloss(0)
         rtemp(7) = ke_d**3.d0*deloss(3) + rtemp(7)
         loss_d = rtemp(7) * loss_d
         if (ke_p.lt.plimit(2)) j = 1
         if (ke_p.ge.plimit(2) .and. ke_p.lt.plimit(3)) j = 2
         if (ke_p.ge.plimit(3)) j = 3
         rtemp(7) = ke_p**3.d0*peloss(j,3) + ke_p**2.d0*peloss(j,2)
         rtemp(7) = rtemp(7) + ke_p*peloss(j,1) + peloss(j,0)
         loss_p = rtemp(7) * loss_p
        endif

        ke_p = ke_p - loss_p
        ke_d = ke_d - loss_d

        revent(27) = loss_p
        revent(28) = loss_d

        if (ke_p.le.0.d0) then
                ievent(2)=3
                goto 9999
        endif
```

```
      if (ke_d.le.0.d0) then
            ievent(2)=4
            goto 9999
      endif

c14.5 fold in the energy resolution for the proton and daughter
      ep_res = res_p * ke_p / 100.d0
      ed_res = res_d * ke_d / 100.d0
      e_p_res = ke_p + ( ep_res * gasdev(iseed,1))
      e_d_res = ke_d + ( ed_res * gasdev(iseed,1))

      revent(29) = e_p_res
      revent(30) = e_d_res

c15   now find the x and y of the proton and daughter on the detectors.
      temp_r = (detz_p * 1000.d0 - z1_beam) / vp_z
      x_p = vp_x * temp_r + x1_beam
      y_p = vp_y * temp_r + y1_beam
      temp_r = (detz_d * 1000.d0 - z1_beam) / vd_z
      x_d = vd_x * temp_r + x1_beam
      y_d = vd_y * temp_r + y1_beam

      revent(31) = x_p
      revent(32) = y_p
      revent(33) = x_d
      revent(34) = y_d

c15.5 Now call the subroutines containing the proton and daughter
c     detector configurations.
c     first the detector array for the daughter nuclei

c     the "infinite" grid
c     call daughter1
c     if (flag.eq.1) then
c           ievent(2)=5
c           goto 9999
c     endif

c     the fragment telescope for 11n experiment
      call daughter3
      if (flag.eq.1) then
            ievent(2)=5
            goto 9999
      endif

cafsh some energy cuts to match experimental cuts for 13O decay
c     if (ke_d.ge.442.d0) then
c       if (x_d.ge.0 .and. y_d.ge.0) then
c           ievent(2)=5
c           goto 9999
c       endif
c     endif
c     if (ke_d.ge.445.d0) then
c       if (x_d.gt.0 .and. y_d.lt.0) then
```

```
c                 ievent(2)=5
c                 goto 9999
c           endif
c         endif
c         if (ke_d.ge.447.d0) then
c           if (x_d.lt.0 .and. y_d.lt.0) then
c                 ievent(2)=5
c                 goto 9999
c           endif
c         endif

c Now enforce the fragment energy lower limit
          if (ke_d.le.3.6d2) then
                ievent(2)=5
                goto 9999
          endif

c         Now let's do the protons
c         now the detector array for the protons
c         first the "infinite" grid
c         call proton1
c         if (flag.eq.1) then
c               ievent(2)=6
c               goto 9999
c         endif

c         now the Maryland Forward Array
          grid_p = pi
          call proton2
          if (flag.eq.1) then
                ievent(2)=6
                goto 9999
          endif

          revent(35) = x_p_res
          revent(36) = y_p_res
          revent(37) = x_d_res
          revent(38) = y_d_res

c         now let's analyze the results we have gotten to reconstruct
c         the mass of the fragment
c16       first the exact solution.

c         calculating the distance travelled by proton
          temp1 = detz_p * 1000.d0 - revent(11)
          temp2 = revent(32) - revent(5)
          temp3 = revent(31) - revent(4)
          a = temp1**2.d0 + temp2**2.d0 + temp3**2.d0

c         now the distance travelled by the daughter
          temp1 = detz_d * 1000.d0 - revent(11)
          temp2 = revent(34) - revent(5)
          temp3 = revent(33) - revent(4)
          b = temp1**2.d0 + temp2**2.d0 + temp3**2.d0
```

```
c       distance between where the proton and the daughter hit on
c       the detectors
        temp1 = (detz_p - detz_d) * 1000.d0
        temp2 = revent(32) - revent(34)
        temp3 = revent(31) - revent(33)
        c = temp1**2.d0 + temp2**2.d0 + temp3**2.d0

c       now calculate the cosine of the angle between the path of
c       the proton and that of the daughter
        cos_exact = (a + b - c)/(2.d0 * dsqrt(a*b))

c       now use the above information to get the mass of the fragment
        ep_exact = ke_p + m_prot + revent(27)
        ed_exact = ke_d + m_dau + revent(28)
        mf_exact = ep_exact**2.d0 - m_prot**2.d0
        mf_exact = mf_exact * (ed_exact**2.d0 - m_dau**2.d0)
        mf_exact = 2.d0 * cos_exact * dsqrt(mf_exact)
        mf_exact = 2.d0 * ep_exact * ed_exact - mf_exact
        mf_exact = dsqrt(mf_exact + m_prot**2.d0 + m_dau**2.d0)

c16.5   now the experimental solution (with resolutions folded in).
        if (v2p(3).eq.0.d0) v2p(3) = detz_p*1.d2
        temp1 = v2p(3) * 1.d1
        temp2 = revent(36) - revent(5)
        temp3 = revent(35) - revent(4)
        a = temp1**2.d0 + temp2**2.d0 + temp3**2.d0

        temp1 = detz_d * 1000.d0
        temp2 = revent(38) - revent(5)
        temp3 = revent(37) - revent(4)
        b = temp1**2.d0 + temp2**2.d0 + temp3**2.d0

        temp1 = (v2p(3)/1.d2 - detz_d) * 1000.d0
        temp2 = revent(38) - revent(36)
        temp3 = revent(37) - revent(35)
        c = temp1**2.d0 + temp2**2.d0 + temp3**2.d0

        cos_exp = (a + b - c)/(2.d0 * dsqrt(a*b))

        revent(39) = dacos(cos_exp)

        ep_exp = revent(29) + m_prot
        ed_exp = revent(30) + m_dau
        mf_exp = ep_exp**2.d0 - m_prot**2.d0
        mf_exp = mf_exp * (ed_exp**2.d0 - m_dau**2.d0)
        mf_exp = 2.d0 * cos_exp * dsqrt(mf_exp)
        mf_exp = 2.d0 * ep_exp * ed_exp - mf_exp
        mf_exp = dsqrt(mf_exp + m_prot**2.d0 + m_dau**2.d0)

        revent(40) = (mf_exp - m_prot - m_dau) * 1.d3

cafsh   now put decay energy cut
c       if (revent(40).gt.2.4d3) goto 9999
```

```
c17     now write out the good information.
        j = nint(revent(40)*1.d-3/fac)
        if (j.gt.1000) goto 9999
        hexp(j) = hexp(j) + 1

        if (out.eq.1) write(62) (event(j),j=1,44)

        if (ievent(2).eq.0) iaf(7)=iaf(7)+1
9999    if (ievent(2).eq.1) iaf(1)=iaf(1)+1
        if (ievent(2).eq.2) iaf(2)=iaf(2)+1
        if (ievent(2).eq.3) iaf(3)=iaf(3)+1
        if (ievent(2).eq.4) iaf(4)=iaf(4)+1
        if (ievent(2).eq.5) iaf(5)=iaf(5)+1
        if (ievent(2).eq.6) iaf(6)=iaf(6)+1

10000   continue

        write(*,*) 'Bad Decays              = ',iaf(1)
        write(*,*) 'Bad Transfers           = ',iaf(2)
        write(*,*) 'Proton Stopped in Target  = ',iaf(3)
        write(*,*) 'Daughter Stopped in Target = ',iaf(4)
        write(*,*) 'Proton Missed Detector    = ',iaf(5)
        write(*,*) 'Daughter Missed Detector  = ',iaf(6)
        write(*,*) ' '
        write(*,*) 'Good Events             = ',iaf(7)
        write(*,*) '----------------------------------------'
        iaf(1)=iaf(1)+iaf(2)+iaf(3)+iaf(4)+iaf(5)+iaf(6)+iaf(7)
        write(*,*) 'Unaccounted             = ',eventn-iaf(1)
        if (eloss_mode.eq.1) then
         write(*,*) ' '
         write(*,*) 'Energy Loss Results on Min. and Max. Limits:'
         write(*,*) 'Beam Out of Range        = ',itemp5
         write(*,*) 'Daughter Out of Range    = ',itemp6
         write(*,*) 'Protons Out of Range     = ',itemp7
        endif

        if (out.eq.1) goto 1034
        open (unit=71,file='masses.dat',status='new')
1033    do 1034 j=1,100
          write(71,*) real(j)*fac,hexp(j)
c         if (hexp(j).ne.0) write(71,*) real(j)*fac,hexp(j)
c         write(71,*) hexp(j)
1034    continue

        stop
        end
```

A.5 Subroutines

```
c       NOW THE SUBROUTINES AND FUNCTIONS USED IN PRO_DECAY

c       Function to generate random numbers according to desired distributions.
        function gasdev(iseed,dist)

c       The variable 'dist' determines the distribution:
c       1) Generates a gaussian of sigma=1 [Pre92]
c       2) Generates a Lorentzian of FWHM=1
c       3) Generates a flat dist. between -.5 and .5
      Real*8 Uniran,erand48,gasdev,daftan
      Integer*4 iseed(2),lseed(2)
      Integer*2 jseed(3),dist
      Equivalence (Lseed(1),jseed(1))
          DATA ISET/0/
          if (dist.eq.1) then
            IF (ISET.EQ.0) THEN
1                 V1=2.d0*uniran(iseed)-1.d0
                  V2=2.d0*uniran(iseed)-1.d0
                  R=V1**2+V2**2
                  IF (R.GE.1..OR.R.EQ.0.) GOTO 1
                  FAC=DSQRT(-2.d0*LOG(R)/R)
                  GSET=V1*FAC
                  GASDEV=V2*FAC
                  ISET=1
            ELSE
                  GASDEV=GSET
                  ISET=0
            ENDIF
          endif
          if (dist.eq.2) gasdev=dtan(dacos(-1.d0)*uniran(iseed))/2.d0
          if (dist.eq.3) gasdev=uniran(iseed)-0.5d0
          RETURN
          END

c-------------------------------------------------------

c       Random number generator (used with erand48.c)
      Function Uniran(iseed)
      Real*8 Uniran,erand48,gasdev,daftan
      Integer*4 iseed(2),lseed(2)
      Integer*2 jseed(3)
      Equivalence (Lseed(1),jseed(1))

C-UniX

      lseed(1) = iseed(1)
      lseed(2) = iseed(2)
      Uniran = Erand48(jSeeD)
      iseed(1) = lseed(1)
      iseed(2) = lseed(2)
```

```
      return
      end

c-------------------------------------------------------

c     Routine to create a thermal dist.
      subroutine thermal(temp,e_therm,jj,kk)

      real*8 temp,e_therm(jj:kk),f(5),pi,e,daftan
      integer *4 i,j,k,jj,kk
      pi = dacos(-1.d0)
      e_therm(0)=0.d0
      do 1000 i=jj,kk-1
            do 10 j=1,5
                  e=float(i) + float(j-1)*2.5d-1
                  f(j)=dsqrt(e/pi/temp)*2.d0/temp
                  f(j)=f(j)*dexp(-e/temp)
10          continue
            e_therm(i+1)=f(1)+4.d0*f(2)+2.d0*f(3)+4.d0*f(4)
            e_therm(i+1)=(e_therm(i+1)+f(5))*2.5d-1/3.d0
            e_therm(i+1)=e_therm(i+1) + e_therm(i)
1000  continue
      return
      end

c-------------------------------------------------------

c     simulates a grid detector for the fragments
      subroutine daughter1

      integer*4 ievent(4),itemp2,itemp4,flag
      real*8 revent(40),grid_d,x_d,y_d,x_d_res,y_d_res,daftan
      common /all/ ievent,flag
      common /daughter/ x_d,y_d,x_d_res,y_d_res,grid_d

      flag=0
      if (dabs(x_d).gt.1.d4.or.dabs(y_d).gt.1.d4) then
            ievent(2)=5
            flag=1
            goto 3023
      endif
      y_d_res=(float(int(y_d/grid_d))+float(int(y_d/dabs(y_d)))*5.d-1)*grid_d
      x_d_res=(float(int(x_d/grid_d))+float(int(x_d/dabs(x_d)))*5.d-1)*grid_d

3023  return
      end

c-------------------------------------------------------

c     The fragment telescope in 11N experiment
      subroutine daughter3

      integer*4 ievent(4),itemp2,itemp4,flag,iseed(2)
```

```
      real*8 revent(40),grid_d,x_d,y_d,x_d_res,y_d_res,daftan
      real*8 gasdev,r,t,pi
      common /all/ ievent,flag
      common /daughter/ x_d,y_d,x_d_res,y_d_res,grid_d,pi
      common /seeds/ iseed

      flag=0
      if (dabs(x_d).gt.2.d1.or.dabs(y_d).gt.2.d1) then
            ievent(2)=5
            flag=1
            goto 3023
      endif
      if (x_d.lt.0.d0 .and. y_d.gt.0.d0) then
            ievent(2)=5
            flag=1
            goto 3023
      endif

      r = grid_d * gasdev(iseed,1)
      t = 2.d0 * pi * (gasdev(iseed,3)+.5d0)

      x_d_res = x_d + r*dcos(t)
      y_d_res = y_d + r*dsin(t)

3023  return
      end

c-----------------------------------------------------------------------

      subroutine proton1

      integer*4 ievent(4),itemp1,itemp3,flag
      real*8 x_p,y_p,x_p_res,y_p_res,grid_p,daftan,rtemp
      common /proton/ x_p,y_p,x_p_res,y_p_res,grid_p
      common /all/ ievent,flag

c     now fold in the position resolution assuming a square detector grid
c     with square elements.  If the particle hits right in between two
c     elements, then it will be "ignored".

      rtemp = dsqrt(x_p**2.d0 + y_p**2.d0)

      flag = 0
      if (rtemp.lt.2.4d1 .or. rtemp.gt.1.d2) then
            ievent(2)=6
            flag=1
            goto 3024
      endif
      x_p_res = float(idint(x_p/grid_p))
      x_p_res = (x_p_res+float(idint(x_p/dabs(x_p)))*5.d-1)*grid_p
      y_p_res = float(idint(y_p/grid_p))
      y_p_res = (y_p_res+float(idint(y_p/dabs(y_p)))*5.d-1)*grid_p

3024  return
```

```
      end

c-----------------------------------------------------------------------
c     The MFA

      subroutine proton2

      integer*4 ievent(4),flag,ir,ith,icheck
      real*8 x_p,y_p,x_p_res,y_p_res,mar_rp,pi,daftan
      real*8 mar_thp,mar_thp1
      common /proton/ x_p,y_p,x_p_res,y_p_res,pi
      common /all/ ievent,flag

      icheck = 0

c     Let's put in the Maryland Forward Array.
c     first change the x,y into r,theta

      mar_rp = dsqrt(x_p**2.d0 + y_p**2.d0)
      flag = 0
      if (mar_rp.lt.2.4d1 .or. mar_rp.gt.4.35d1) then
            ievent(2)=6
            flag = 1
            goto 20
      endif

c     mar_thp is the theta according to detector 2's left side and
c     follow the numbering scheme (2,3,4,...,15,16,1)

      mar_thp = daftan(x_p,y_p)*1.8d2/pi - 1.4d1
      if (mar_thp.lt.0.d0) mar_thp=mar_thp+3.6d2

c     now check to see where on the detector the hit is (resolution)

      mar_thp = float(int(mar_thp / 2.25d1))
      ith = int(mar_thp / 4.)
      mar_thp = (mar_thp * 2.25d1 + 1.125d1+1.4d1) * pi/1.8d2

      mar_rp = float(int(mar_rp / 1.5d0)) * 1.5d0 + .75d0
      ir = 16 - nint((mar_rp - 24.75) / 1.5) + ith*100

      if (ir.eq.114 .or. ir.eq.206 .or. ir.eq.207) icheck=1
      if (ir.eq.213 .or. ir.eq.216 .or. ir.eq.309) icheck=1
      if (ir.eq.310 .or. ir.eq.311) icheck=1
    if (ir.eq.215.and.mar_thp.gt.4.3.and.mar_thp.lt.4.4) icheck=1

      if (icheck.eq.1) then
            ievent(2)=6
            flag = 1
            goto 20
      endif

c     now convert back to x,y
      x_p_res = mar_rp * dsin(mar_thp)
```

```
        y_p_res = mar_rp * dcos(mar_thp)

20      return
        end


c-------------------------------------------------------

c       A function to do arctan without the usual error problems
        function daftan(y,x)

        real*8 a,b,c,x,y,daftan,pi

        pi = dacos(-1.d0)
        a = dabs(y/x)
        daftan = datan(a)
        if (x.lt.0.d0.and.y.ge.0.d0) daftan=pi-datan(a)
        if (x.ge.0.d0.and.y.lt.0.d0) daftan=2.d0*pi-datan(a)
        if (x.lt.0.d0.and.y.lt.0.d0) daftan=pi+datan(a)

        return
        end

c-------------------------------------------------------

c       Routine to do a binary search within an array
        subroutine binsearch (a,j,k,b,i,r)

        real*8 a(j:k),b,r
        integer*4 i,max,min

        if (a(k).le.a(j)) write(*,*) 'There is an error in Binsearch'
        r = 0.d0
        i = int((j+k) / 2)
        if (a(k).le.b) then
                i = k
                goto 50
        elseif (a(j).eq.b) then
                i = j
                goto 50
        endif

        max=k
        min=j

10      i = int((max+min) / 2)
          if (a(i).gt.b) then
                max = i
          else
                min = i
          endif
          if (max-min.le.1) goto 20
        goto 10
```

```
20      if (dabs(a(max)-b).lt.dabs(a(min)-b)) then
          i = max
        else
          i = min
        endif

        if (max.eq.min) then
          r = 0
        else
          i = min
          r = (b-a(min)) / (a(max)-a(min))
        endif

50      return
        end

c-------------------------------------------------------

        subroutine lineshape(icount)
c  this routine will calculate the line-shape due to the width of a state including Coul. and Centrifugal
c  barriers.

C*****************************************************************C
C       THIS IS FOR A STATE WITH ONE DECAY BRANCH ONLY  C
C*****************************************************************C

        integer*4 ievent(4),flag,iseed(2),l_mom,a_dau,z_dau
        integer*4 a1,z1,icount
        real*8 m_frag,m_dau,m_prot,w_decay,pen,estep
        real*8 r,k,rk,rwidth,eres,m_mu,emin,emax
        real*8 prob(0:1001),energy(0:1001),e_e,gamma
        real*8 sigma

        common /all/ ievent,flag
        common /seeds/ iseed
        common /penetr1/ m_frag,a_dau,z_dau,m_dau,m_prot,l_mom
        common /penetr2/ w_decay,prob,energy

c  first let's setup for the penetrability calculation by calculating
c  the reduced width

        a1 = a_dau
        z1 = z_dau

        eres = m_frag - m_dau - m_prot

        m_mu = (m_dau*m_prot) / (m_dau+m_prot)
        r = 1.4 * (a1**(1.d0/3.d0) + 1.d0)

        k = dsqrt(2.d0*m_mu*eres) / 1.97d2
        rk = r * k

        call penetrate(l_mom,k,rk,z1,1,m_mu,pen)
```

```
      rwidth = w_decay / (2.d0*rk*pen)

      emin = 0.d0
      emax = 1.d1
      estep = 1.d-2
      prob(0) = 0.d0
      energy(0) = 0.d0
      icount = 0

c  now loop over the decay energies

      do e_e = emin+estep,emax,estep
        icount = icount+1
        k = dsqrt(2.d0*m_mu*e_e) / 1.97d2
        rk = k * r

        call penetrate(l_mom,k,rk,z1,1,m_mu,pen)

        gamma = 2.d0 * rk * rwidth * pen
        sigma = gamma/((e_e-eres)**2.d0+(gamma/2.d0)**2.d0)

        prob(icount) = prob(icount-1) + sigma
        energy(icount) = e_e

      end do

      do i = 1,icount
        prob(i) = prob(i) / prob(icount)
      end do

      return
      end

C-------------------------------------------------

      subroutine lineshape(icount)
c  this routine will calculate the line-Shape for a state with two
c  proton decay branches.

C*****************************************************************C
C    THIS IS FOR A STATE WITH TWO DECAY BRANCHES ONLY    C
C*****************************************************************C

      integer*4 ievent(4),flag,iseed(2),l_mom,a_dau,z_dau
      integer*4 a1,z1,icount
      real*8 m_frag,m_dau,m_prot,w_decay,pen,estep
      real*8 r,k,rk,rwidth,eres,eres2,m_mu,emin,emax
      real*8 prob(0:1001),energy(0:1001),e_e,gamma
      real*8 sigma,m_mu2,k2,rk2,rwidth2,gamma2

      common /all/ ievent,flag
      common /seeds/ iseed
      common /penetr1/ m_frag,a_dau,z_dau,m_dau,m_prot,l_mom
      common /penetr2/ w_decay,prob,energy
```

```
c  first let's setup for the penetrability calculation by calculating
c  the reduced width
          a1 = a_dau
          z1 = z_dau
          r = 1.4 * (a1**(1.d0/3.d0) + 1.d0)

          eres = m_frag - m_dau - m_prot
          eres2=eres-3.354d0
caf       eres2=eres+3.354d0

          m_mu = (m_dau*m_prot) / (m_dau+m_prot)
          m_mu2= ((m_dau+3.354d0)*m_prot)/(m_dau+m_prot+3.354d0)
caf       m_mu2= ((m_dau-3.354d0)*m_prot)/(m_dau+m_prot-3.354d0)

          k = dsqrt(2.d0*m_mu*eres) / 1.97d2
          k2= dsqrt(2.d0*m_mu2*eres2) / 1.97d2
          rk = r * k
          rk2= r * k2

          call penetrate(l_mom,k,rk,z1,1,m_mu,pen)

          rwidth = w_decay / (2.d0*rk*pen)

          call penetrate(l_mom,k2,rk2,z1,1,m_mu2,pen)

c         total width is included next in the (# - w_decay)
caf       where # is the total width
          rwidth2 = (.5d0-w_decay) / (2.d0*rk2*pen)

          emin = 0.d0
          emax = 1.d1
          estep = 1.d-2
          prob(0) = 0.d0
          energy(0) = 0.d0
          icount = 0

c  now loop over the decay energies
          do e_e = emin+estep,emax,estep
            icount = icount+1
            k = dsqrt(2.d0*m_mu*e_e) / 1.97d2
            rk = k * r

            call penetrate(l_mom,k,rk,z1,1,m_mu,pen)

            gamma = 2.d0 * rk * rwidth * pen

           if (e_e.gt.3.354d0) then
            k2= dsqrt(2.d0*m_mu2*(e_e-3.354d0)) / 1.97d2
caf         k2= dsqrt(2.d0*m_mu2*(e_e+3.354d0)) / 1.97d2
            rk2= k2 * r

            call penetrate(l_mom,k2,rk2,z1,1,m_mu2,pen)
```

```
            gamma2= 2.d0 * rk2 * rwidth2 * pen
           else
            gamma2=0.d0
           endif

            gamma2= gamma2 + gamma
            sigma = gamma/((e_e-eres)**2.d0+(gamma2/2.d0)**2.d0)

            prob(icount) = prob(icount-1) + sigma
            energy(icount) = e_e

          end do

          do i = 1,icount
            prob(i) = prob(i) / prob(icount)
          end do

          return
          end

c-------------------------------------------------------

          Subroutine Penetrate(l,xk,rk,Z1,Z2,xmu,Pen)
c  Calculates the Coulomb + Centrifugal penetrability.

          integer*4 l,z1,z2
          real*8 xk,rk,xmu,pen
          real*8 xl,xeta,xrho,xxf,xxfp,xxg,xxgp

          if(xk.eq.0.d0) then
            Pen = 0.d0
            return
          end if

          xl  = float(l)
          xrho = rk
          xeta = float(z1*z2)*1.44d0*xmu/(1.97d2**2.d0 * xk)

          if(xeta.lt.5.d2) then

            Call Coull(xl,xeta,xrho,xxf,xxfp,xxg,xxgp)

            Pen  = 1.0d0/(xxf**2.d0 + xxg**2.d0)
          else
            Pen  = 0.d0
          end if

          return
          end

c-------------------------------------------------------

c  Random number generator written in C to be linked with the rest of the code
```

```
        double erand48_(xsubi)
        unsigned short xsubi[3];          /*Arrays passed by reference*/
{
        double r,erand48();

          r = erand48(xsubi);

        return(r);
}
```

A.6 Sample Input File

```
!
!        INPUT FILE FOR PRO_DECAY
!
3685367,4364983                 ! seeds
100000                          ! number of events
0,1.e-1                         ! output mode (1 eventfile, 0 masses), expansion factor
0                               ! 0=Transfer, 1=Fragmentation
1,1,10.d0                       ! 0=Lor/1=Pen/2=Therm/3=Flat, L (hbar), T (MeV)
1,1.7d1                 ! 1=100% Thermal Target Recoils, T (temperature MeV)
0,0.d0,1.483529864d0            ! 1=Singles,Scat. Theta, Decay Theta of P (rad)
12,7,1.1191693d4                ! A, Z, M of beam
4.077d1,3.d0                    ! E/A, and momentum width(%) of beam
2.8d0,4.8d0                     ! beam spot x-FWHM, y-FWHM on PPAC2(mm)
0.d0,0.d0                       ! beam x-offset, y-offset on PPAC2(mm)
2.d1,1.45d1                     ! beam spot x-radius, y-radius on PPAC1(mm)
-9.d0,1.4d1                     ! beam x-offset, y-offset on PPAC1(mm)
11,7,10270.459d0                ! A, Z, M of fragment
.2d0                            ! decay width (MeV)
10,6,9330.930d0                 ! A, Z, M of daughter 9327.576
9,4,8392.753d0                  ! A, Z, M of target
10,4,9325.506d0                 ! A, Z, M of product
0.2032d0,36.64                  ! target thickness(mm), and mg/cmsq
104.82d0                        ! energy loss of beam / mm (at beam energy)
77.260d0                        ! energy loss of daughter / mm (at beam energy)
2.14d0                          ! energy loss of protons / mm (at beam energy)
.199d0,.621d0                   ! proton, fragment detector distances from target (m)
5.d0,3.d0                       ! proton and fragment energy resolution (%)
1.d0,1.d0                       ! proton and fragment detector grid sizes (mm)
5.d-2,37.56d0                   ! theta critical and slope for scattering
1                               ! Actual E_loss equations on/off
4.2d2,5.4d2                     ! Beam : valid energy region
1.52776d0                       ! a0 for beam
-2.87639d-3                     ! a1 for beam
1.9453d-6                       ! a2 for beam
2.5d2,5.5d2                     ! Daughter: valid energy region
1.5147100d0                     ! a0 for daughter
-5.410140d-3                    ! a1 for daughter
9.0328270d-6                    ! a2 for daughter
-5.612011d-9                    ! a3 for daughter
1,10,30,100                     ! Protons : divided into three energy regions
2.30462d-1,-6.20771d-2          ! a0, a1 region 1
7.29768d-3,-3.01875d-4          ! a2, a3 region 1
7.96004d-2,-5.98858d-3          ! a0, a1 region 2
2.05111d-4,-2.56410d-6          ! a2, a3 region 2
3.08083d-2,-7.24017d-4          ! a0, a1 region 3
7.75216d-6,-3.00694d-8          ! a2, a3 region 3
3685367                         ! iseed1 for checking of input file
```

BIBLIOGRAPHY

Bibliography

[Ajz88] F. Ajzenberg-Selove, Nucl. Phys. **A490**, 142 (1988).

[Ajz90] F. Ajzenberg-Selove, Nucl. Phys. **A506**, 43 (1990).

[Ajz91] F. Ajzenberg-Selove, Nucl. Phys. **A523**, 38 (1991).

[Bar96] F. C. Barker, Phys. Rev. **C 53**, 1449 (1996).

[Ben74] W. Benenson , E. Kashy, D. H. Kong-A-Siou, A. Moalem, and H. Nann, Phys. Rev. **C 9**, 2130 (1974).

[Ben79] W. Benenson and E. Kashy, Rev. Mod. Phys. **51**, 527 (1979).

[Bie80] J. Biersack and L. Haggmark, Nucl. Instr. and Meth. **174**, 257 (1980).

[Bla91] J. M. Blatt and V. F. Weisskopf, *Theoretical Nuclear Physics*, Dover Publications Inc., New York (1991)

[Bro94] B. A. Brown, NSCL Report No. MSUCL-941, (1994).

[Bro96] B. A. Brown, private communications.

[Cur86] M. S. Curtin, L. H. Harwood, J. A. Nolen, B. Sherrill, Z. Q. Xie, and B. A. Brown, Phys. Rev. Lett. **56**, 34 (1986).

[For95] H. T. Fortune, D. Koltenuk, and C. K. Lau, Phys. Rev. **C** 51, 3023 (1995).

[Gol61] V. I. Goldanskii, JETP **39**, 497 (1960); Nucl. Phys. **19**, 482 (1960); **27**, 648 (1961).

[Har81] L. H. Harwood and J. A. Nolen, Nucl. Instr. and Meth. **186**, 435 (1981).

[Hof94] S. Hofman, GSI Report No. GSI-93-04, (1993); *Handbook of Nuclear Decay Modes*, CRC Press, Florida (1994).

[Jac75] J. D. Jackson, *Classical Electrodynamics*, John Wiley & Sons, New York (1975).

[Kry94] R. A. Kryger, private communications.

[Kry95] R. A. Kryger, A. Azhari, M. Hellström, J. H. Kelley, T. Kubo, R. Pfaff, E. Ramakrishnan, B. M. Sherrill, M. Thoennessen, and S. Yokoyama, Phys. Rev. Lett. **74**, 860 (1995).

[Kry96] R. A. Kryger, A. Azhari, J. Brown, J. Caggiano, M. Hellström, J. H. Kelley, B. M. Sherrill, M. Steiner, and M. Thoennessen, Phys. Rev. **C 53**, 1971 (1996).

[Llo92] W. J. Llope, R. Pedroni, R. Pak, G. D. Westfall, J. Wagner, A. Mignerey, D. Russ, J. Shea, H. Madani, R. A. Lacey, D. Craig, E. Gualtieri, S. Hannuschke, T. Li, J. Yee, and E. Norbeck, National Superconducting Cyclotron Laboratory Annual Report, 236 (1992).

[Mil88] W. T. Milner, Program STOPI, Oak Ridge (1988).

[Mil92] W. T. Milner, Program DAMM, Oak Ridge (1992).

[Mil96] D. J. Millener, private communications.

[Oer70] W. Von Oertzen, M. Liu, C. Caverzasio, J. C. Jacmart, F. Pougheon, M. Riou, J. C. Roynette, and C. Stephan, Nucl. Phys. **A143**, 34 (1970).

[Pag92] R. D. Page, P. J. Woods, R. A. Cunningham, T. Davison, N. J. Davis, S. Hofmann, A. N. James, K. Livingston, P. J. Sellin, and A. C. Shotter, Phys. Rev. Lett. **68**, 1287 (1992).

[Pag94] R. D. Page, P. J. Woods, R. A. Cunningham, T. Davison, N. J. Davis, A. N. James, K. Livingston, P. J. Sellin, and A. C. Shotter, Phys. Rev. Lett. **72**, 1798 (1994).

[Pre92] W. H. Press, S. A. Teukolsky, W. T. Vetterling, B. P. Flannery, *Numerical Recipes in Fortran The Art of Scientific Computing*, Press Syndicate of the University of Cambridge, Cambridge (1992).

[Rol88] C. E. Rolfs and W. S. Rodney, *Cauldrons in the Cosmos*, The University of Chicago Press, Chicago (1988).

[She92] B. M. Sherrill, D. J. Morrissey, J. A. Nolen, N. Orr, and J. A. Winger, Nucl. Instr. Meth. Phys. Res., Sect. **B 70**, 298 (1992).

[She94] B. M. Sherrill and J. Winfield, MSUCL report no. **449**, (1994)

[She95] R. Sherr, private communications.

[Tal60] I. Talmi and I. Unna, Phys. Rev. Lett. **4**, 469 (1960).

[Tig94] R. J. Tighe, D. M. Moltz, J. C. Batchelder, T. J. Ognibene, M. W. Rowe, and Joseph Cerny, Phys. Rev. **C 49**, R2871 (1994).

[Wig57] E. P. Wigner, Proceedings of the Robert A. Welch Conferences on Chemical Research **1**, 67 (1957).

[Win92] J. A. Winger, B. M. Sherrill, and D. J. Morrissey, Nucl. Instr. Meth. **B70**, 380 (1992).

[Wol88] H. Wollnik, Gios: A program for the design of General Ion Optical Systems, (1988).